ISBN 978-82-326-2594-9 (printed version)
ISBN 978-82-326-2595-6 (electronic version)
ISSN 1503-8181

Doctoral theses at NTNU, 2017:263

Thomas Hansen

Aerodynamic Optimisation of Airfoils and Winglets for Wind Turbine Application

Doctoral Thesis

Thomas Hansen

NTNU
Norwegian University of Science and Technology

Doctoral theses at NTNU, 2017:263

NTNU
Norwegian University of
Science and Technology
Faculty of Engineering
Department of Energy and Process Engineering

NTNU
Norwegian University of
Science and Technology

NTNU
Norwegian University of
Science and Technology

Thomas Hansen

Aerodynamic Optimisation of Airfoils and Winglets for Wind Turbine Application

Thesis for the degree of Philosophiae Doctor

Bergen, July 2017

Norwegian University of Science and Technology
Faculty of Engineering
Department of Energy and Process Engineering

NTNU
Norwegian University of
Science and Technology

NTNU
Norwegian University of Science and Technology

Thesis for the degree of Philosophiae Doctor

Faculty of Engineering
Department of Energy and Process Engineering

ISBN 978-82-326-2594-9 (printed version)
ISBN 978-82-326-2595-6 (electronic version)
ISSN 1503-8181

Doctoral theses at NTNU, 2017:263

Printed by Skipnes Kommunikasjon as

Preface

The work presented in this thesis is performed at the Department of Energy and Process Engineering (EPT) at the Norwegian University of Science and Technology (NTNU) in Trondheim, and at Christian Michelsen Research (CMR) Prototech in Bergen. The financial support provided by the Research Council of Norway and CMR Prototech is gratefully acknowledged.

I would like to thank my main supervisor Professor Per-Åge Krogstad for his guidance and support. The freedom Per-Åge has given me in order to both define and pursuit this PhD is most appreciated. Also, thanks to my co-supervisor Professor Lars Sætran for many interesting and educational discussions. A big thank you goes to Professor Anton Evgrafov from the Department of Mathematical Sciences at NTNU for his help with the exciting topic of optimisation.

The mentoring and guidance I have received from my co-supervisors Senior Engineer Øyvind Torvanger and PhD Sonia Faaland at CMR Prototech has been most valuable. Without their help and facilitation, this thesis would have been much harder to finalise. I have had much fun together with my colleagues at EPT and CMR Prototech, and I would like to thank you all for the necessary distractions.

I would also like to thank my family and friends for the encouragement and support. Especially my son Jesper has given me endless patience, and I promise you that I will make up for all the lost playtime. Finally, I would thank my girlfriend Gloria for her help and inspiration. Without your patience and love, this thesis would not exist. I hope you will continue to fly your glider next to mine for the rest of our lives.

Thomas Hansen

Bergen, July 2017

Abstract

The presented thesis summarises work on applying evolutionary optimisation algorithms for the design of airfoils and winglets for wind turbine application. This approach is more computationally expensive than using traditional design methods, i.e., gradient optimisation, but has the ability to find improved solutions in the multi-modal and rugged solution landscapes often encountered in aerodynamic design. Further, in this work the simulation tools are considered as black-boxes, where gradient information is difficult to obtain. In this scenario, evolutionary computation is a better approach since derivatives are not required.

The work is divided into three studies. First, the performance of the numerical tools is investigated by simulating a glider aircraft in steady level flight. The simulations are performed by solving the incompressible Reynolds-Averaged-Navier-Stokes (RANS) equations, and to predict the transitional boundary layer flow the correlation-based γ–Re_θ transition model is applied. Next, an airfoil optimisation method that reduces the loss in performance due to leading edge contamination on wind turbine blades is developed and tested. Here, the aerodynamic coefficients are computed using the panel code XFOIL, and to improve the accuracy, the code is adjusted for wind turbine airfoil flows. The airfoil shapes are optimised using the Covariance Matrix Adaptation Evolution Strategy algorithm, and in order to include constraints, an adaptive penalty function is created. Finally, a winglet optimisation method is developed and tested for a model-scale wind turbine. The turbine performance is simulated by solving the RANS equations and the best performing winglet is obtained by constructing a Kriging surrogate model. To refine the surrogate, an infill criterion based on expected improvement is maximised using a hybrid genetic-gradient optimisation algorithm. The simulated wind turbine performance, both with and without winglets, is validated by performing experiments in the NTNU wind tunnel.

In the first part of the work, it is found that the performance of the glider aircraft is strongly underpredicted when the transitional boundary layer flow is not included. This illustrates how important it is to simulate the flow physics correctly. When optimising airfoils and winglets for wind turbine application it is shown that global evolutionary algorithms produce comparable or improved solutions compared to current state of the art.

Dissertation

This thesis is based on a brief introduction to the area of research and the following appended papers:

Paper A

T. H. Hansen. Modeling the performance of the Standard Cirrus glider using Navier-Stokes CFD. *Technical Soaring*, Vol. 38, No. 1, 2014.

Paper B

T. H. Hansen. Airfoil Optimisation for Wind Turbine Application. Submitted to *Wind Energy*. Minor revision in progress.

Paper C

T. H. Hansen and F. Mühle. Winglet Optimisation for a Model-Scale Wind Turbine. Submitted to *Wind Energy*. Under review.

Contents

Introduction

Even if we are not aware of it, we are constantly optimising. When we drive to work, we choose the fastest lane or the most cost effective route, at work we hope to maximise the profit, and at home we try to minimise stress and expenses while maximising the quality of our lives. By constantly searching for the best solutions to problems, the human race has evolved to where we are today. However, our brain is not well equipped to solve complex, nonlinear systems with multiple input variables and constraints. To tackle such problems we need the help of computers. Recently, the progress in computational modelling has led to a revolution in our ability to solve complex problems. Today, numerical models both complement and replace theory and experiments, and it is no exaggeration to say that almost all research activities now involve a certain amount of modelling, computer simulations and optimisation [1].

In Figure 1, an antenna designed for NASA's Space Technology 5 (ST-5) mission is shown. This design is evolved using evolutionary computation, and as can be seen, the bizarre-looking antenna does not resemble anything a human would create. The ST-5 antenna is designed by the Evolvable

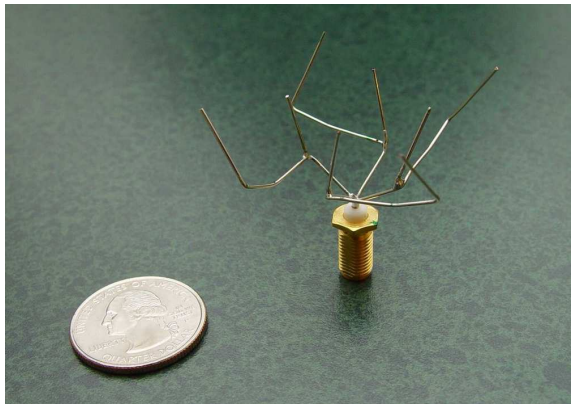

Figure 1: Optimised antenna for NASA's Space Technology 5 mission.

Systems Group at NASA Ames Research Center using a genetic optimisation algorithm [2]. This type of optimisation mimics Darwin's natural selection by only allowing the fittest members of a generation to produce offspring. By evolving the design over many generations using computers, the desired traits become more common, and in the end, the antenna best suited for the task is obtained.

The above case is an example of how evolutionary optimisation can discover improved solutions to complex problems. Even though a large amount of simulations is required to evolve the design, each simulation only takes a few seconds, and on a modern computer thousands of generations can be simulated in only one day.

In the wind industry, 25 years of evolution have resulted in the wind turbines in use today. Here, the designs with best performance have been obtained by parameter studies, optimisation and trial and error, and the long development time has resulted in wind turbines which are more reliable, more cost effective and more quiet [3]. However, compared to oil and gas, wind energy is still expensive and to ensure that this environmentally friendly energy source becomes more competitive, the cost, performance and reliability of wind turbines need to be improved further. This is especially true for offshore wind, which still is in its infancy. In the offshore environment there are tremendous opportunities, but also many new difficulties to overcome. In Figure 2, an example of modern offshore wind turbines is shown.

Figure 2: Modern offshore wind turbines.

In this thesis, numerical optimisation is used to design airfoils and winglets for wind turbine application, and the main research objective is to investigate if evolutionary computation techniques will improve current state of the art. Compared to traditional design methods, i.e. parameter studies and local gradient optimisation, evolutionary search engines have the ability to find the global best solution in a rugged and multi-modal design space. This is an important quality since most problems of aerodynamic interest are multi-modal and the computation of the mathematical model often introduces noise that makes the solution space rugged. Since it is important

to simulate the flow physics correctly in order to obtain solutions that will improve the performance not only on the computer, but also in the real world, the ability of the numerical analysis tools applied in this thesis are investigated in detail and results are validated to experimental data.

Numerical optimisation

Numerical optimisation is the science of finding the maximum or the minimum value of a mathematical function by applying search algorithms. In order to solve a problem using numerical optimisation, three components are required. First, the physical problem needs to be described using a mathematical model, then we need to be able to solve this model numerically, and finally we need to apply an optimisation algorithm that efficiently finds the optimal solution [1]. Unfortunately, no single optimisation algorithm is suited to solve all problems, and applying the correct type of algorithm is crucial in order to obtain the best solution. The choice of optimisation method depends both on the modality of the solution space, i.e. the level of nonlinearity in the mathematical model, the computational resources required to solve the numerics and whether gradient information is available. Optimisation algorithms can be classified in different ways, however, they generally fall into two categories, *local* and *global* optimisers.

Local gradient-based search methods are the most efficient when the solution space is smooth, unimodal and gradient information is available. These algorithms use the solution space slope-information to find the shortest path towards the (local) optimum in the nearest basin of attraction. The Newton method, the quasi-Newton method and the conjugate gradient method are well known examples of gradient-based algorithms [4]. While these solvers are very efficient as local search engines, they have the disadvantage of getting trapped on a local optimum if the problem is not convex. Once trapped, the search needs to be re-launched from a new (random) starting point and this operation often involves an inefficient exploration of unpromising regions in the design space. Another problem when using gradient-based search algorithms is numerical noise created either in the simulation of the mathematical model or in the calculation of the derivatives. When numerical noise is present the search landscape becomes rugged and gradient-based methods are no longer suited. In Figure 3, a smooth and a rugged multimodal solution space is illustrated in one-dimension.

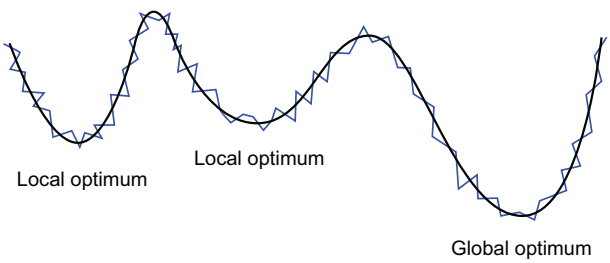

Figure 3: Smooth and rugged solution landscape.

When the solution space is smooth, unimodal and gradient information is not available, *local gradient-free* search methods are the most efficient. Examples of such algorithms, also known as direct search methods, are the simplex method, the complex method and pattern search [4]. These algorithms are often less efficient than gradient-based algorithms, but provide a more robust search since they do not as easily get stuck on a local minimum. By increasing the step-size, some of the gradient-free methods also have the ability to search a multi-modal landscape and they could even find the global optimum solution.

If the solution space is strongly multi-modal, *global* optimisation algorithms are the most efficient. A large number of different global algorithms exist, and the methods are classified according to if the search is deterministic, stochastic or heuristic. In the latter, we find the evolutionary algorithms which often mimic the natural evolution found in nature to search for the global best solution in a design space. Examples of well known evolutionary explorers are the genetic algorithm, particle swarm and the Covariance Matrix Adaptation Evolution Strategy (CMA-ES) [5, 6]. Compared to the local search engines, which rather quickly converge to the (local) optimum, the global algorithms often require a lengthy and expensive search.

The ability to optimise is linked to the computational resources required to solve the model numerically. For problems where the simulation time is very long, it might not be possible to solve the problem using a global optimisation algorithm directly. Then, surrogate models are the only viable approach. When applying a surrogate, the number of computational expensive simulations is reduced by creating an approximate model for the responses in the mathematical model. Depending on the problem, different surrogate models can be applied, such as polynomial response surface methods, neural network approximations and Gaussian process methods (Kriging) [7]. To initiate a surrogate model, a set of initial samples from the design space

is required. The location of these samples, known as a Design of Experiment (DoE) can be determined using a multitude of methods. Examples are Monte Carlo sampling, full factorial design and latin hypercube sampling [7]. Since the surrogate model is continuous and smooth it can be searched quickly using a global optimisation algorithm. However, the surrogate is only an approximation of the mathematical model and it therefore needs to be refined by performing more simulations. These new simulations are known as infill-points and to determine their best location, an infill-criterion is often maximised using an global optimisation algorithm [8].

Numerical simulations

Numerical simulations are only useful if they reproduce the physics of the problem accurately. In addition, if numerical simulations are to be used in a design process, they also need to be efficient. For aerodynamic applications such as aircraft wings and wind turbine rotor blades, the fluid is fully described by the Navier-Stokes equations. Unfortunately, for problems of aerodynamic interest, it is not possible to solve the Navier-Stokes equations directly since it requires computer power that is beyond the capabilities of any foreseeable system. It is therefore necessary to simplify the Navier-Stokes equations, and depending on the flow physics that we want to study this is performed in different ways. The first level of simplification is to apply a model for the smallest scales of the turbulent eddies. This reduces the solution of the full Navier-Stokes equations, known as a Direct Numerical Simulation, to a Large Eddy Simulation (LES). On the largest clusters of computers available today interesting aerodynamic problems can be solved using LES, however, the computational resources required are still huge and LES is seldom used for design purposes. The next level of simplification is the Reynolds-Averaged-Navier-Stoke (RANS) equations. Here, compressibility and viscosity are still present in the flow, while a turbulence model is used to estimate the fluctuating components. A large amount of different turbulence models have been developed over the years, ranging from simple eddy viscosity models to the computationally more expensive Reynolds Stress Models (RSM). While the eddy viscosity models approximate the turbulence as isotropic, RSM accounts for the anisotropy of turbulence and predicts the turbulent flow more realistic. Recently, transition models have been introduced to improve the flow predictions of eddy viscosity models. When using a transition model, the natural transitional flow phenomenon is accounted for, and the eddy viscosity models can be used to predict regions of laminar and turbulent flow more accurately.

If the fluid is considered inviscid, the Navier-Stokes equations simplify to the Euler equations. Compared to the RANS equations, the Euler equations are normally much simpler to solve, and this can lead to an order of magnitude saving in computational effort. If, in addition to viscosity also the rotation in the fluid is excluded, it is possible to model the flow using a potential method. In modern Computational Fluid Dynamics (CFD) codes, a grid discretisation of the fluid volume is required to solve the Full-Potential equations, the Euler equations, or the Navier-Stokes equations. This grid discretisation is called a mesh, and to obtain an accurate solution the mesh quality needs to match the flow problem. However, the number of cells in the mesh determines the computational resources required to solve the flow equations, and constructing a mesh using a low number of cells, which still has the correct quality can be very time consuming. A computationally less expensive approach is to use singularity methods. Here, only discretisation of the surface geometry is required and this both avoids the construction of the time consuming volume mesh and reduces the computational cost required to solve the flow equations. Singularity methods are used for Vortex Lattice and panel methods for potential flow where compressibility is excluded [9]. In Figure 4, an example of a surface and a volume mesh for a glider aircraft is shown. As can be seen, the volume mesh increases the number of cells compared to only generating a surface mesh.

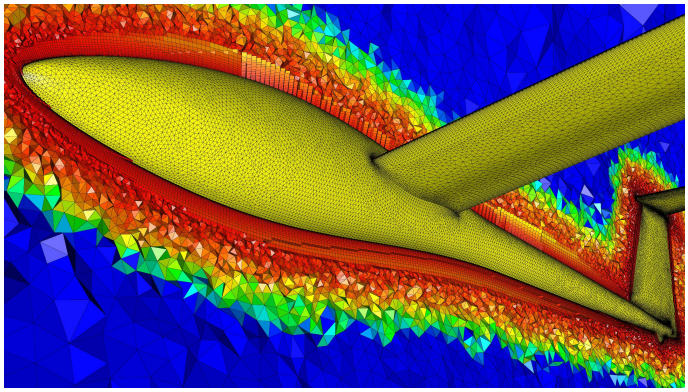

Figure 4: Surface and volume mesh. (Pointwise, Inc.)

For inviscid Euler and potential flow calculations, the effects of viscosity can be approximated using so-called viscous-coupled models. This is performed in the two-dimensional panel code XFOIL, which is the most common tool used to design and analyse airfoils in the aerospace and wind energy industry. These methods are very computational efficient, and even though

some aircraft now are being designed using RANS, most flying vehicles are developed either by solving the Euler equations or by using potential flow methods.

For the design of wind turbine rotor blades, Blade Element Momentum (BEM) methods are used. In BEM, momentum theory is coupled with the forces produced by the airfoils at different elements on the rotor blades in order to predict the power and thrust for a turbine design. To analyse wind turbines in more detail, however, RANS models are commonly applied [10]. In order to study wake effects, a method has recently been developed where LES is coupled with an actuator line model [11]. Here, the lift and drag for the rotor blades are calculated using a model outside of the flow domain, and included as body forces to the Navier-Stokes equations. This reduces the number of cells in the mesh and thereby decreases the computational effort required to solve the complex turbulent wake flows with LES.

Wind turbine airfoil design

The performance of lifting surfaces such as aircraft wings and wind turbine rotor blades depend on the cross sectional airfoil shapes. For airfoils, the aerodynamic properties are functions of the geometrical shape, angle of attack, α, Reynolds number, turbulence level and surface quality. The amount of different airfoils that can be generated is virtually unlimited, and the designer is faced with a difficult task when selecting or designing the shape best suited for the application. To a certain extent, airfoils can be characterised using a few design parameters. These are illustrated in Figure 5. Here, t is the maximum thickness, x_t is the location of the point of maximum thickness, f is the maximum camber, x_f is the location of maximum camber, r is the leading edge radius, te is the trailing-edge thickness

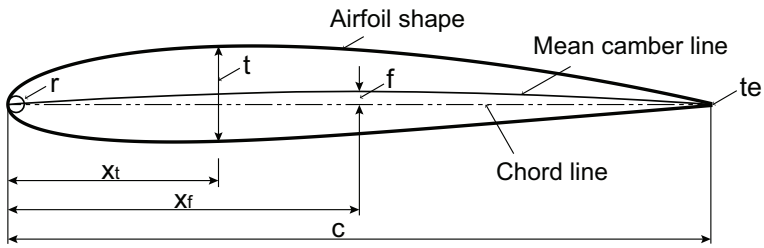

Figure 5: Airfoil geometric parameters, (NACA 2515).

and c is the chord. In order to classify airfoil shapes according to certain characteristics, different airfoil families have been developed over the years. Historically, the best known are the NACA 4- and 5-series developed by the National Advisory Committee for Aeronautics. These airfoils are described using a series of digits, and for the NACA 2515 airfoil depicted above, a maximum camber of 2% is located 50% from the leading edge, with a maximum airfoil thickness of 15% of the chord.

The total aerodynamic force on an airfoil may be decomposed into components perpendicular and parallel to the flow, in combination with a moment. In Figure 6, the aerodynamic lift, drag and pitching moment on an airfoil are shown.

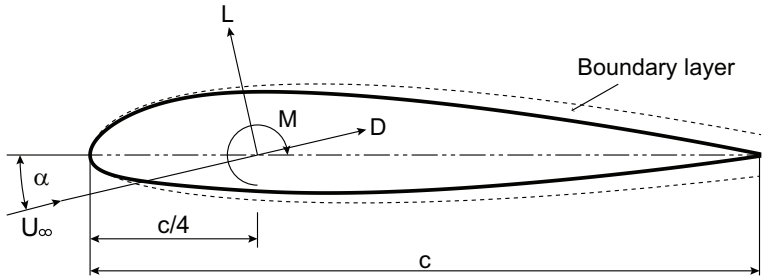

Figure 6: Aerodynamic forces and moments on an airfoil, (NACA 23015).

The lift and drag forces, and the moment are expressed as nondimensional coefficients according to

$$C_l = \frac{L}{q_\infty c}\,, \qquad C_d = \frac{D}{q_\infty c}, \qquad C_m = \frac{M}{q_\infty c^2}\,. \tag{1}$$

Here, q_∞ is the dynamic pressure given by $\frac{1}{2}\rho U_\infty^2$, where, ρ is the density of air and U_∞ is the velocity of the free-stream wind. The forces on an airfoil are characterised by the ratio of inertial to viscous forces in the flow. This relationship is nondimensionalised using the Reynolds number

$$Re = \frac{\rho U_\infty c}{\mu} \;=\; \frac{\text{Inertial forces}}{\text{Viscous forces}}\,, \tag{2}$$

where μ is the dynamic viscosity. The viscous forces are created in the boundary layer surrounding the airfoil, hence, the thickness of the boundary layer plays a crucial role in determining the aerodynamic properties of airfoils. The thickness depends on the Reynolds number, and for a Reynolds

number of about 1 million, the boundary layer is typically only a few millimeters thick at the leading edge and grows steadily to about a centimeter near the trailing edge [12].

In the early days of modern wind energy, NACA airfoils were frequently used on wind turbine rotor blades, even though these airfoils originally were developed for aircraft applications. The operational conditions for rotor blades are, however, different to aircraft wings, and it was soon realised that by applying aviation airfoils, the performance of wind turbines is limited. One main concern when using airfoils intended for aircraft on wind turbines is the high lift capability. While high lift is needed on an airplane at take-off and landing, it results in excessive power at high wind speeds on stall regulated wind turbines leading to burned-out generators [13]. Today, wind turbines have pitch control to better regulate the forces on the rotor blades, however, limiting the airfoil lift is still important in order to account for sudden shifts in wind speed due to atmospheric turbulence or from delay in the control system response [14]. In Figure 7, the lift and drag coefficients for the NACA 2515 airfoil are shown for angles of attack from -5° to 22°. The aerodynamic coefficients are calculated using the panel code XFOIL. As shown, a lower Reynolds number reduces the lift and increases the drag.

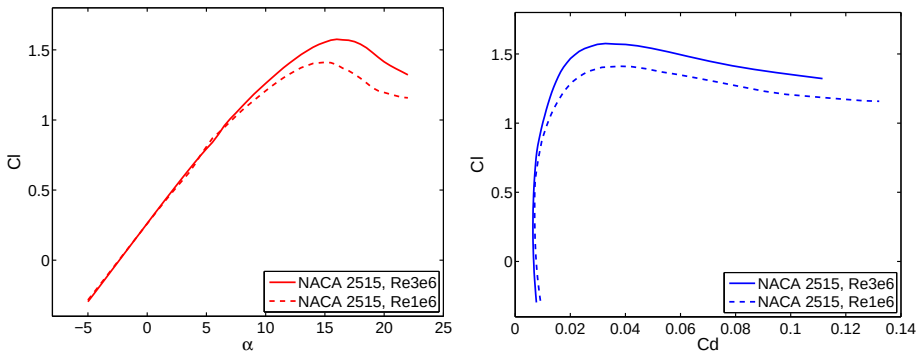

Figure 7: Predicted NACA airfoil lift and drag coefficient.

To maximise the power production on a wind turbine, the fundamental design criterion for the airfoils at the outer part of the rotor blade is to produce a high lift-to-drag ratio. In Figure 8, the effect of changing the airfoil shape and reducing the Reynolds number is shown. Here, the NACA 24015 airfoil shape outperforms the NACA 2515 since it produces higher lift-to-drag coefficients for a larger range in angles of attack. A wind turbine using the NACA 24015 will thus produce more power and make it easier

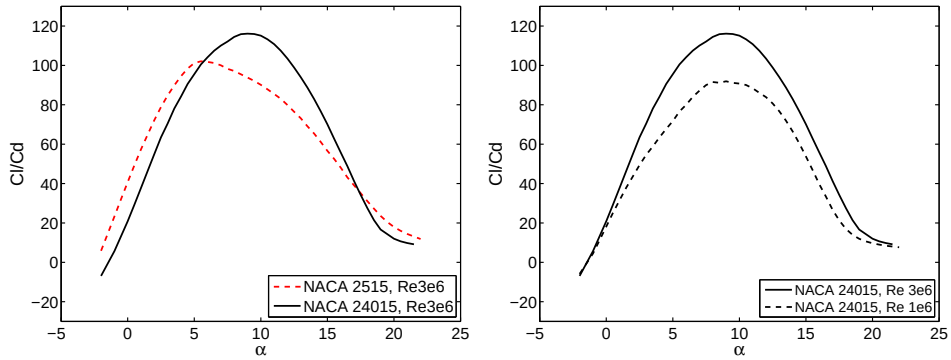

Figure 8: Airfoil performance, different shapes and Reynolds number.

for the control system to operate the rotor blades within the region of best performance. In the right figure, it can be seen that by reducing the Reynolds number on the NACA 24015 airfoil, the lift-to-drag ratios are reduced as well. Hence, when designing airfoils for wind turbine rotor blades the operational range in Reynolds numbers is an important design criterion.

Another main challenge for wind turbines is the loss in performance due to leading edge contamination caused by insects, sand, salt and hail. The contamination increases the surface roughness on the leading edge of the rotor blades, and thus turbulates the airflow on the airfoils resulting in reduced performance. Throughout the 20-year lifespan of a wind turbine, leading edge contamination might eventually also lead to rotor blade corrosion. An example of leading edge contamination caused by insects accumulating on a rotor blade is seen to the left in Figure 9. Here, the wind turbine has only been in operation for a few weeks. The wind turbine depicted to the right, on the other hand, has been in operation for a few years and needs repair.

Figure 9: Leading edge contamination.

The XFOIL predicted loss in performance due to turbulating the leading edge on the NACA 24015 airfoil is shown in Figure 10. Here, the calculations are performed at a Reynolds number of 3 million. As can be seen, the airfoil performance is reduced due to turbulating the leading edge, and the best lift-to-drag coefficient is reduced by about 43%. Insensitivity to roughness is known to be an important airfoil design criterion and specialised airfoils addressing this issue have been designed since the mid 1980's [13].

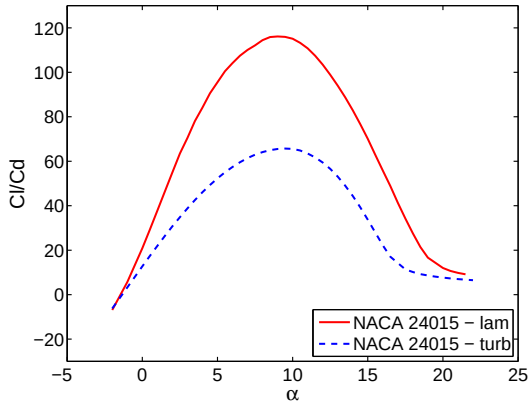

Figure 10: Airfoil performance, leading edge contamination.

Wind turbine winglet design

To improve the performance, most transport and glider aircraft are today designed with winglets. By applying winglets, the source of drag known as induced drag is reduced. When correctly designed, winglets create a flow-field that reduces the amount of span-wise flow in the tip region of the wing, and this increases the wing's efficiency without increasing the span [15]. In Figure 11, a modern winglet developed by Boeing for the B737 is shown. On this aircraft the winglet is reported to reduce the fuel consumption by 4-5% and also to moderate the noise levels at take-off [16]. On transport aircraft, span is regulated by the size of the airport gates. In the wind industry, however, span limitations have traditionally not been a concern, and among the main wind turbine manufacturers, only Enercon uses winglets on their designs. To allow better tower clearance, Enercon mounts their winglets towards the pressure side of the rotor blades. However, studies indicate that to get the best possible performance, the winglets should be mounted towards the suction side [17]. If future turbines are to be located in urban

Figure 11: Winglet on Boeing B737 MAX.

areas, or to reduce the size of floating structures, rotor span might become an important factor. Then, optimised winglets should be used to improve the performance of existing and new wind turbine rotor blades also by other manufacturers. In Figure 12 an Enercon turbine with winglets is shown.

Figure 12: Enercon-70 with winglets. (Photo by Tony Kanev)

Since the purpose of the winglet is to reduce the production of induced drag, it is important to understand the induced drag phenomenon. For a wing mounted between walls, like in a wind tunnel, induced drag does not exist. At this operational condition, the lift is created equally along the wing, and the forces can be considered as two-dimensional. In free flight, however, a wing or a rotor blade is not constricted by walls, and at this operational condition, the pressure difference due to the lift is equalised at the tips

where a vortex is created. Induced drag is thus a necessary consequence of producing lift on a finite-wing [12]. In Figure 13, the production of lift on the suction side of a wing in the wind tunnel is illustrated. Here, the lift is equally distributed along the wing, and no vortex is created.

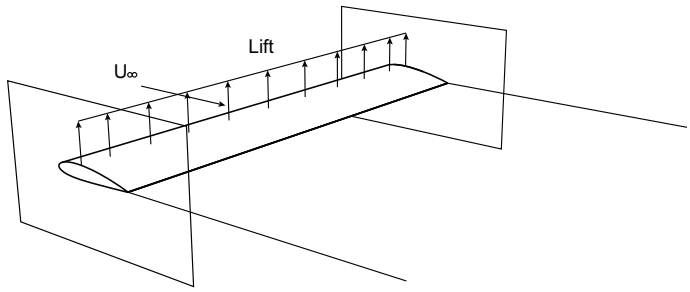

Figure 13: Lift distribution and wake on a wing with wall restriction.

In Figure 14, the lift and wake on a wing in free-flight condition is illustrated. As seen, the production of lift reduces towards the tips where a vortex is created.

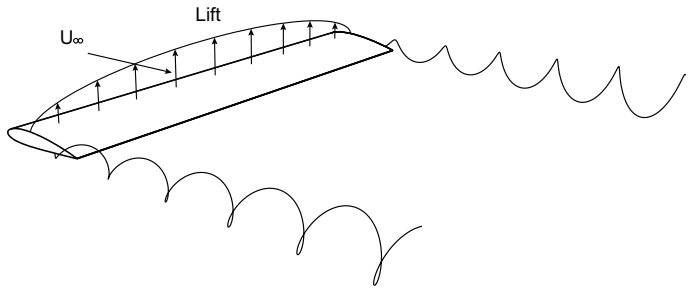

Figure 14: Lift distribution and wake on a wing in free-flight.

The local pressure difference at the tip of the wing influences the production of lift and drag, also further inboard, since the direction of the free-stream wind is reduced by the induced angle of attack, α_i. As illustrated in Figure 15, this results in the effective free-stream wind, $U_{(y)}$, and a reduced effective angle of attack, α_e. An effective (and reduced) local lift, F, is then generated perpendicular to this modified velocity vector. However, since the lift and drag are defined as forces perpendicular and parallel to the free-stream wind (the velocity far upstream), the induced drag, D_i, which is the parallel component of the effective lift, F, contributes to the total drag.

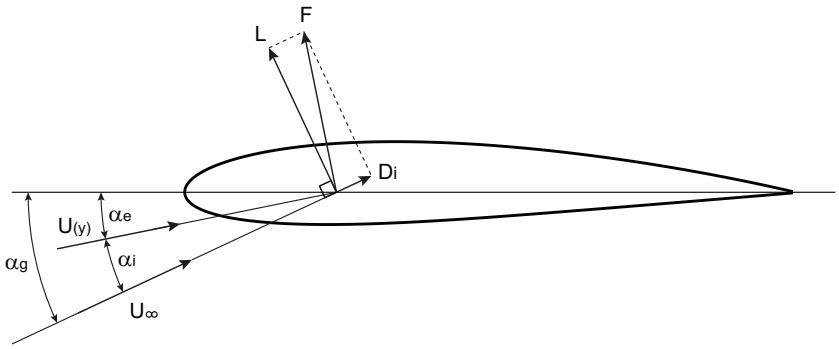

Figure 15: Production of induced drag along a wing. (Inspired by [12])

According to Prandtl's lifting line theory, induced drag is proportional to the square of the lift and inversely proportional to the aspect ratio [12]. This means that when the lift on a wing is increased, also the induced drag is increased. Further, if the aspect ratio of a wing is made larger, the induced drag is reduced. Designers of high performance glider aircraft have been leading the aerodynamic development of designing wings that minimize induced drag. Hence, modern high performance gliders have large span in combination with small chords to increase the aspect ratio. In addition, most competition gliders also use winglets to decrease the induced drag further. In Figure 16, a modern competition glider with winglets is shown. For gliders, winglets have been studied since the early 1980's, and first in recent years with higher demands on environmentally friendly transport, the commercial aviation industry has adopted the drag reducing technology. The

Figure 16: Ventus 3 glider with winglets. (Photo by Schempp-Hirth)

modern wind industry has also benefited strongly from the technology developed in aviation. In the years to come, wind energy has an important role in the fight against climate change and it is required that the wind industry leads the technology in their own direction to make wind energy more competitive. Then, the possible benefits from applying winglets on wind turbines should be investigated in more detail also by the wind industry.

Reflection on optimisation

Even tough evolutionary computation is able to find the global best solution, the optimisation algorithm only searches within the limits of a defined design space. Hence, if the size of the design space is increased a better solution might exist. However, when applying a larger number of degrees of freedom it quickly becomes much harder and more time consuming to find the best solution. In Figure 15, a wandering albatross shows off its skills and wings, which have been optimised by natural selection for 35 million years. In nature, few limitations exist for the possible design space, and as can be seen by looking at the wings of the albatross, we have a long way to go before we truly can claim to have optimised anything at all.

Figure 17: Wandering albatross. (Courtesy of Kimball Chen)

Summary of research results

The main part of the presented work concerns the application of evolutionary optimisation algorithms for the design of airfoils and winglets for wind turbine application. Additionally, the performance of the numerical tools used for the optimisation are investigated in detail and validated to experimental data.

The research objective for the papers is focused on the different components required to solve the design problem using numerical optimisation. In Paper A, the performance of the numerical tools is investigated in detail. In this first study, a glider aircraft is chosen for the validation to avoid the complex rotational flow that exists on wind turbines. The glider is simulated in three-dimensions by solving the incompressible Navier-Stokes equations. The turbulent flow is computed using the k–ω SST turbulence model and to calculate the transitional boundary layer flow, a correlation-based transition model is used. Also, the performance of the panel codes XFOIL and RFOIL are investigated by calculating the aerodynamic coefficients of the airfoil used at the outer part of the glider wing. The simulations are validated by comparing the results to experimental data, and it is shown that if the laminar flow is not included in the numerical model the performance of the glider is underpredicted both in two and three dimensions.

In Paper B, an airfoil optimisation method for wind turbine applications that controls the loss in performance due to leading edge contamination is developed and tested. In this work, the aerodynamic coefficients are computed using the panel code XFOIL, and to improve the accuracy, the code is first adjusted for wind turbine airfoil flows. The airfoil shape is optimised directly using the Covariance Matrix Adaptation Evolution Strategy algorithm. This optimisation algorithm does not have constraint handling, and to include constraints an adaptive penalty function is created. The optimised airfoils are compared to airfoils developed at Delft University, which are considered state of the art for the outer part of a MW class wind turbine rotor blade. Compared to the Delft designs, the airfoils optimised using the CMA-ES algorithm, in combination with the adaptive penalty function, are shown to have equal or improved performance. In addition, it is shown that the adjustments performed to the XFOIL code improve the prediction for both the maximum lift, post stall and the overall drag.

In Paper C, a winglet optimisation method is developed, and tested for a model-scale wind turbine. Here, the turbine performance is simulated by solving the incompressible Navier-Stokes equations and the turbulent flow is predicted using the Spalart Allmaras turbulence model. Since this is a computational expensive approach, the best performing winglet shape is obtained by constructing a Kriging surrogate model. To refine the surrogate, an infill criterion based on expected improvement is maximised using a hybrid genetic-gradient algorithm. In the optimisation, the winglet is parametrised using 6 design variables and 100 shapes are tested. The simulated performance is validated by performing experiments in the NTNU wind tunnel. It is shown that the optimisation method is able to find a winglet which increases the power coefficient for the turbine by 7.8% numerically. In the wind tunnel experiments the winglet is found to increase the turbine power by 10.3%. Further, to analyse the rotor blade with the optimised winglet additional simulations are performed using an Elliptic Blending Reynolds-Stress Model. In this study it is shown that the winglet reduces the induced drag and improves the turbine power mainly by increasing the lift locally in the tip region of the rotor blades.

Future work

The design methods developed in this thesis, which use evolutionary computation to optimise airfoils and winglets for wind turbine application, are independent of turbine size and operational conditions. Further, the design tools are not limited only to wind turbines and the methods could be implemented in the design of other aerodynamic applications. In future work, the two-dimensional direct optimisation using the CMA-ES algorithm should be expanded to three-dimensions by simulating the aerodynamic performance using a 3d-panel code with strong viscous-coupling. Then, the design method could be used to optimise not only the airfoils, but also the shape of the wing or rotor blade. In order to maximise the performance, the optimisation should also consider the full operational condition. For flow problems, which require the solution of the Navier-Stokes equations, the Kriging surrogate model is of particular interest, since it allows optimisation of computational expensive and accurate solutions. Future studies should therefore include constraints in the Kriging optimisation and simulate the aerodynamic performance using a numerical analysis tool that captures the flow physics accurately. To accomplish the latter, the aerodynamic performance could be simulated using low and high fidelity models, and a co-Kriging surrogate should be applied to reduce the numerical cost.

References

[1] S. Koziel and X.-S. Yang. *Computational optimization, methods and algorithms*. Springer-Verlag, Berlin Heidelberg, 2011.

[2] G. S. Hornby, A. Globus, D. S. Linden, and J. D. Lohn. Automated antenna design with evolutionary algorithms. In *Space 2006*, San Jose, California USA, September 19–21 2006. AIAA 2006-7242.

[3] J. F. Manwell, J. G. McGowan, and A. L. Rogers. *Wind Energy Explained*. John Wiley & Sons, 2002.

[4] A. Forrester, A. Sóbester, and A. Keane. *Engineering design via surrogate modelling*. John Wiley & Sons, 1st edition, 2008.

[5] MathWorks Inc. *Global Optimization Toolbox User's Guide, R2015b*, 2015.

[6] N. Hansen. *The CMA Evolution Strategy: A Tutorial*. Research Centre Saclay-Île-de-France, Université Paris-Saclay, April 2016.

[7] A. Keane and P. B. Nair. *Computational approaches for aerospace design*. John Wiley & Sons, 1st edition, 2008.

[8] J. M. Parr, C. M. E. Holden, A. I. J. Forrester, and A. J. Keane. Review of efficient surrogate infill sampling criteria with constraint handling. In *2nd International Conference on Engineering Optimization*, Lisbon, Portugal, September 2010.

[9] M. Drela. *Flight vehicle aerodynamics*. The MIT Press, 2014.

[10] M. O. L. Hansen. *Aerodynamics of Wind Turbines*. Earthscan, London, UK, 2nd edition, 2008.

[11] J. N. Sørensen, R. F. Mikkelsen, D. S. Henningson, S. Ivanell, S. Sarmast, and S. J. Andersen. Simulation of wind turbine wakes using the actuator line technique. *Philos Trans A Math Phys Eng Sci*, 373(2035), January 2015. doi: 10.1098/rsta.2014.0071.

[12] F. Thomas. *Fundamentals of Sailplane Design*. College Park Press, Silver Spring, Maryland USA, 1999.

[13] J. L. Tangler and D. M. Somers. Status of the Special-Purpose airfoil families. Technical Report TP-3264, SERI, 1987.

[14] W. A. Timmer and R.P.J.O.M. van Rooij. Summary of the Delft University wind turbine dedicated airfoils. *Journal of Solar Energy Engineering*, 125(4):488–496, 2003. doi:10.1115/1.1626129.

[15] M. D. Maughmer. Design of winglets for high-performance sailplanes. *Journal of Aircraft*, 40(6):1099–1106, 2003.

[16] W. Freitag and E. T. Schulze. Blended winglets improve performance. *AERO-MAGAZINE*, 35(03), 2009.

[17] M. Gaunaa and J. Johansen. Determination of the maximum aerodynamic efficiency of wind turbine rotors with winglets. *Journal of Physics*, (Conference series 75 (2007)), 2007. doi:10.1088/1742-6596/75/1/012006.

Division of work between authors

Paper A

Hansen was responsible for the computational analysis and measurements of the Std Cirrus glider geometry. The evaluation and comparison of results was performed by Hansen.

Paper B

Hansen was responsible for the development of the optimisation methodology. The evaluation and validation of results was performed by Hansen.

Paper C

Hansen was responsible for the optimisation and computational analysis. The experimental testing was performed by Mühle. The evaluation and validation of the numerical results was performed by Hansen. The paper was written by Hansen.

Paper A

Modeling the Performance of the Standard Cirrus Glider using Navier-Stokes CFD

Thomas H. Hansen
Norwegian University of Science and Technology
N-7491, NTNU Trondheim, Norway and CMR Prototech, Bergen, Norway
thomas.h.hansen@ntnu.no

Abstract

The performance of the Standard Cirrus glider is simulated using a Computational Fluid Dynamics code, solving the incompressible Navier-Stokes equations for steady flow. To calculate the transitional boundary layer flow a correlation-based transition model is used. It is found that the numerical model is able to predict the performance of the Standard Cirrus well. The simulations using the transition model are found to improve the results compared to fully turbulent simulations, except for the region of the stall. The best in-flight measured glide ratio for the Standard Cirrus is 36.5 at 94.5 km/h. The simulations using the transition model predict a best glide ratio of 38.5 at 95 km/h.

1. Introduction

The development of modern computer tools has led to a revolution in the design and construction of high-performance gliders. Today, the aerodynamic and the structural potential of new designs can be investigated and refined using computers to produce gliders with performance and handling qualities inconceivable just a few decades ago. The JS1, ASG29 and the Diana 2 are examples of modern gliders developed by using the latest computational tools in combination with experience and experimental testing. Glide ratios above 50:1 and maximum speeds higher than 280 km/h are today normal for gliders having 15 and 18 meter of wing span. However, modern numerical tools stand in sharp contrast to the methods applied for the design of the first high-performance gliders. Some 30 years ago the tools available consisted almost entirely of analytic approximation methods, wind tunnel experiments and flight testing. The materials and the accuracy of the production methods available at the time were also limiting factors in the quest to develop high-performance gliders.

In this paper, the Standard Cirrus glider is simulated by solving the Reynolds-Averaged Navier-Stokes (RANS) equations in the commercial computational fluid dynamics (CFD) software STAR-CCM+ [1]. The main purpose of the study is to create a validated reference model for the performance of the glider in steady level flight. To predict the important boundary layer flows, the correlation-based γ–Re_θ transition model is used [2, 3]. The results obtained in this work should enable future investigations regarding possible performance and handling quality enhancements for the glider. The design of new winglets, the installation of an electrical engine and research on new turbulator technology are examples of studies that could benefit from using a validated RANS model. The model of the Standard Cirrus is also intended to be a reference model for investigating and refining the results from other numerical simulation tools. The abilities and limitations of less computationally expensive tools such as lifting line methods, vortex-lattice codes, and potential flow solvers can all be evaluated better by comparing the results to a validated Navier-Stokes model.

To perform the simulations, the geometry of the specific Standard Cirrus named LN-GTH is first measured using a digitizing arm and a surface model is created. Then, the performance of the airfoil used at the outer part of the Cirrus wing is analyzed using a two dimensional mesh. The simulations are performed to investigate the accuracy of the γ–Re_θ transition model in detail. The two dimensional computations are validated by comparing the results to experimental values from the low-turbulence pressure wind tunnel at NASA Langley. Finally, the three dimensional model of the Standard Cirrus is simulated in steady level flight for velocities from 90 km/h to 160 km/h. The three dimensional CFD simulations are validated by comparing the results to flight tests performed with a Standard Cirrus at the Idaflieg summer meeting in 2011.

2. The Standard Cirrus

The Standard Cirrus (Figure 1) was designed by Dipl.-Ing. Klaus Holighaus at the Schempp-Hirth factory and flew for the first time in March 1969. The glider is a 15-m design without flaps and was originally built to compete in the Standard Class. The glider uses an all-moving tailplane, is equipped with air brakes on the upper surface of the wings, and can carry 80 kg of water ballast to increase the flight performance. The wing of the glider is designed using two different airfoils, where the root airfoil blends linearly into the airfoil that is used at the outer part of the wing. This outer airfoil is kept constant from the start of the aileron to the tip of the wing. The

best glide ratio for the glider is about 37:1 and the maximum speed is 220 km/h. The glider is known for its good handling qualities, large cockpit and ability to climb well in turbulent thermals. Today, the Standard Cirrus is considered to be one of the best gliders for participating in club class competitions.

Figure 1: The Standard Cirrus. Lennart Batenburg, with permission.

3. Method

In the following, the methods used to perform the simulations of the Standard Cirrus are presented. First, the approach used to perform the measurements of the glider geometry is explained. Then, the numerical approach used to investigate the performance of the Standard Cirrus in both two and three dimensions is given.

3.1. Measurements of the glider geometry

To perform a qualitative analysis of the flight performance for the Standard Cirrus the 'as built' geometry is measured on a specific Standard Cirrus named LN-GTH. To reproduce the glider geometry, the airfoil on both the wing, elevator and rudder is measured using a digitizing arm. The wing is measured at the root, the start of the aileron, and at the tip of the wing. Tail-section measurements are performed at the largest and smallest chord, respectively. By fixing stainless steel shims to the surface of the wing and tail at the measurement stations a straight edge is created and used to guide the

digitizing arm. In Figure 2, the digitizing arm used for the measurements is depicted. The digitizing arm is operated in combination with a surface Computer Aided Design (CAD) tool [4] and about 200 points are captured for each measurement. To increase the accuracy, five measurement series are taken for each airfoil geometry. Then, final splines of the airfoils are created in a two dimensional panel code [5] using the averaged measured data. The chord lengths of the wing and tail at the chosen stations are also measured using a 1-m digital caliper gauge. All other measurements of the glider, such as the position of the wing to fuselage fairing, height of the tail, etc., are taken using a handheld laser. Factory drawings are used as reference. The fuselage, however, is defined by modifying a CAD model which has been used to perform a similar CFD simulation of the Standard Cirrus using the TAU code at the German Aerospace Center (DLR) [6].

Figure 2: Microscribe digitizing arm.

3.2. Navier Stokes solver

The simulations of the Standard Cirrus are performed using the parallelized flow solver STAR-CCM+. The program is designed to take on all aspects of the CFD process, and tools enabling both CAD design and post-processing of the results are implemented. The meshing technology is automated and is capable of creating both a tetrahedral, polyhedral and trimmed hexahedral mesh in a Cartesian coordinate system. A wide range of turbulence models is available, including the k–ω SST turbulence model of Menter [7] which

is a prerequisite for applying the γ–Re$_\theta$ transition model [1]. To solve the RANS equation for the simulations of the Standard Cirrus, the segregated solver in STAR-CCM+ is used. The flow field is modeled using a constant density model and the air is considered to be steady and incompressible. The turbulent flow is modeled with the k–ω SST turbulence model, and the transition locations are predicted using the γ–Re$_\theta$ transition model. All simulations are performed on a Dell power blade cluster running 36 CPUs in parallel.

3.3. The γ–Re$_\theta$ transition model

The laminar-turbulent transition process is important when predicting the performance of gliders. For Reynolds numbers below 3 million, this transition process often takes the form of a laminar separation bubble. When this occurs, the separating laminar layer is followed by turbulent reattachment, just behind a recirculation region. In Figure 3 an illustration of the transition process on the upper side of an airfoil is shown.

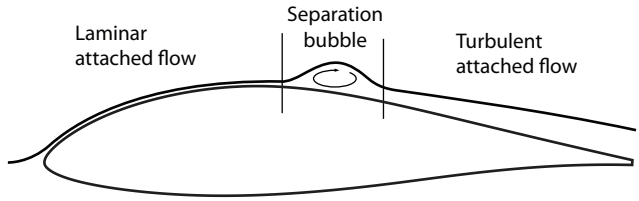

Figure 3: Laminar separation bubble.

The γ–Re$_\theta$ transition model used in this study is a correlation-based transition model that solves two extra transport equations, one for intermittency, γ, and one for the local transition onset momentum thickness Reynolds number, Re_{θ_t}. The model relates the local momentum thickness Reynolds number, Re_θ, to the critical value, Re_{θ_c}, and switches on the intermittency production when Re_θ is larger than the local critical value. The only input the model requires is the definition of the location for the free-stream edge. This means that a distance from the wall of the geometry has to be estimated to ensure that the entire boundary layer is captured [1]. A high-quality, refined, low-Reynolds number mesh is required for using the γ–Re$_\theta$ transition model. One important parameter defining the mesh quality is the distance from the wall boundary to the first cell centroid in the mesh. This distance determines how the boundary layer is resolved by the

turbulence model, and is defined by the y^+ value

$$y^+ = \frac{yu^*}{\nu} \ , \tag{1}$$

where y is the normal distance from the wall to the first cell-centroid, u^* is the frictional velocity at the nearest wall and ν is the kinematic viscosity. To enable the γ–Re_θ transition model to converge, the y^+ values need to be in the region 0.1 to 1, and the growth rate and stream-wise mesh spacing in the transition area needs to be fine enough to capture the laminar separation bubble [3]. By performing the simulations as fully turbulent, the transition process is ignored and only turbulent air-flow is present in the boundary layer.

3.4. Two dimensional calculations

To investigate the accuracy of the γ–Re_θ transition model, the performance of the airfoil used on the outer part of the Standard Cirrus wing is investigated in two dimensions. The simulations are validated by comparing the results to experimental data from the low-turbulence, pressure wind tunnel at NASA Langley [8]. The simulated airfoil geometry is obtained from the NASA experiment performed in 1977, and is believed to be from a Standard Cirrus wing. Hence, the performance of the newly refinished LN-GTH airfoil can be compared to measurements of the original airfoil geometry. The mesh quality required to obtain a mesh independent solution using the γ–Re_θ model is taken from previous work, where a mesh dependency study was performed [9]. The interesting angles of attack, α, are calculated using an O-mesh that is constructed with a hyperbolic extrusion method using a structured mesh tool [10]. To create a pressure outlet boundary the downstream far-field edge is cut at 40 and 110 degrees. Upstream, a velocity inlet boundary is used. In Figure 4 an example of the O-mesh is shown.

To reproduce the flow condition in the test section of the NASA wind tunnel, the turbulent intensity and turbulent viscosity ratio is defined. The value for the turbulent intensity is found from [11] to be 0.02% and a turbulent viscosity ratio of 10 is used. The correct values applied to the inlet boundary are calculated using the turbulence decay laws for the k–ω SST turbulence model [1]. All simulations are performed for a Reynolds number of 1.5 million. To ensure a converged solution a drop in accuracy to the fourth decimal is used as stopping criterion for all residuals. In addition, an asymptotic stopping criterion for the monitored coefficients, C_l and C_d is used to ensure a bounded accuracy on the fifth decimal for the last 50

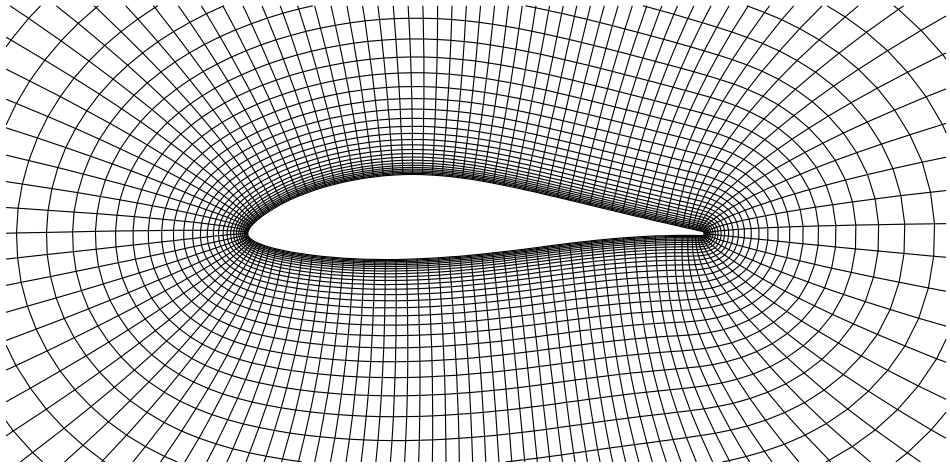

Figure 4: Hyperbolic extruded O-mesh.

iterations. For all calculations the free-stream edge definition for the γ–Re_θ model is put at 25 mm from the airfoil surface. Fully turbulent simulations are also performed and used as reference to the transition model investigations. The mesh criteria for the fully turbulent simulations are taken from previous work performed on wind turbine blades [9]. The results from the two dimensional simulations are also compared to calculations performed using the panel codes XFOIL [12] and RFOIL [13]. To match the turbulence level, an Ncrit value of 12 is used in the panel codes.

3.5. Three dimensional calculations

In steady level flight the lift produced by an aircraft needs to equal the weight. For a glider this situation occurs at a steady, unaccelerated descent, where θ is the equilibrium descent glide angle. The lift force in coefficient form is given by

$$C_L = \frac{L}{q_\infty S} = \frac{mg}{q_\infty S} \tag{2}$$

and the drag coefficient is given by

$$C_D = \frac{D}{q_\infty S} \ . \tag{3}$$

Here, m is the mass of the glider, g is the gravitational constant and S is the reference area. The dynamic pressure q_∞ is denoted

$$q_\infty = \frac{1}{2}\rho_\infty V_\infty^2 \ , \tag{4}$$

where ρ_∞ is the density of air and V_∞ is the free-stream velocity. Since the change in Reynolds number due to difference in density at different altitudes is small, the descent glide angle θ can be found from

$$\tan(\theta) = \frac{1}{C_L/C_D} \ . \tag{5}$$

Hence, the descent glide angle θ is only a function of the lift-to-drag ratio, C_L/C_D, and does not depend on altitude or wing loading. However, to achieve a given C_L/C_D at a given altitude, the glider must fly at a specific velocity V_∞ called the equilibrium glide velocity. The value of V_∞ is dependent on both altitude and wing loading [14].

To evaluate the performance of the Standard Cirrus the speed polar is calculated. The polar shows the rate of sink at different free-stream velocities and is found from

$$h = V_\infty \sin(\theta) \ . \tag{6}$$

To validate the three dimensional simulations the speed polar is compared to flight measurements performed for the Standard Cirrus at the Idaflieg summer meeting [15]. The flight data from Idaflieg are provided as calibrated air speed (CAS) using $\rho_0 = 1.225$ kg/m^3 as reference density, and the simulations are therefore also performed using this density. The performance of the glider is investigated at flight speeds between 90 km/h and 160 km/h. These are the steady level flight speeds normally used for the glider. At lower speeds, the glider should normally be circling in thermals, and not be in steady level flight. At higher speeds than 160 km/h, the large increase in sink rate deteriorates the performance of the glider. Hence, it is not preferable to fly at these speeds except when having over-predicted the altitude needed for the final glide.

To simulate the performance of the Standard Cirrus, two CFD models are constructed and calculated. One model is created to simulate the lift and drag coefficients of the wing and fuselage, where the wing, the wing fairing and the fuselage is included. To find the correct angles of attack that produce the needed lift coefficient at the specific velocities, two simulations at different angles of attack are performed. The expected linearity of the lift slope is then used to find the angle of attack that produces the required lift for the glider. To calculate the drag coefficient of the tail section another model is created. This model is constructed with both the fuselage and the tail section present, and has the elevator positioned at zero degrees angle of attack. To account for Reynolds number effects, the drag coefficient of the tail section is simulated for all investigated velocities.

The discretization of the two models is created using an isotropic, trimmed hexahedral mesh in STAR-CCM+. To reduce the number of cells in the mesh, symmetry conditions are applied. Hence, only half the glider is present in the models. The required quality for the three dimensional grids when using the γ–Re_θ transition model is investigated for the different flight conditions. To capture the boundary layer flows, a 20-layer, 30-mm thick body-fitted hyperbolic extruded prism layer is created from the surface of the glider. The mesh outside the prism layer has a growth rate of 1.1. In Figure 5, the wing and fuselage mesh is shown.

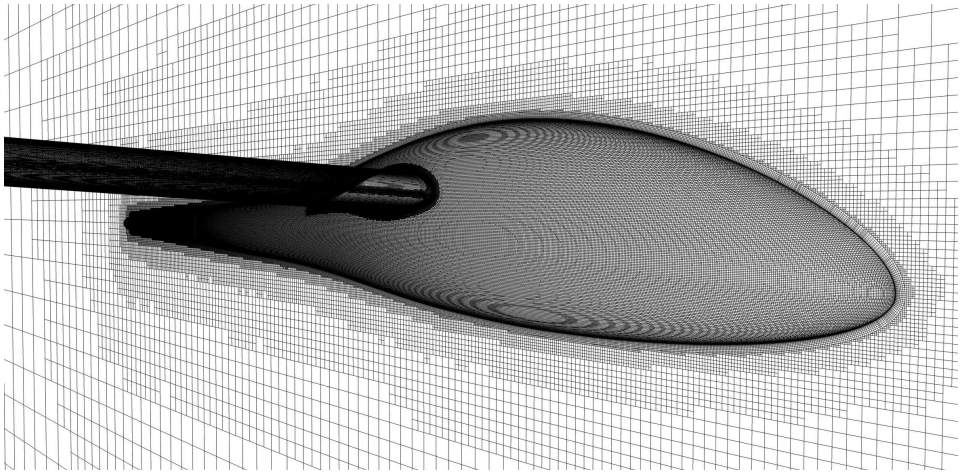

Figure 5: Trimmed hexahedral mesh.

The outer boundary of the flow domain is constructed as a half-sphere, and is positioned 50 m from the glider surface. The domain is split and has a velocity inlet and pressure outlet boundary upstream and downstream of the glider, respectively. A turbulence intensity of 0.1% and a turbulent viscosity ratio of 10, initiated at the inlet boundary, is applied to specify the turbulence in the air-flow for all simulations. Convergence is assumed to be reached when a drop in accuracy to the third decimal is obtained. In addition, an asymptotic criterion is used to ensure that the monitored coefficients C_l and C_d are asymptotically bounded on the fourth decimal for the last 50 iterations. The free-stream edge definition for the simulations with the γ–Re_θ model activated is set to 50 mm. Fully turbulent simulations are also performed and the results are compared to the transition model predictions. To better investigate the difference between the two CFD methods the mesh used for the fully turbulent simulations is the same as for the calculations performed with the γ–Re_θ transition model.

4. Results

In the following, the results from the investigations of the Standard Cirrus glider are presented. First, the measurement of the airfoil geometry from the outer wing of the LN-GTH glider is shown and compared to the original coordinates. Then the results for the two and three dimensional simulations are given.

4.1. Geometry measurement results

The airfoil used at the outer part of the Standard Cirrus wing is found in [16] to be the FX 66-17 A II-182. This airfoil was designed by Dr. F.X. Wortmann at the University of Stuttgart and the original coordinates are obtained from the Stuttgart airfoil catalogue [17]. To investigate the quality of the airfoil on LN-GTH, comparison to both the original airfoil coordinates and to the measurements obtained from the NASA experiment are performed. In Figure 6, the airfoil comparison is shown. The figure is scaled to better visualize the differences between the airfoils. As seen in the figure, the three airfoils do not match exactly. The difference between the original Stuttgart coordinates and the NASA measurements are discussed in [8] and is believed to be due to the fiberglass construction techniques available at the time of production. The airfoil geometry from the LN-GTH measurements can be seen to fit the NASA airfoil better than the Stuttgart coordinates. The largest difference between the LN-GTH and the NASA

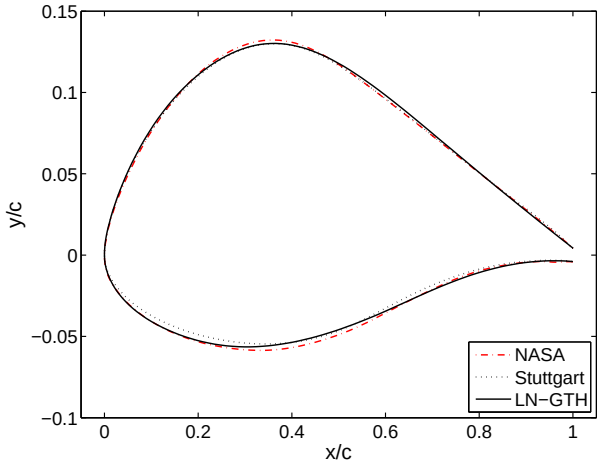

Figure 6: Comparison of FX 66-17 A II-182 airfoils.

airfoil is found at the thickest part of the airfoil geometry. This difference is believed to be caused by refinishing the gelcoat on the 34-year-old LN-GTH glider.

4.2. Two dimensional results

The O-mesh with the smallest number of cells that enables the γ–Re$_\theta$ model to converge for all investigated angles of attack is taken from a mesh dependency study performed in previous work [9]. This mesh has 600 cells wrapped around the airfoil, a growth rate of 1.05 and y^+ values below 1 for all simulated angles of attack. By reducing the number of cells on the airfoil it is found that the range of angles of attack possible to simulate is also reduced. In Figure 7, the results for the lift and drag coefficient from the two dimensional investigations are given. The left figure shows the lift coefficient versus the angle of attack. Here, the predictions from the CFD simulations using the transition model can be seen to compare well to the experimental data. The results using the transition model predict the lift coefficient equally well as the panel codes XFOIL and RFOIL for the angles of attack between -5 and $+5$ degrees. For higher angles of attack the tran-

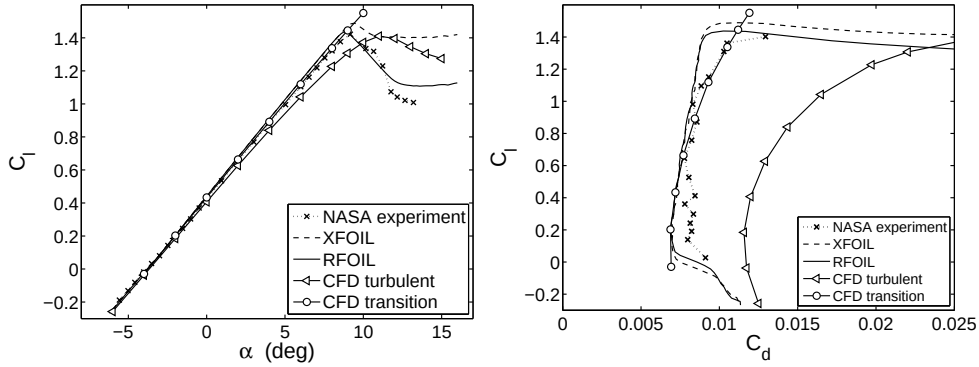

Figure 7: Comparison of lift coefficient versus angle of attack (left) and versus drag coefficient (right), respectively.

sition model compares better to the experimental data than to the results from the panel codes. However, the transition model is unable to simulate the occurrence of the stall and the lift coefficient is over-predicted in this region. The fully turbulent CFD model can be seen to underestimate the lift coefficient for all positive angles of attack. Interestingly, the RFOIL calculations can be seen to capture the occurrence of the stall better than the XFOIL simulations. The right figure shows the lift coefficient C_l versus the

drag coefficient C_d. Here, the predictions from the CFD simulations using the transition model can be seen to compare well to the experimental data. The transition model performs equally well as the panel codes for predicting the drag coefficient at C_l values from zero to 0.6. For higher C_l values, the drag predictions using the transition model compares better to the experimental data than the XFOIL and RFOIL results. The fully turbulent CFD model can be seen to over-predict the drag coefficient heavily for all values of C_l.

In Figure 8, the pressure coefficient for the airfoil at angles of attack 0 and 8.05 degrees is given. By comparing the predictions from the k–ω SST model, the γ–Re_θ transition model and the XFOIL and RFOIL codes to experimental values, the performance of the different methods can be investigated in detail. In the left figure the pressure coefficients for $\alpha = 0$ degrees are depicted. At this low angle of attack only a small difference in pressure can be observed between the fully turbulent and the transition model compared to the experimental values. However, the transition model predicts the pressure slightly better on the front part of the airfoil suction side, and is also able to predict the position of the laminar separation bubbles with good accuracy. The turbulent CFD model only models the air-flow around the airfoil as turbulent and no transition is predicted. Compared to the panel codes the transition model predicts the pressure on the airfoil equally well. However, a small difference can be seen after the location of the laminar separation bubbles, which are predicted to be both larger in size and slightly further back on the airfoil for the panel codes. In the right figure the pressure coefficients for $\alpha = 8.05$ degrees are compared. As can be seen, the pressure on the airfoil is under-predicted using the turbulent CFD

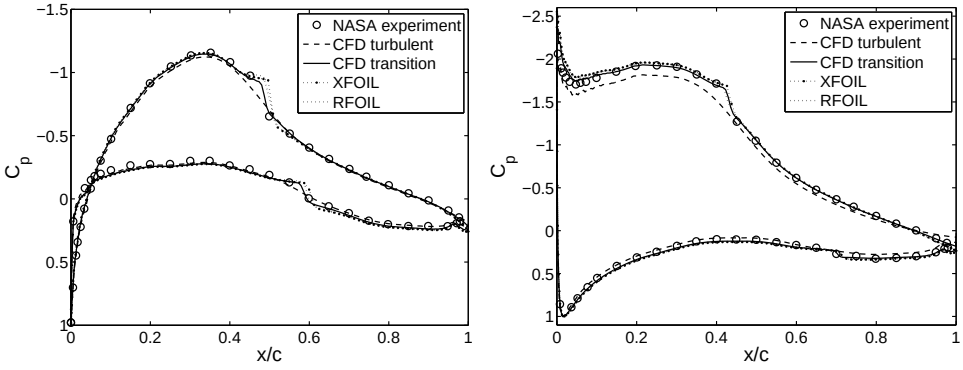

Figure 8: Pressure coefficient distribution comparison, $\alpha = 0$ degrees (left) and $\alpha = 8.05$ degrees (right).

model. Specially, in the laminar region on the front part on the suction side of the airfoil the pressure is too low. It is found that by not accounting for the laminar flow present on the airfoil, this error in predicting the pressure increases for higher angles of attack. This is the reason for the lift being increasingly under-predicted at higher angles of attack in Figure 7. The transition model, on the other hand, is able to predict the laminar air-flow in this region and the pressure compares well to the experimental data. The transition model predicts the position of the laminar separation bubbles accurately also for this flow condition. Compared to the panel codes the transition model calculates the pressure on the airfoil slightly better. The panel codes can be seen to over-predict the pressure in the region on the front part on the suction side of the airfoil. For the investigated flow conditions, the only difference between the XFOIL and the RFOIL code is the small deviation found in the transition predictions.

In Figure 9, the difference in production of turbulent kinetic energy at zero angle of attack using the k–ω SST model and the γ–Re_θ transition model is visualized. As can be seen in the top figure, no laminar flow exists when simulating the airfoil using the fully turbulent model. The production of turbulent kinetic energy is initiated at the leading edge of the geometry

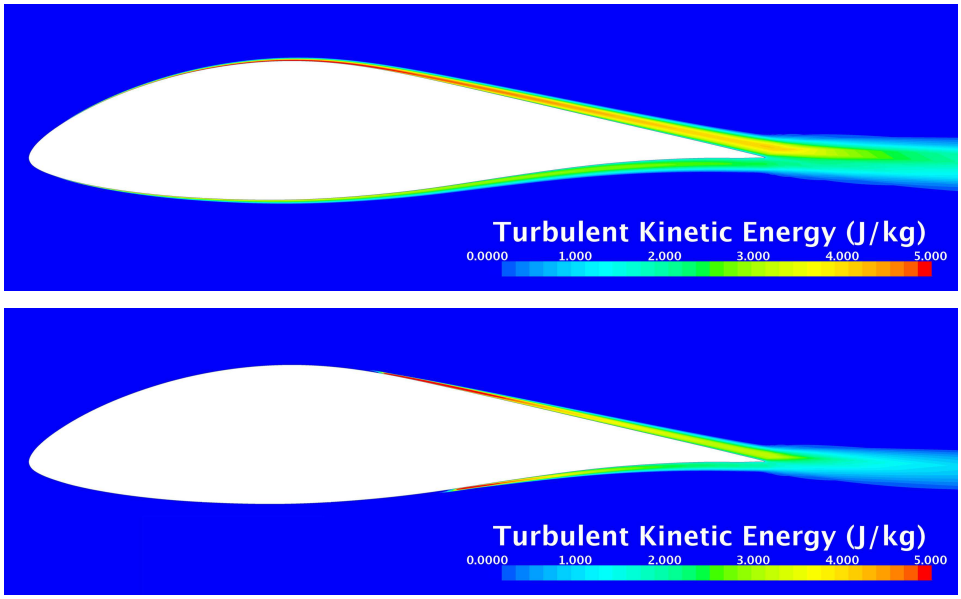

Figure 9: Turbulent kinetic energy prediction at $\alpha = 0$ degrees for turbulent model (top) and transition model (bottom).

and increases in size along the length of the airfoil. In the bottom figure the equivalent transition model simulation is depicted. Here, the region of laminar air-flow that exists on the front part of the airfoil is captured and the production of turbulent kinetic energy begins at the reattachment point, after the laminar separation bubble.

In Figure 10, the production of turbulent kinetic energy at $\alpha = 8.05$ degrees is visualized. Here, the difference in production of turbulent kinetic energy between the fully turbulent (top) and the transition model (bottom) simulation is much larger compared to the zero angle of attack simulations.

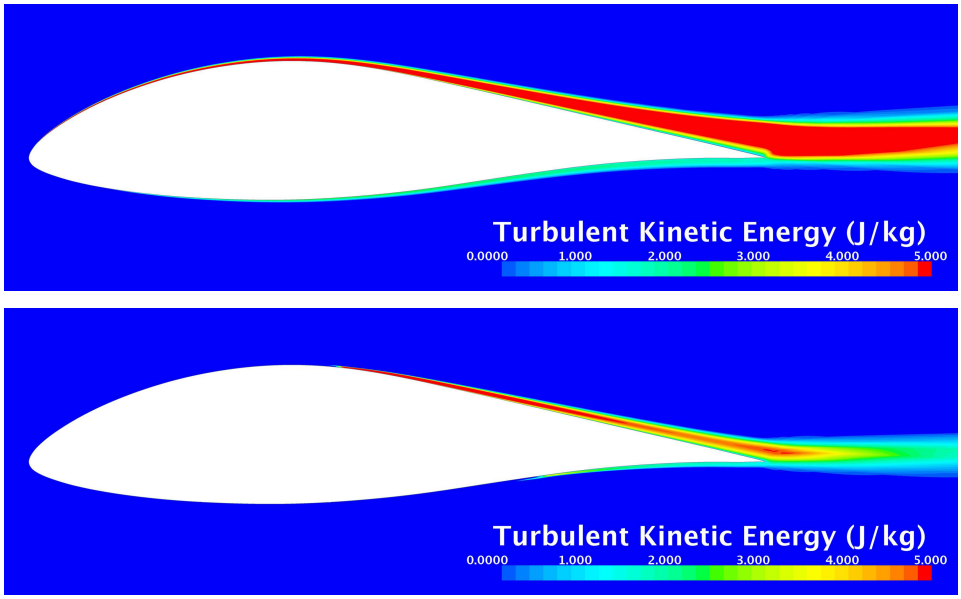

Figure 10: Turbulent kinetic energy prediction at $\alpha = 8.05$ degrees for turbulent model (top) and transition model (bottom).

Hence, by performing the simulations using the fully turbulent model, the over-production of turbulent kinetic energy increases for higher angles of attack. This is the cause of the increased over-prediction in drag for high lift coefficients in Figure 7. For the transition model simulation, the production of turbulent kinetic energy is smaller. By including the laminar flow region on the airfoil, the transition model predicts the flow condition more correctly, which enables better drag predictions.

In Figure 11, the results for the position of the transition are given. As can be seen in the figure, the position of the laminar separation bubble using the γ–Re_θ transition model compares well to the experimental data. The

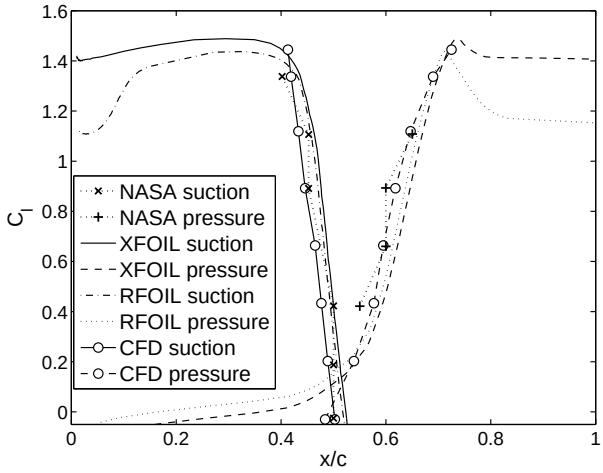

Figure 11: Airfoil transition position.

prediction using the XFOIL and RFOIL codes can be seen to be slightly further back on the airfoil on both the suction and pressure side. The transition location for both the γ–Re_θ model and the panel codes are compared to the experimental data at the reattachment point where transition to turbulent flow occurs.

Finally, a comparison of the lift-to-drag ratio for the NASA airfoil measured in 1977 and the LN-GTH airfoil is depicted in Figure 12. Here, both results are obtained using the RFOIL code and indicate a slightly better performance for the LN-GTH airfoil at angles of attack below 8 degrees for the investigated flow condition.

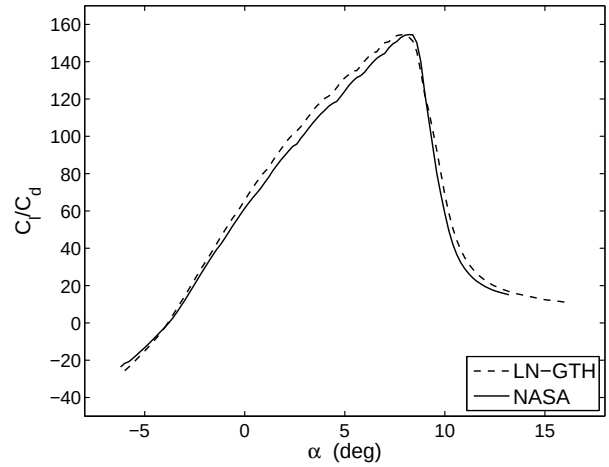

Figure 12: Performance comparison LN-GTH and NASA airfoil.

4.3. Three dimensional results

In Figure 13, the constrained streamlines and the production of turbulent kinetic energy on the top side of the Standard Cirrus are visualized. As can be seen in the figure, the transition model is able to predict both the occurrence of the laminar separation bubble and the transition from laminar to turbulent air-flow on both the wings and the fuselage of the glider. To the left in the figure a free-stream velocity of 95 km/h is applied. At this velocity the transition process starts approximately at the mid-chord along the span of the wing. The laminar separation bubble can be seen as the region where the streamlines are halted and the turbulent reattachment region, followed by turbulent attached flow is predicted by the production of turbulent kinetic energy. To the right in the figure the 160 km/h simulation is depicted. At this velocity the position of the transition is moved slightly backwards compared to the 95 km/h simulation. Due to the higher Reynolds number on the inboard part of the wing no laminar separation bubble is visible in this region and the transition process forms directly to turbulent flow. On the outer part of the wing the Reynolds number is gradually decreased and a linearly growing laminar separation bubble is formed towards the tip. The amount of turbulent kinetic energy is also increased for this flight velocity due to the increase in profile drag.

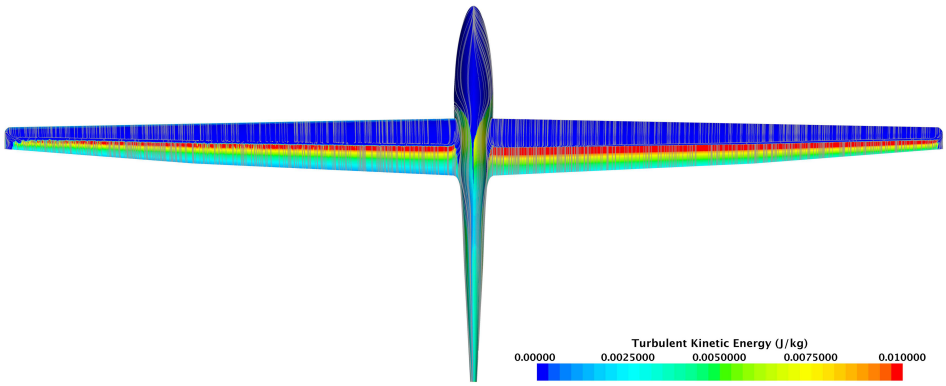

Figure 13: Top side transition, left 95 km/h, right 160 km/h.

In Figure 14, the constrained streamlines and the production of turbulent kinetic energy on the bottom side of the Standard Cirrus is shown. For the 95 km/h simulation (left in figure) the transition from laminar to turbulent flow on the bottom side starts slightly behind the mid-chord along the span of the wing. A large laminar separation bubble is predicted and the

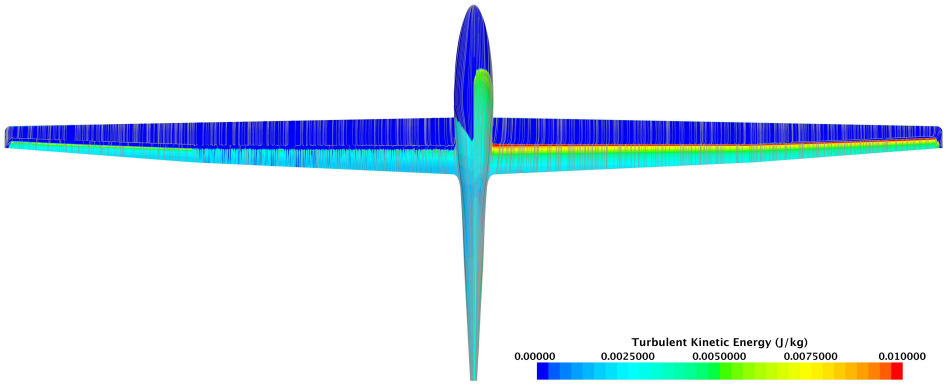

Figure 14: Bottom side transition, left 95 km/h, right 160 km/h.

production of turbulent kinetic energy is lower than on the suction side. For the 160 km/h simulation (right in figure) the position of the transition is moved slightly forward compared to the 95 km/h simulation. Again, most of the transition forms directly to turbulent flow, and only on the outboard part of the wing a linearly growing laminar separation bubble is predicted due to the decrease in Reynolds number. The higher profile drag compared to the 95 km/h simulation can be seen by the larger production of turbulent kinetic energy for this simulated velocity. Interestingly, the transition model predicts little production of turbulent kinetic energy in the region of the vortex at the tip of the wing for both simulated velocities.

The constrained streamlines and the production of turbulent kinetic energy on the fuselage of the Standard Cirrus is visualized in Figure 15. In the top figure the transition position for the 95 km/h simulation is shown. Here, the transition from laminar to turbulent can be seen to occur slightly before the wing-fuselage fairing. In the bottom figure the production of turbulent kinetic energy for the 160 km/h simulation is shown. Due to the higher velocity and smaller angle of attack at this flight condition the transition has moved forward on the lower side of the fuselage. Hence, both the fuselage shape, the angle of attack and the velocity determines how the transition process develops on the fuselage. It is known that sailplane cockpit ventilation is affected by internal flow resistance within the fuselage, causing air to escape between the canopy frame and the cockpit edge. Depending on the amount of leakage this might trip the laminar boundary layer on the cockpit edge to turbulent flow and increase the profile drag for the fuselage [18]. This phenomena is not captured by the simulations performed in this work. However, the position of the boundary layer transition line for

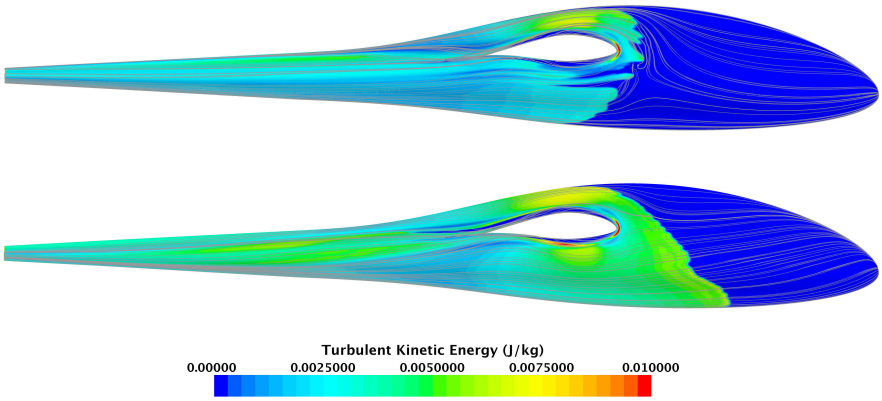

Figure 15: Fuselage transition, top 95 km/h, bottom 160 km/h.

the simulations are found to compare well to measurements found in [16].

In Figure 16, the constrained streamlines and the production of turbulent kinetic energy on the top of the elevator is shown. Again, the trends from the simulations performed on the wings of the glider can be observed. For the 95 km/h simulation, to the left in the figure, the production of turbulent kinetic energy is small and the laminar separation bubble is large. The position of the transition for the 160 km/h simulation to the right in the figure, has moved forward and the production of turbulent kinetic energy is increased due to the increase in profile drag. As for the wing at 160 km/h, the transition bubble is only present at the outer part where the Reynolds number is lower.

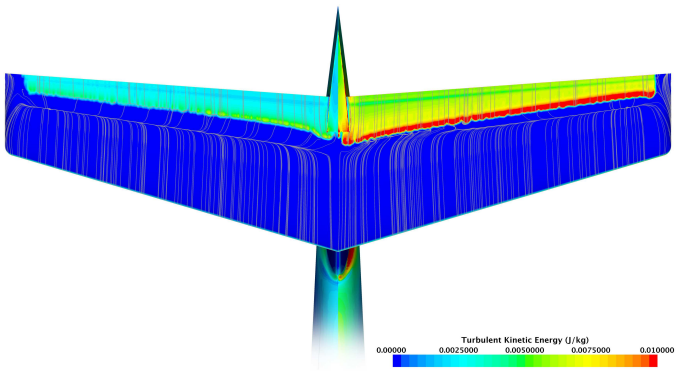

Figure 16: Elevator transition, left 95 km/h, right 160 km/h.

The constrained streamlines and the production of turbulent kinetic energy on the lower side of the elevator and the tail section is shown in Figure 17. To the left in the figure the result from the 95 km/h simulation is depicted and to the right the 160 km/h simulation is visualized. It can be seen that the presence of the fuselage has an impact on the production of turbulent kinetic energy on the tail section, since the turbulent flow condition from the fuselage initiates the transition process almost on the leading edge for the lower part of the fin. Higher up on the fin the inflow condition is less turbulent and the transition occurs later. Also, in the connection

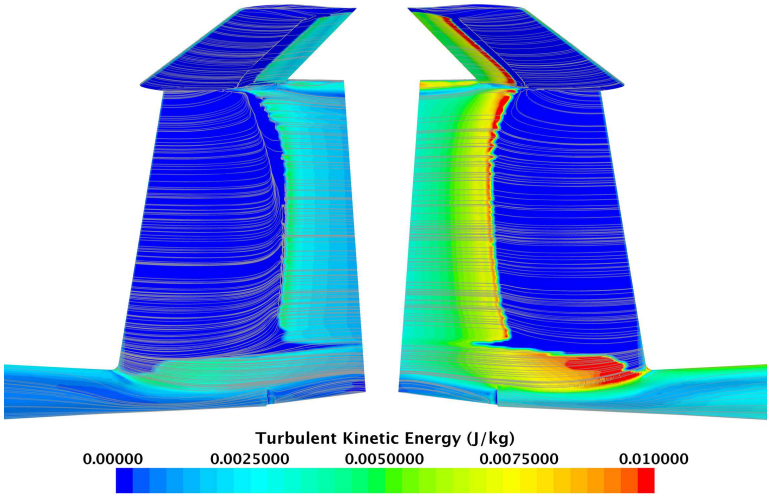

Figure 17: Tail section transition, left 95 km/h, right 160 km/h.

between the elevator and fin more turbulent kinetic energy is produced due to increased interference drag, and the transition point is moved slightly forward. For the 95 km/h simulation a laminar separation bubble can be seen to form about half way up the fin and continues on the lower side of the elevator. For the 160 km/h simulation, however, the laminar separation bubble is only visible on the lower side of the elevator and the transition forms directly to turbulent flow on the fin section. The drag coefficient for the tail section is found to be Reynolds number dependent and a reduction in C_d of about 10% is found for the 160 km/h simulation compared to the 95 km/h simulation.

To obtain converged solutions for the simulations using the γ–Re_θ model the calculated grids are adjusted to fulfil the mesh criteria due to differences in simulated velocities and angles of attack. Since the y^+ value for the mesh

scales with the velocity, the grids at high velocities are adjusted using a smaller distance to the first cell centroid. At angles of attack where the flow is less attached, more cells on the wing are also needed to obtain a converged solution. The number of cells in the mesh for the 90 km/h to the 160 km/h simulation is therefore gradually increased from 28 million to about 42 million cells, respectively. The simulations of the fuselage and tail section mesh have about 7.8 million cells.

In Figure 18, the calculated speed polar for the Standard Cirrus is compared to flight measurements from Idaflieg. The simulations performed using the γ–Re_θ transition model can be seen to compare well to the real flight data. For velocities below 100 km/h the simulations are closely matched to the in-flight measurements. At higher velocities, the sink rates are slightly under-predicted. The measured best glide ratio for the Standard Cirrus from the Idaflieg flight tests is found to be 36.51 at 94.47 km/h. The best glide ratio for the simulations performed using the γ–Re_θ model is found to be 38.51 at 95 km/h. The turbulent calculations of the Standard Cirrus can be seen to heavily over-estimate the drag and consequently the sink rates for all investigated velocities. The difference between the simulated results and the flight measurements also increase at higher flight speeds. This is because the friction drag on the glider is increasingly over-predicted since no laminar flow is present in the model. The best glide ratio for the fully turbulent simulations is found to be 28.96 at 90 km/h.

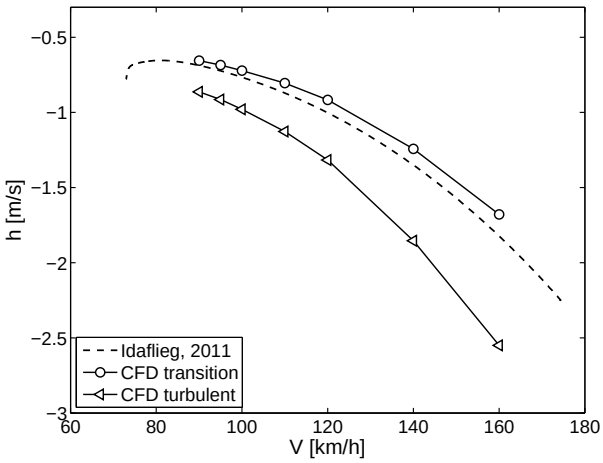

Figure 18: Standard Cirrus speed polar comparison.

In Table 1, the angles of attack for the Standard Cirrus simulations are given. The zero angle of attack position for the CFD models of the glider is referenced to the weighing position as found in the flight and service manual [19]. As can be seen in the table, higher angles of attack are required to sustain steady level flight when performing the simulations as fully turbulent compared to using the γ–Re_θ transition model.

Table 1: Input data for CFD simulations.

V_∞	$[km/h]$	90	95	100	110	120	140	160
C_L	[-]	0.911	0.818	0.738	0.610	0.512	0.376	0.288
α_{trans}	[deg]	2.663	1.770	1.013	-0.207	-1.128	-2.396	-3.220
α_{turb}	[deg]	3.265	2.274	1.472	0.169	-0.805	-2.133	-2.992

5. Conclusions

In this study the performance of the Standard Cirrus glider is simulated using the computational fluid dynamics code STAR-CCM+. The turbulent flow is modelled using the k–ω SST turbulence model and the transition locations are automatically predicted using the γ–Re_θ transition model. To investigate the performance of the γ–Re_θ model, calculations on a Cirrus airfoil are first performed using a two dimensional grid. The final three dimensional simulations of the glider are validated by comparing the results to recent flight measurements from Idaflieg. It is found that the numerical model is able to predict the performance of the glider well. For low angles of attack, the γ–Re_θ transition model improves the results for the lift and drag prediction of the glider compared to fully turbulent calculations. For high angles of attack the γ–Re_θ transition model is unable to converge. The best glide ratio for the Standard Cirrus from the flight tests is measured to be 36.51 at 94.47 km/h. For the simulation using the γ–Re_θ transition model the best glide ratio is calculated to be 38.51 at 95 km/h. For the fully turbulent simulations the best glide ratio is predicted to be 28.96 at 90 km/h. The large deviations in the prediction of the performance when using fully turbulent simulations are due to the absence of laminar flow in the boundary layer of the glider.

By accounting for the drag due to air leakage from the cockpit edges, as well as the drag from the tail-skid and wing tip skids, the results from the simulations using the γ–Re_θ transition model could be further improved. In particular, the drag of the tail in this work is simulated using a simplified

model where the elevator is positioned at zero angle of attack. By accounting for the extra induced drag due to the elevator deflection needed to sustain steady level flight, the results should be improved. Future studies should investigate the drag production from the glider in more detail and focus on applying the γ–Re_θ transition model for high angles of attack.

6. Acknowledgments

The author wishes to thank Dipl.-Ing. Falk Pätzold at the Technische Universität Braunschweig for providing the experimental data from the Standard Cirrus flight tests. Also, thanks to Ing. Bernt H. Hembre and Graeme Naismith for their help with measuring the glider geometry and to Dr. Gloria Stenfelt for her support throughout this study.

References

[1] CD-Adapco. *Introducing STAR-CCM+*, 2017. User guide, STAR-CCM+ version 12.02.010.

[2] R. B. Langtry and F. R. Menter. Correlation-based transition modeling for unstructured parallelized computational fluid dynamics codes. *AIAA Journal*, 47(12):2894–2906, 2009.

[3] P. Malan, K. Suluksna, and E. Juntasaro. Calibrating the γ–Re_θ transition model for commercial CFD. In *47th AIAA Aerospace Sciences Meeting including The New Horizons Forum and Aerospace Exposition*, January 2009.

[4] Robert McNeel and Associates. *Rhinoceros NURBS modeling for Windows*, 1993–2008. User's Guide, Version 4.0.

[5] XFLR5. analysis of foils and wings operating at low Reynolds numbers., February 2014. Guidelines for XFLR5 v6.03.

[6] S. Melber-Wilkending, G. Schrauf, and M. Rakowitz. Aerodynamic analysis of flows with low Mach- and Reynolds-number under consideration and forecast of transition on the example of a glider. In *14th AG STAB/DGLR Symposium*, Bremen, November 2004.

[7] F. R. Menter. Two-equation eddy-viscosity turbulence models for engineering applications. *AIAA Journal*, 32(8):1598–1605, 1994.

[8] D. M Somers. Experimental and theoretical low-speed aerodynamic characteristics of a wortmann airfoil as manufactured on a fiberglass sailplane. Technical Report TN 0-8324, NASA, February 1977.

[9] T. Hansen. Wind turbine simulations using Navier-Stokes cfd. Master's thesis, Royal Institute of Technology, Aeronautical and Vehicle Engineering, July 2010.

[10] Pointwise, Inc. *Pointwise, reliable CFD meshing*, 2014. User manual, version 9.02.

[11] A. E. von Doenhoff and F. T. Abbot Jr. The Langley two-dimensional low-turbulence pressure tunnel. Technical Report TN 1283, NASA, 1947.

[12] M. Drela and H. Youngren. Xfoil 6.9 user primer. Technical report, Massachusetts Institute of Technology, November 2001. http://web.mit.edu/drela/Public/web/xfoil/.

[13] B. O. G. Montgomerie, A. J. Brand, J. Bosschers, and R. P. J. O. M. van Rooij. Three-dimensional effects in stall. Technical Report ECN-C-96-079, NREL, TUD, June 1997.

[14] J. D. Anderson Jr. *Aircraft Perfromance and Design.* McGraw-Hill, 1999.

[15] F. Pätzold. Preliminary results of flight performance determination of Cirrus75 D-6607 S/N 633. Technical report, IDAFLIEG, 2012. Preliminary results from the 2011 IDAFLIEG summer meeting.

[16] F. Thomas. *Fundamentals of Sailplane Design.* College Park Press, Silver Spring, Maryland USA, 1999.

[17] D. Althaus and F. X. Wortmann. *Stuttgarter Profilkatalog I.* Institut für Aerodynamik und Gasdynamik, Stuttgart, 2011.

[18] A. S. Jonker, J. J. Bosman, E. H. Mathews, and L. Liebenberg. Flow over a glider canopy. *The Aeronautical Journal*, 118(1204):669–682, June 2014.

[19] Schempp-Hirth K. G., Kircheim-Teck. *Flight and Service Manual for the Sailplane Standard Cirrus*, 1969.

Paper B

Airfoil Optimisation for Wind Turbine Application

Thomas H. Hansen
Norwegian University of Science and Technology
N-7491, NTNU Trondheim, Norway and CMR Prototech, Bergen, Norway
thomas.h.hansen@ntnu.no

Abstract

An airfoil optimisation method for wind turbine applications that controls the loss in performance due to leading edge contamination is developed and tested. The method employs the CST technique to parametrise the airfoil geometry and uses an adjusted version of the panel code XFOIL to calculate the aerodynamic performance. To find optimal airfoil shapes the derivative-free CMA-ES algorithm is used in combination with an adaptive penalty function. The method is tested for the design of airfoils for the outer part of a MW class wind turbine rotor blade, and the results are compared to airfoils from TU Delft. It is found that the method is able to automatically create airfoils with equal or improved performance compared to the Delft designs. For the tested application, the adjustments performed to the XFOIL code improve the maximum lift, post stall and the overall drag predictions.

1. Introduction

A key element towards reducing the cost of energy in the wind turbine industry is the development of airfoils with specialised aerodynamic performance. In modern wind farms the power production is known to reduce over time, and loss in capacity factors of 10 to 15% are reported compared to manufacturer predictions [1]. The main contribution to this loss is believed to be leading edge contamination, which increases the surface roughness on the rotor blades and deteriorates the aerodynamic performance. The contamination is caused by insects, sand, salt, and hail hitting the turbine over time, and depending on the severity of these environmental hazards the rotor blades will eventually experience erosion and need repair [2]. To reduce the loss in power production and revenue from wind turbines, insensitivity to roughness is well recognised as an important design criterion, and specialised wind turbine airfoils addressing this problem have been developed since the mid 1980's [3]. Most of these airfoils, however, have been created using inverse design techniques, where the velocity distribution is specified

to obtain the corresponding airfoil shape at isolated angles of attack. This approach has the disadvantage that only single-point design problems can be handled directly [4]. A method better suited when multiple design points are considered, is numerical optimisation, where the airfoil performance can be maximised within the limits of aerodynamic and geometric constraints using a mathematical algorithm. Research shows that depending on the choice of shape parametrisation technique, flow solver and optimisation algorithm, this approach has the potential to find airfoils with improved performance around multiple design points. In [5], a modified version of the flow solver XFOIL is used in combination with a genetic algorithm to optimise an airfoil for a competition glider aircraft. Here, the design method considers the full operation during a competition flight, and compared to the original airfoil that was created using an inverse design method, the optimised airfoil is able to increase the overall cross country speed for the glider by about 2.5 km/h. In [6], wind turbine airfoils ranging from 12 to 30% thickness are developed using XFOIL and a gradient optimisation method. Here, the loss in aerodynamic performance due to the leading edge contamination is controlled by restricting the design lift coefficient and constraining the transition from laminar to turbulent flow on the airfoil at specific angles of attack.

In this work, an airfoil design method is developed where the loss in performance due to leading edge contamination is controlled by optimising the airfoil shape at multiple design points, both for clean flow conditions and with a turbulated leading edge. To minimise the loss in performance between the two flow scenarios, the allowable loss in lift, the difference in angle of attack for best performance, as well as the minimum allowable lift-to-drag ratio for the airfoil with leading edge transition are controlled. The method uses the Class-Shape Transformation (CST) technique to parametrise the airfoil geometry, and calculates the aerodynamic coefficients using an adjusted version of the XFOIL code. To optimise the airfoil shape, the Covariance Matrix Adaptation Evolution Strategy (CMA-ES) algorithm is used in combination with an adaptive penalty function. The main purpose for the work is to develop a tool that creates airfoils with best possible performance for low-speed application. However, the study is also performed to investigate the performance and limitations of the CST method, the adjusted version of XFOIL and the CMA-ES algorithm.

To develop the airfoil optimisation method the CST technique is tested and its ability to reproduce an existing airfoil shape is investigated. Next, the performance of the XFOIL code is discussed and important parameters controlling the prediction of lift at high angles of attack and the overall drag

are adjusted to improve the code's accuracy with regard to low-speed wind turbine airfoil flows. Then, two single-point optimisation studies are performed to better understand how the optimum lift-to-drag ratio is affected by increasing the number of degrees of freedom in the CST method and by altering the airfoil thickness. Finally, the optimisation tool is used to design airfoils for the outer part of a MW sized wind turbine rotor blade having 18, 21 and 25% thickness.

2. Method

In the following, the approach used to develop the airfoil design tool is presented. First, the CST parametrisation technique is introduced and the methods used to control geometric parameters on the airfoil are given. Then, the adjustments performed to the XFOIL code in order to improve the predictions from the flow solver are explained. Finally, the CMA-ES algorithm, and the adaptive penalty function are introduced, and the methods used to optimise the airfoils are given. In Figure 1, an overview of the design process is illustrated. Here, the optimisation algorithm finds the airfoil shape that maximises the performance, subject to both aerodynamic and geometric constraints.

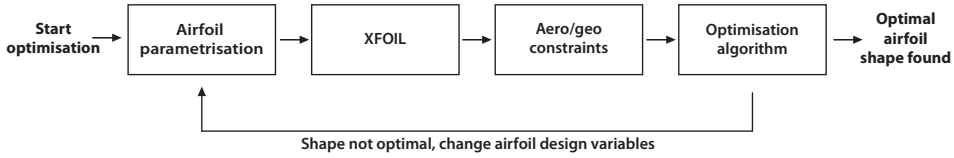

Figure 1: Airfoil optimisation loop.

2.1. CST airfoil parametrisation

The CST method is a parametrisation technique developed by Kulfan and Bussoletti at Boeing [7] to perform shape optimisation of complex aircraft configurations. The method combines an analytical class function with a parametric shape function to create smooth geometries using a low number of design variables. For airfoil application the method is described by

$$\zeta(\psi) = C(\psi)S(\psi) + \psi\zeta_T \ , \tag{1}$$

where $\zeta = y/c$ and $\psi = x/c$, are the non-dimensional stations and coordinates of the airfoil with respect to the chord, c. The last term controls

the thickness at the trailing edge, where $\zeta_T = y_{te}/c$. The class function is defined as

$$C(\psi) = \psi^{N1}(1-\psi)^{N2} \ , \tag{2}$$

and determines the family of shapes generated. To obtain the class function that represents airfoils, the exponentials $N1$ and $N2$ are set to 0.5 and 1.0, respectively. The airfoil shape is generated through the summation of Bernstein polynomials in the shape function

$$S(\psi) = \sum_{i=0}^{n} a_i b_{i,n}(\psi) \ , \tag{3}$$

where a is a vector of weights, and b is the Bernstein polynomial defined as

$$b_{i,n} = \binom{n}{i} \psi^i (1-\psi)^{n-i} \ . \tag{4}$$

By manipulating the weights a_i, in the shape function for the upper and lower surfaces of the airfoil, individual geometries are created, and the global smoothing abilities of the Bernstein polynomials ensure that any combination of weights leads to a smooth airfoil shape. By increasing the number of weights, more shape functions are introduced uniformly along the geometry and more complex airfoils can be created. The leading edge radius, the boat-tail angle and the trailing edge thickness are controlled directly through the first and the last weights of the shape function. Control of the airfoil thickness and camber is not addressed by the CST method and to provide control of these parameters the generated geometry is decomposed into a thickness and camber distribution. To create airfoils with a specific thickness, the a values in the CST method are scaled. The locations of maximum thickness and camber, on the other hand, are controlled by introducing geometric constrains in the optimisation process. To reproduce existing airfoils, the root mean square error between the coordinates of the seeded airfoil and the CST airfoil are minimised using a non-linear curve fitting algorithm.

2.2. XFOIL adjustments

XFOIL is an interactive program for the design and analysis of subsonic airfoils created by Drela and Youngren at Massachusetts Institute of Technology (MIT). The program combines a high-order panel method with a fully-coupled viscous/inviscid method, making the code well suited for rapid analysis of low Reynolds number airfoil flows with transitional separation

bubbles [8, 9]. The program has both Full-Inverse and Mixed-Inverse design capabilities, and is widely used in the aeronautical industry for the design of airfoils. At low speeds, however, comparisons between XFOIL and wind tunnel measurements show that the drag is often under predicted by the program, and that the maximum lift, in the region of the stall, is often over predicted [10, 11]. To reduce this error, the parameters controlling the high lift, post-stall and drag computations in XFOIL (version 6.99) are adjusted for low-speed wind turbine applications.

A guidance on how to improve the high lift and post-stall predictions is retrieved from a method used by Delft University (TU Delft) to develop their modified XFOIL (version 5.4), named RFOIL. In RFOIL, the accuracy of the maximum lift predictions is improved by adjusting the shear lag coefficients in Green's lag entrainment equation of the turbulent boundary layer model. The calibration is performed by adjusting the A and B coefficients in the $G - \beta$ locus

$$G = A\sqrt{1 + B\beta} \,, \tag{5}$$

which controls the equilibrium level of the shear stress of the turbulent boundary layer. In XFOIL the constants $A = 6.7$, and $B = 0.75$ are used for this locus, based on experimental data for equilibrium flows. However, since the $G - \beta$ locus affects the maximum lift predictions, Drela advises that the A and B coefficients are calibrated for specific airfoil flows. In RFOIL it is found that the high lift predictions for wind turbine airfoil flows are improved by changing the A and B coefficients to 6.75 and 0.83, respectively. To also improve the post-stall predictions, RFOIL uses an engineering expression that couples the deviations from the equilibrium flow to the shape factor. This expression is given by

$$K_c = 4.65 - 0.95 \tanh(0.275 H_k - 3.5) \,. \tag{6}$$

Here, K_c is the shear-lag coefficient, which controls how much the actual shear stress lags behind the equilibrium shear stress, and H_k is the shape factor. In XFOIL Drela uses a constant value for $K_c = 5.6$, while the coupling performed in RFOIL ensures that K_c takes the value 5.6 for attached flow (H_k below 3.0), and $K_c = 3.65$ for larger values of H_k, corresponding to separated turbulent flow [12]. The performance of the RFOIL code is well validated and comparison to measured data shows that the code consistently predicts the lift at stall and in the post-stall region more accurately than XFOIL [13, 11]. The drag computations, on the other hand, are not modified in RFOIL and to improve the drag predictions for low-speed application in this work, the turbulent skin friction coefficient is increased using

a multiplier. This multiplier, named CFAC, existed in older versions of the XFOIL code, and is re-implemented in the adjusted version.

The performance of the adjusted XFOIL code is investigated by comparing calculations of the DU96W180 airfoil at a Reynolds number of 3 million to experimental data from the low-speed wind tunnels at TU Delft and Stuttgart, and to calculations using the original XFOIL and the RFOIL code.

2.3. Airfoil design criteria

To maximise the power production of a wind turbine the fundamental design criterion for the airfoils at the outer part of the rotor blade is to produce high lift-to-drag ratios. Towards the root, where structural requirements dominate, thicker airfoils are needed and high lift capabilities become more important. What is to be considered an optimal airfoil along a rotor blade is, thus, a trade-off between aerodynamic and structural requirements. At ideal conditions, modern pitch controlled, variable speed wind turbines operate at a constant tip speed ratio over a wide range of wind speeds. This means that the airfoils can be designed to produce its best performance at a single angle of attack. However, to account for sudden shifts in wind speed due to atmospheric turbulence or from delay in the control system response, the airfoils should be designed so that the best performance occurs with a margin around the design point [14]. Also the difference in angle of attack, α, between the design point and the stall is important. To prevent excessive loads in case of a gust this difference should not be too large. If this angle difference is too small, however, a slow working control system could make the rotor stall [13]. Following this design philosophy, three airfoils having 18, 21 and 25% thickness are developed. The airfoils are intended to be used at the outer part of a MW wind turbine rotor blade operating at a Reynolds number of 3 million. The three dimensional flow effects due to rotation in this part of the rotor blade are assumed to be small, hence, the flow around each airfoil is considered two dimensional.

In Table 1, the most important constraints that represent design criteria for the three different airfoils are given. The 18% thick airfoil is intended to operate at the tip of the rotor blade and a thin trailing edge (TE) is used to minimise trailing edge self noise. The airfoils further inboard have thicker trailing edges for structural reasons. To limit aerodynamic torsional loads, a maximum allowable pitch moment, C_m, constraint is applied for the tip airfoil. The stall margin criterion is used to control the difference in angle of attack between the design point and the stall, and to reduce fatigue, the

margin to stall is increased slightly for the airfoils towards the tip of the rotor blade.

Table 1: Airfoil design criteria.

Design criteria			
Airfoil thickness	18%	21%	25%
Max thickness pos	36%	34%	32%
TE thickness	0.15%	0.25%	0.325%
Max C_m	-0.08	-	-
Stall margin	5°	5°	4°

2.4. Airfoil optimisation

The airfoil optimisation is performed by executing the adjusted XFOIL code twice for a range of angles of attack between -2 and 16 degrees in each objective function evaluation. The first run computes the clean airfoil performance using free transition, and the second run simulates the airfoil with leading edge contamination by fixing the transition on both sides of the airfoil at 10% of the chord from the leading edge. The flow condition on the airfoils is adjusted using the N_{crit} parameter in XFOIL. The N_{crit} value determines the amplification factor of the most-amplified frequency which triggers transition on the airfoils, and it is used to mimic the effect of the turbulence level in the flow on the transition process [8]. To represent the flow on the airfoils for the clean and turbulent simulations N_{crit} values of 9 and 0.1 are used, respectively. The airfoil performance is maximised by optimising the lift-to-drag ratio at clean condition for a prescribed range of angles of attack. The optimisation problem is defined as

$$\begin{aligned} &\text{maximise} \quad f(\boldsymbol{x}) = \sum_{i=1}^{n} \left(\frac{C_l}{C_d} \right)_i \\ &\text{subject to} \quad g_j(\boldsymbol{x}) \leq 0,\ j = 1, \ldots, m. \end{aligned}$$

Here, $\boldsymbol{x}$ is the vector containing the CST airfoil design variables, n is the number of angles of attack where the performance is to be maximised, and C_l and C_d are the corresponding lift and drag coefficients. In g_j, where $j = 1, ..., m$, the normalised constraints are included, which are based on the design criteria in Table 1. To symmetrically balance the shape of the lift-to-drag curve in the region of the optimum point, the computed performance in the angle of attack range $i = 1, ..., n$ are normalised with respect to the

maximum value. By increasing the size of this range, more angles of attack are included in the optimisation, resulting in a wider lift-to-drag curve.

The CMA-ES algorithm developed by Hansen [15] is used to solve the optimisation problem. This algorithm belongs to the family of evolution algorithms and is a powerful stochastic, derivative-free search method normally used to solve unconstrained, non-linear, black-box optimisation problems. CMA-ES is known to manage a rugged search landscape with noise and local optima well, which is considered an important quality for solving the constrained airfoil problem. The algorithm does not require parameter tuning, and only the population size and the stopping criteria are adjusted to match the problem. The population size is increased by multiplying the number of degrees of freedom used in the CST method with a factor. The optimisation is started from an initial airfoil shape, and to limit the size of the design space, upper and lower bounds on $\boldsymbol{x}$ are applied. The algorithm is stopped, and an optimal solution is chosen to be found when a change in $\boldsymbol{x}$ is smaller than $1 \cdot 10^{-3}$.

To ensure that the different design criteria are respected by the optimisation, constraints are applied. However, since little research has been done on investigating constraint handling techniques for evolutionary algorithms, no universal method exists. In this work, the airfoil problem is constrained using an adaptive penalty function inspired by [16]. The penalty function replaces the original optimisation problem, and is defined as

$$f_p(\boldsymbol{x}) = f(\boldsymbol{x}) \; + \; \sum_{j=1}^{m} (\lambda_{j,k} d_j) \; . \tag{7}$$

Here, $f(\boldsymbol{x})$ is the original objective function value, λ contains the penalties for each constraint, and d is the normalised instantaneous constraint violation. To make the penalty function adaptive, λ is allowed to increase and decrease in size in each iteration k, according to the severity of the violation. The response of this system is controlled by

$$\lambda_{j,k+1} = \begin{cases} \lambda_{j,k} + \beta_1 \tilde{d}_j, & \text{if } \tilde{d} > 0 \\ \lambda_{j,k} - \beta_2 \tilde{d}_j, & \text{if } \tilde{d} < 0 \\ \lambda_{j,k} & \text{if } \tilde{d} = 0 \end{cases} , \tag{8}$$

where, β_1 and β_2 are constants that determine the rate of change in λ, and $\tilde{d}$ is the constraint violation for the best objective function found in the last iteration. To avoid negative values and to ensure that the penalties are activated quickly throughout the search, the minimum size of λ is bounded.

Eight constraints, including those in Table 1, are used to control the optimisation. At clean condition, constraints are used to limit the moment coefficient, the difference in angle of attack between the optimum point and the stall, the maximum location of the airfoil thickness, and the slope of the lift curve in the pre- and post-stall region. Since the chord and twist distributions on a rotor blade are specifically designed to match the local airfoil lift and angle of attack, it is considered important to minimise the changes in these values caused by leading edge contamination. Constraints are therefore also applied to control the allowable differences in performance for the airfoils at clean and turbulent flow condition. Hence, the acceptable loss in lift and difference in angle of attack for the design point are constrained. For the design points, a difference in angle of attack of ± 0.5 degrees is accepted between clean and turbulent flow. In addition, the minimum allowable lift-to-drag ratio at turbulent flow condition is constrained.

The performance of the airfoil design method is first investigated by performing two single-point optimisation studies. Here, the effect of changing the number of design variables in the CST method and changing the airfoil thickness are studied by optimising airfoils at $C_l = 1$. Then, the method is used to optimise airfoils at a Reynolds number of 3 million, having 18, 21 and 25% thickness.

3. Results

In the following, the results from the studies performed to develop the airfoil design tool are presented. First, the ability of the CST method to reproduce an existing airfoil geometry is tested. Then the effect of adjusting the parameters influencing the lift and drag predictions in XFOIL are compared to calculations obtained using the default XFOIL code, the RFOIL code and experimental data. Finally, the results of the single-point optimisation studies and the optimised 18, 21 and 25% thick airfoils are given.

3.1. CST parametrisation study

For the optimisation process the number of design variables required to reproduce a representative airfoil is an important quantity, since both the possible design space of airfoil shapes and the computational time scales with the number of degrees of freedom (DOF). In Figure 2, the Delft DU93W210 airfoil is seeded by minimising the root mean square (r.m.s) error between the coordinates of the Delft airfoil and the CST airfoil. Figure 2a shows the CST airfoil fit to the Delft airfoil using 6 degrees of freedom on both

pressure and suction side. In Figure 2b, the r.m.s. error when increasing the degrees of freedom in the CST method from 1 to 10 is given. As can be seen, the ability to reproduce the geometry is not improved much by applying more than 6 design variables, neither for the suction nor for the pressure side on this airfoil. However, to exactly reproduce the aerodynamic force coefficients it is observed that more design variables are required.

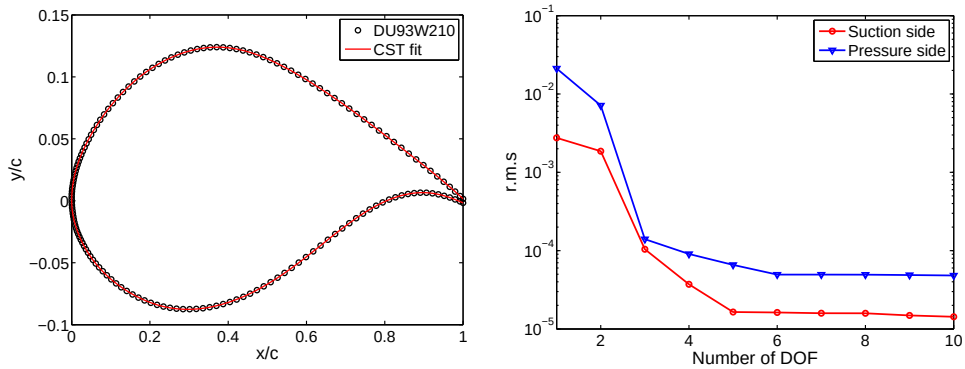

(a) (b)

Figure 2: CST airfoil study.

3.2. Adjusted XFOIL

The effects of adjusting the parameters that control the prediction of lift and drag in the XFOIL code are investigated using the DU96W180 airfoil, at a Reynolds number of 3 million as a test case. In Figure 3, the lift coefficients from the adjusted XFOIL code are compared to the default XFOIL code, RFOIL and to experimental data from the Stuttgart wind tunnel. In Figure 3a, it can be seen that the default XFOIL code does not capture the stall and over-predicts the lift at high angles of attack compared to the experimental data. The RFOIL code, on the other hand, captures the stall well, and only over-predicts the lift slightly. By changing the A and B parameters for the $G - \beta$ locus in XFOIL, the over-predicted lift is reduced, but the stall is still not captured. However, by also including the term that couples the deviation of the equilibrium flow to the shape factor, a much better prediction of the stall is obtained. To obtain the depicted result however, the coupling expression is slightly modified compared to the RFOIL definition. In the modified expression, K_c is activated earlier, and is also allowed to decrease to lower values than in RFOIL. In Figure 3b, the computed drag is compared to experimental data and the adjustments

performed to the lift in XFOIL do not change the drag. Hence, results comparable to the default XFOIL code and RFOIL are obtained.

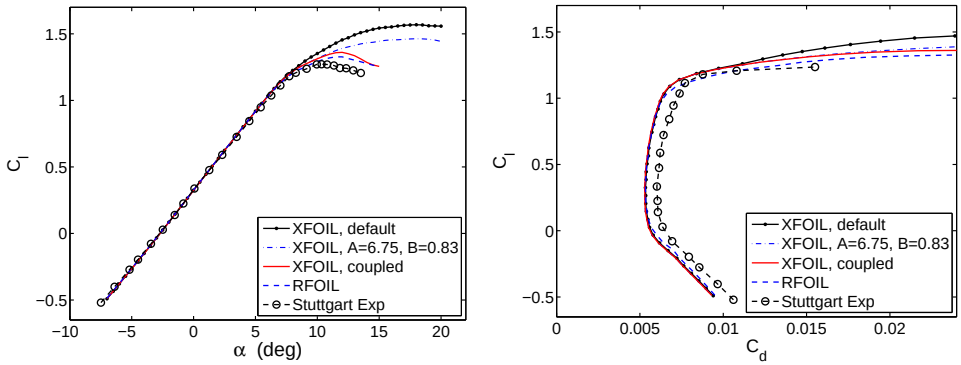

(a) (b)

Figure 3: Effect of adjusting $G - \beta$ locus and coupling term.

In Figure 4, the drag in XFOIL is adjusted by increasing the turbulent skin friction coefficient using a CFAC multiplier of 1.3. As can be seen in Figure 4a, applying this multiplier improves the drag predictions for almost all values of C_l, compared to the experimental data. However, by increasing the turbulent skin friction coefficient also the lift is decreased, and to recover the lift, the A and B parameters are reduced to 6.7 and 0.77, respectively. In Figure 4b, the final lift predictions are visualised. Here, the lift coefficients from the adjusted XFOIL code resemble the RFOIL results well.

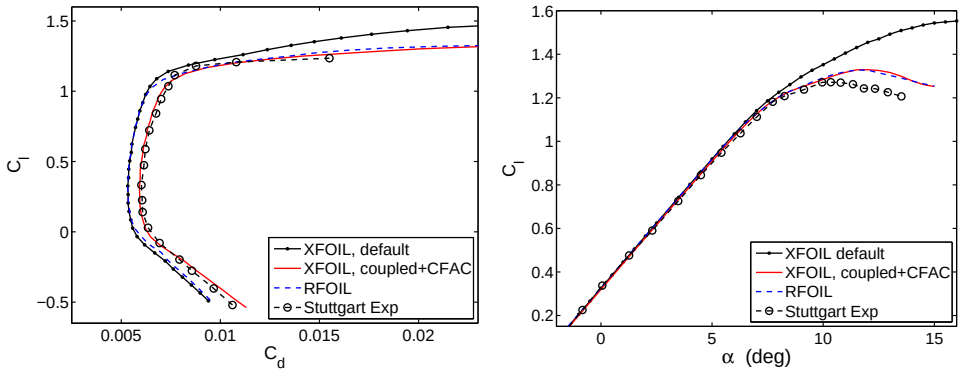

(a) (b)

Figure 4: Effect of including CFAC multiplier.

In Figure 5, computations using the adjusted XFOIL code are compared to experimental data from the low-speed wind tunnel at TU Delft. In these experiments, the loss of performance due to leading edge transition is studied by performing experiments also with turbulators mounted at 5% from the leading edge of the airfoil. Figure 5a shows the increase in drag due to applying the turbulators and it can be seen that the adjusted XFOIL predictions match the experimental data fairly well. However, to obtain the depicted result, a 20% reduction of the computed drag is required. When analysing airfoil performance using the default XFOIL or RFOIL code it is a normal practice to increase the free transition drag by about 9-10 %, to better match wind tunnel data, [11]. The increased turbulent skin friction introduced to XFOIL in this work, thus, changes this requirement and calibration of the predicted drag with turbulators is now required.

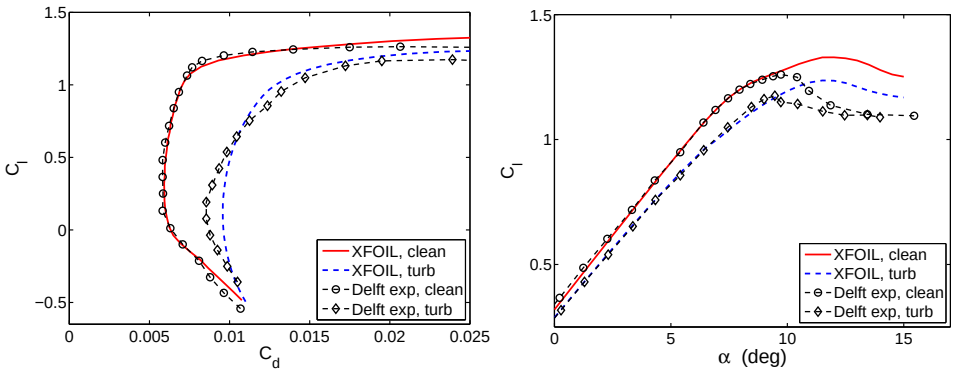

(a) (b)

Figure 5: Leading edge contamination.

In Figure 5b, the lift coefficient for the airfoil both with and without turbulators are shown. Here, it can be seen that the adjusted XFOIL code is able to predict the loss in lift due to leading edge transition well. Interestingly, the un-turbulated experiments from the Delft low-speed wind tunnel both predict a slightly lower drag and a more abrupt stall for the DU96W180 airfoil compared to the Stuttgart wind tunnel data seen in Figure 3 and 4.

3.3. Design space

The design space searched by the optimisation is constrained using bounds. The upper bounds are the maximum values for the weights in the CST method, while the lower bounds are adjusted to ensure that only airfoils with reasonable trailing edge thickness and leading edge radius are investigated.

In Figure 6, the starting airfoil, and the upper and lower bounds are shown. By increasing the number of degrees of freedom in the CST method the design space of possible airfoil shapes is also increased. To test the ability of CMA-ES to find the best global solution the optimisation is started from the middle of the design space using a symmetrical airfoil shape.

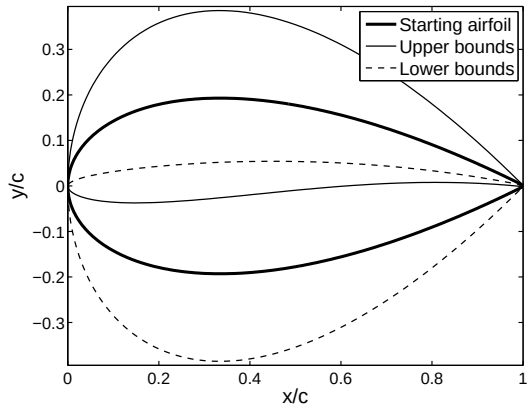

Figure 6: Starting airfoil and bounds.

3.4. Single-point airfoil optimisation

In Figure 7, the results from the two unconstrained single-point optimisation studies are given. The first study finds the 18 % thick airfoil shapes that maximise the lift-to-drag ratio for increased number of degrees of freedom in the CST method. The second study optimises the performance of the airfoils at increased thickness. Both studies are performed at $C_l = 1$, and the airfoils are optimised first for clean, and then for turbulent flow conditions. In Figure 7a, the results from the first study are shown. Here, it is seen that a large difference in performance exists between the two flow scenarios. The best lift-to-drag ratio is obtained using more than 12 CST design variables on both suction and pressure side of the airfoil, and at clean condition the best performance is about 235. In turbulent flow, the C_l/C_d ratio with the same number of degrees of freedom is reduced to 88. It is observed that the improved performance at clean conditions from using more design variables is linked to the ability of the optimisation algorithm to refine the region behind the thickest point on the suction side of the airfoil. By increasing the number of degrees of freedom, a more defined bubble ramp is created in this region, which increases the amount of laminar flow, and minimises the effect of the transitional separation bubble. The results indicate that a large

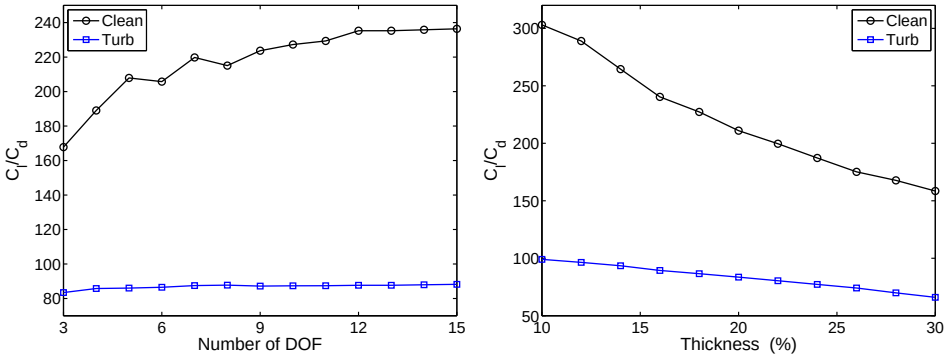

(a) (b)

Figure 7: CST degree of freedom and thickness study.

number of design variables should be used to obtain the best performance. However, as the shape functions in the CST method are distributed uniformly along the airfoil, flexibility is also introduced uniformly. If the aifoil surface is too flexible, the optimisation algorithm often discovers slightly improved solutions by creating bumps and local refinements also at undesirable locations on the airfoil. This problem is well described by Drela in [17]. Hence, to obtain feasible solutions with best possible performance, the degrees of freedom in the CST method must be chosen with care. At turbulent flow conditions, the lift-to-drag ratio is not improved much by increasing the number of design variables, since no laminar flow exists on the airfoils. In Figure 7b, the airfoils are optimised to maximise the performance at increasing thickness. Here, 9 and 6 CST design variables are used on the suction and pressure side of the airfoil, respectively. As expected, the lift-to-drag ratio at clean condition is linked to the thickness of the airfoil since the pressure drag is reduced for the thinner airfoils. The best and worst performance is found for the thinnest and thickest airfoils, and a C_l/C_d ratio of about 303 and 159 is obtained. Also in turbulent flow, the increase in performance from reducing the airfoil thickness exists. However, due to the absence of laminar flow, the performance is lower and a best C_l/C_d ratio of about 99 and 66 is computed for the thinnest and thickest airfoil, respectively.

3.5. Airfoil optimisation study

The developed airfoil design tool is tested for the optimisation of airfoils for a MW class wind turbine rotor blade having 18, 21 and 25% thickness. The performance of the optimised designs is compared to wind turbine air-

foils with the same thickness developed at TU Delft [13]. To control the minimum allowable C_l/C_d at turbulent flow the performance at the design condition is constrained to similar values as for the Delft airfoils. In Figure 8a, the optimised 18% thick airfoil is shown. The best airfoil found by the optimisation has a maximum camber of 3.15% and the thickest point occurs at $x/c = 0.346$. In Figure 8b, the best lift-to-drag ratio at clean and

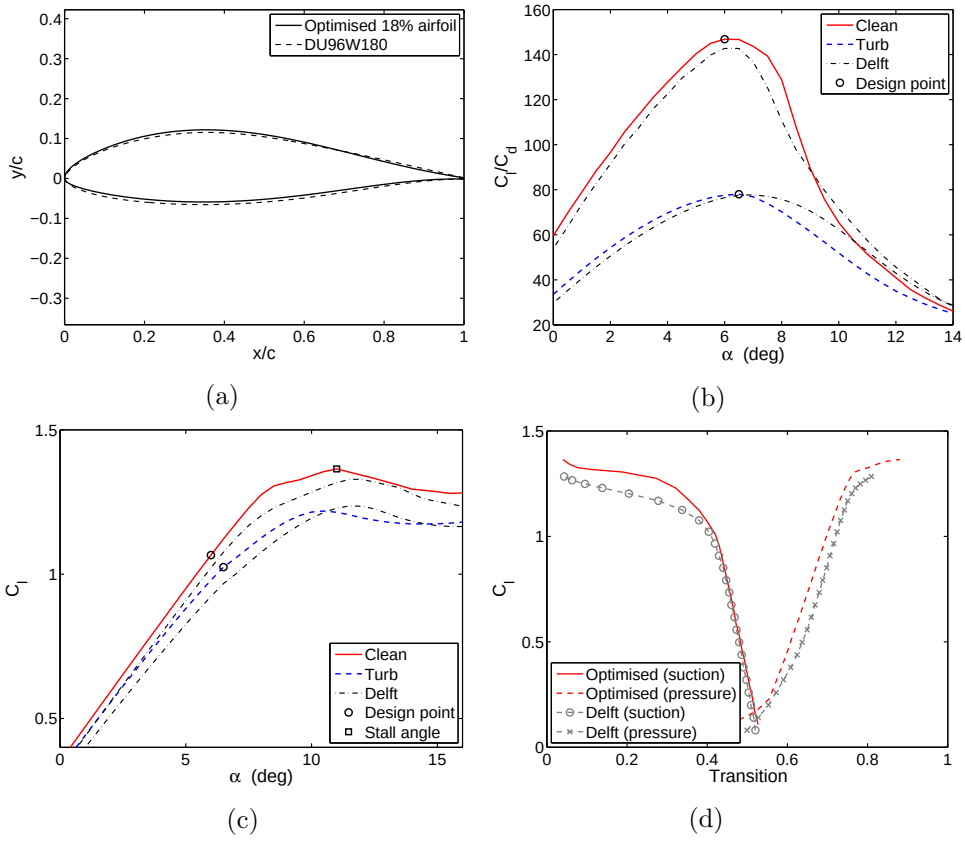

Figure 8: Optimised 18% airfoil results.

turbulent conditions for the optimised airfoil are compared to the predicted results of the DU96W180 airfoil. Here, it is seen that the new airfoil has better performance at clean condition than the Delft airfoil. The best C_l/C_d ratio for the optimised airfoil is about 147, while the computed lift-to-drag ratio for the Delft airfoil is 143. In turbulent flow the performance of the two airfoils is more similar and a best C_l/C_d ratio of about 77 is computed. The Delft airfoil, however, produces better performance at angles of attack higher than the design point. The lower performance of the optimised airfoil

in this region is believed to be due to the requirement to produce the best performance at about the same angle of attack at both flow conditions. The width of the clean performance C_l/C_d curve for the new airfoil is optimised for a range in angle of attack of 4 degrees. The resulting larger area between the clean and turbulent curves, representing increasing leading edge contamination, is expected to make it easier for the control system to cope with atmospheric turbulence.

In Figure 8c, the optimised design has a slightly higher lift coefficient at the design point than the Delft airfoil. A maximum loss in lift constraint due to leading edge transition less than $C_l = 0.15$ is used for the optimised design, and it can be seen that the loss for the Delft airfoil is about the same. At angles of attack above the design point a flat plateau exists in the lift curve at clean condition for the optimised airfoil. It is observed during the optimisation that the algorithm constantly attempts to maximise performance within the limits of the constraints by maximising the lift in the region around the design point. This plateau can also be seen in the lift curve of the Delft airfoil. In Figure 8d, the location of transition for the two airfoils is shown. Here, the optimised airfoil has slightly more laminar flow on the suction side compared to the Delft airfoil. At the pressure side on the other hand, the transition on the optimised airfoil occurs further forward than on the Delft airfoil.

In Figure 9a and 9b, the optimised 21% thick airfoil and its lift-to-drag polar at clean and turbulent conditions are given. This airfoil has a maximum camber of 2.87% and the maximum thickness point occurs at $x/c = 0.33$. Compared to the equivalent thick DU93W210 airfoil, the optimised airfoil has a similar maximum C_l/C_d of 141 compared to 139.5 at clean condition. At turbulent condition, the results are even closer, and a lift-to-drag ratio of 69 is computed for both airfoils at the design point.

In Figure 9c, the lift curves for the optimised airfoil and the Delft airfoil are compared. Here, the plateau in the lift slope at clean condition, that also was observed for the 18% airfoil, can be recognised. The transition for both airfoils are almost identical up to the design point, as can be seen in Figure 9d. At higher lift coefficients the transition for the Delft airfoil is less abrupt than for the optimised design.

In Figure 10a and 10b, the optimised 25% airfoil and the predicted lift-to-drag is compared to the equivalent thick DU91W2-250 airfoil. The optimised airfoil has a maximum camber of 3.2% and the location of the maximum thickness point occurs at $x/c = 0.31$. At clean condition a maximum C_l/C_d ratio of about 130 and 132 is computed for the optimised and the Delft airfoil, respectively. However, also at this thickness the lift-to-drag

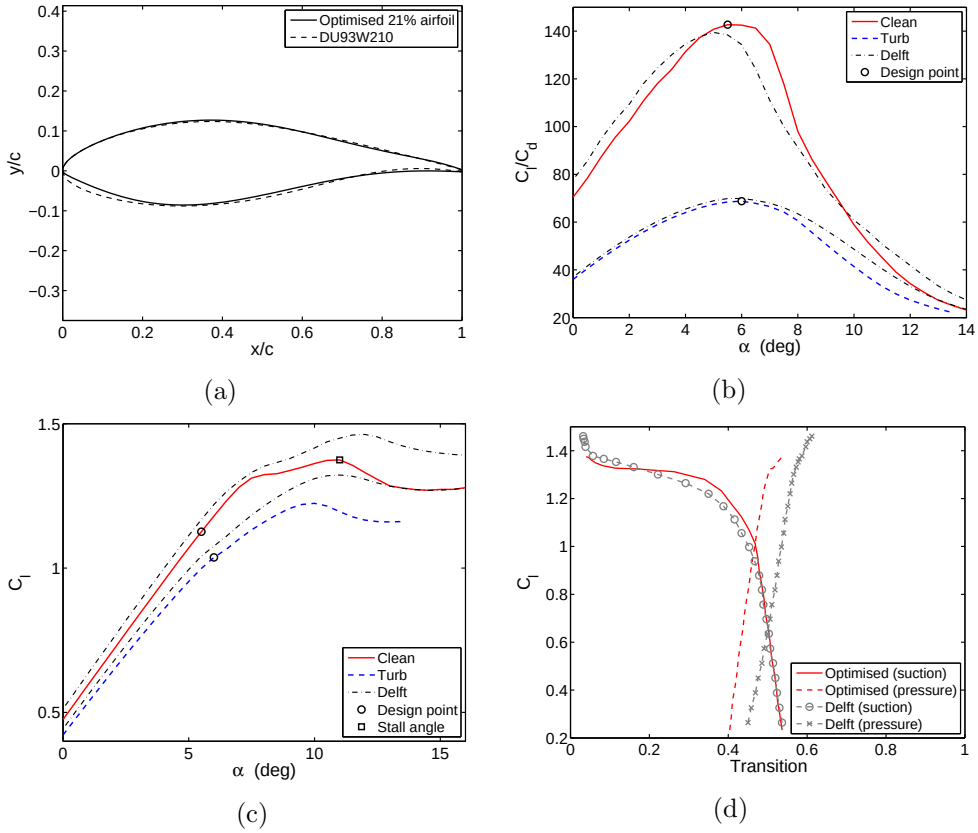

Figure 9: Optimised 21% airfoil results.

polar for the optimised airfoil is wider in the region of the design point. At turbulent condition the performance is closely matched, and a best C_l/C_d of about 62 is predicted. In Figure 10c and 10d, the lift coefficients and the transition for the optimised airfoil are shown. Here, the lift coefficients at the design point for the optimised airfoil are about the same as for the Delft airfoil at the two simulated flow conditions. The stall on the optimised airfoil, however, is not as smooth as on the Delft airfoil. The result both indicates that the Delft airfoil is well designed and that a more strict constraint should be used to optimise the airfoil at this thickness. The location of transition shows slightly more laminar flow on the suction side than on the pressure side for the optimised airfoil compared to the Delft design.

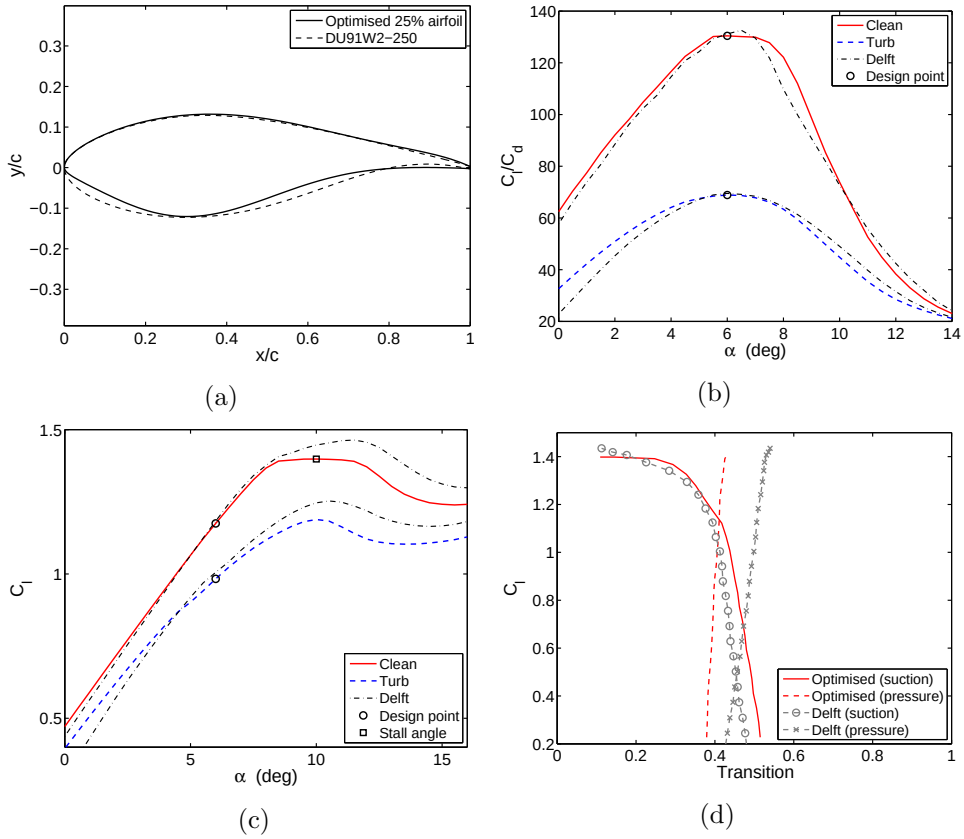

Figure 10: Optimised 25% airfoil results.

3.6. Parameter tuning

The results produced by the airfoil design method strongly depend on the parameters applied to the different problems. Both the number of constraints, the population size in CMA-ES, the number of degrees of freedom in the CST method and the penalty function coefficients influence the solution. In Figure 11, the residual of the objective value for the optimised 18% airfoil is shown. Here, the CMA-ES algorithm is seen to converge on the best performing airfoil shape after 364 iterations. To obtain the presented result a rather large population size of 60 is required, corresponding to 21840 function calls and 43680 XFOIL executions. To control the response of the adaptive penalty function the β_1 and β_2 values are set to about 1% and 0.7% of the final objective value. However, since the final objective value is not know upfront, a series of runs are required to adjust the coefficients.

It is found necessary to use an adaptive penalty function due to the large number of constraints. When applying a static penalty function, the size of the penalty is difficult to decide. If too large static penalties are used, the airfoil shape gets stuck, and the optimal solution is not obtained. If too soft penalties are applied, however, the constraints are broken and the algorithm searches in the direction of largest lift. Then, an airfoil with a Stratford-type pressure distribution is often developed. This airfoil type is known to give high lift but will also generate rather high drag and extensive separation in case of severe leading edge contamination [18].

The degrees of freedom used in the CST method and the range in angles of attack optimised, both influence the response of the computed coefficients. Their overlapping impact makes it difficult to apply the best settings. The 18 and 21% airfoils in this work are created using 6 and 4 degrees of freedom in the CST method on the suction and pressure side, respectively. The larger curvature of the 25% airfoil is designed using 6 and 8 design variables on the top and bottom surface. The range in angles of attack optimised for the 18% thick airfoil is 4 degrees, while the 21 and 25% airfoils is designed using 3 degrees.

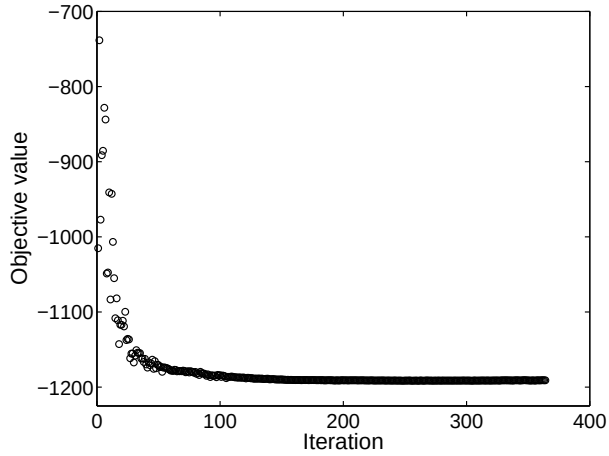

Figure 11: Objective value per iteration.

3.7. Conclusion

In this study, an airfoil optimisation method for wind turbine applications that controls the loss in performance due to leading edge contamination is developed. The class-shape transformation technique (CST) is used to parametrise the airfoil shape, and the aerodynamic performance is computed using an adjusted version of the panel code XFOIL. To optimise the airfoil, the derivative-free Covariance Matrix Adaptation Evolution Strategy (CMA-ES) algorithm is used in combination with an adaptive penalty function. The method is tested for the design of airfoils for the outer part of a MW sized wind turbine rotor blade having 18, 21 and 25% thickness. To control the loss in performance due to leading edge contamination, the allowable loss in lift coefficient and the difference in angle of attack at best performance between the clean and turbulent simulations are constrained. In addition, the minimum lift-to-drag ratio in turbulent flow condition is controlled. The optimised designs are compared to wind turbine airfoils created at TU Delft.

It is found that the developed method is able to create airfoils that have equal or improved performance compared to the Delft designs. The CST method is shown to be a flexible parametrisation technique and a large design space of smooth airfoil shapes is created using low degrees of freedom. It is believed, however, that the CST method would benefit from a local refinement scheme as a large number of design variables is required to maximise the airfoil performance at clean conditions. The CMA-ES algorithm is found to be a powerful, but time consuming search method, as a large population size is required to solve the constrained airfoil problem. However, the algorithm copes well with local optima and noise, and it is believed that the best solution within the limits of the CST method and the applied constraints is found. The adaptive penalty function used to constrain the optimisation problem matches the CMA-ES algorithm well and feasible solutions are often obtained at the limits of the constraints. However, the coefficients that control the response of the penalty function influence the solution and many runs are required to obtain the values used for the different problems. The adjustments performed to the flow solver XFOIL are shown to improve the predicted lift at high angles of attack, the post stall and the drag for the studied low-speed wind turbine application.

The large amount of possible, local solutions make the constrained airfoil problem difficult to solve. By increasing the number of degrees of freedom in the CST method and the number of constraints, the problem complexity is increased further. A disadvantage of the developed airfoil optimisation

method is that the best combination of CST design variables, penalty coefficients and range in optimised angles of attack is difficult to predict. Future studies should investigate the influence of these parameters in more detail, or test different constraint handling methods and parametrisation techniques in order to reduce the parameter tuning. The adjustments performed to the XFOIL code should be validated for a larger range of Reynolds numbers and be applied to other low-speed applications.

4. Acknowledgments

This project is financially supported by the Research Council of Norway and CMR Prototech. The author also wishes to thank Professor Per-Åge Krogstad and Professor Lars Sætran at the Department of Energy and Process Engineering at the Norwegian University of Science and Technology (NTNU) for supervising this work. Also, thanks to Professor Anton Evgrafov from the Department of Mathematical Sciences at NTNU for valuable input. Finally, thanks to Senior Researcher Anders Hallanger at Christian Michelsen Research (CMR), Ing. Bernt H. Hembre at Clampon and Dr. Gloria Stenfelt at the Marine Department of Bergen University College for their support when performing this study.

References

[1] R. S. Ehrmann, E. B. White, et al. Realistic leading-edge roughness effects on airfoil performance. In *31st AIAA Applied Aerodynamics Conference*, San Diego, CA USA, June 24–27 2013. AIAA 2013-2800.

[2] A. Sareen, C. A. Sapre, and M. S. Selig. Effects of leading edge erosion on wind turbine blade performance. *Wind Energy*, 17:1531–1542, 2014. doi: 10.1002/we.1649.

[3] J. L. Tangler and D. M. Somers. Status of the Special-Purpose airfoil families. Technical Report TP-3264, SERI, 1987.

[4] M. S. Selig and M. D. Maughmer. Generalized multipoint inverse airfoil design. *AIAA Journal*, 30(11):2618–2625, 1992.

[5] K. Kubrynski. Design of a flapped laminar airfoil for high performance sailplane. In *30th AIAA Applied Aerodynamics Conference*, New Orleans, Louisiana USA, June 25–28 2012. AIAA 2012-2662.

[6] K. S. Dahl and P. Fuglsang. Design of the wind turbine airfoil family Risø-A-XX. Technical Report Risø R-1024(EN), Risø National Laboratory, Roskilde, Denmark, December 1998.

[7] B. M. Kulfan and J. E. Bussoletti. Fundamental parametric geometry representation for aircraft component shapes. In *11th AIAA/ISSMO Multidisciplinary Analysis and Optimization Conference*, Portsmouth, VA USA, September 6–8 2006. AIAA 2006-6948.

[8] M. Drela and H. Youngren. XFOIL 6.9 User Primer, April 2014. http://web.mit.edu/drela/Public/web/xfoil/.

[9] M. Drela. *XFOIL: An Analysis and Design System for Low Reynolds Number Airfoils. Low Reynolds Number Aerodynamics.* Springer-Verlag, 1989. Lecture notes in Eng. 54.

[10] M. D. Maughmer and J. G. Coder. Comparisons of theoretical methods for predicting airfoil aerodynamic characteristics. Technical Report TR 10-D-106, RDECOM, August 2010.

[11] W. A. Timmer. An overview of NACA 6-digit airfoil series characteristics with reference to airfoils for large wind turbine blades. In *47th AIAA Aerospace Sciences Meeting Including The New Horizons Forum and Aerospace Exposition*, Orlando, FL USA, January 5–8 2009. AIAA 2009-268.

[12] R.P.J.O.M. van Rooij. Modification of the boundary layer calculation in RFOIL for improved airfoil stall predicition, September 1996. Report IW-96087R.

[13] W. A. Timmer and R.P.J.O.M. van Rooij. Summary of the Delft University wind turbine dedicated airfoils. *Journal of Solar Energy Engineering*, 125(4):488–496, 2003. doi:10.1115/1.1626129.

[14] M. S. Selig. *Low Reynolds Number Airfoil Design.* Lecture notes von Karman Institute, published by von Karman Institute for Fluid Dynamics or NATO–RTO/AVT, 2003.

[15] N. Hansen. *The CMA Evolution Strategy: A Tutorial.* Research Centre Saclay-Île-de-France, Université Paris-Saclay, April 2016.

[16] A. E. Smith and D. W. Coit. *Constraint-Handling Techniques - Penalty Functions.* Chapter C5.2. in Handbook of Evolutionary Computation, Institute of Physics Publishing and Oxford University Press, Bristol, U.K., 1997.

[17] M. Drela. *Pros and Cons of Airfoil Optimization.* Chapter in Frontiers of Computational Fluid Dynamics edited by D. A. Caughey and M. M. Hafez, Singapore, 1998.

[18] W. A. Timmer and R.P.J.O.M. van Rooy. Thick airfoils for HAWTs. *Journal of Wind Engineering and Industrial Aerodynamics*, 39:151–160, 1992.

Paper C

Winglet Optimisation for a Model-Scale Wind Turbine

T. H. Hansen[1] and F. Mühle[2]
[1] Norwegian University of Science and Technology, NTNU Trondheim, Norway and CMR Prototech, Bergen, Norway

[2] Norwegian University of Life Science, NMBU Ås, Norway

Abstract

A winglet optimisation method is developed, and tested for a model-scale wind turbine. The best performing winglet shape is obtained by constructing a Kriging surrogate model which is refined using an infill criterion based on expected improvement. The turbine performance is simulated by solving the incompressible Navier-Stokes equations and the turbulent flow is predicted using the Spalart Allmaras turbulence model. To validate the simulated performance, experiments are performed in the NTNU wind tunnel. According to the simulations, the optimised winglet increases the turbine power and thrust by 7.8% and 6.3%. The wind tunnel experiments show that the turbine power and thrust increases by 8.9% and 7.4%. When introducing more turbulence in the wind tunnel to reduce laminar separation, the turbine power and thrust due to the winglet increases by 10.3% and 14.9%.

1. Introduction

To improve the performance, most modern transport and glider aircraft are built with winglets. When correctly designed, winglets create a flow-field that reduces the amount of span-wise flow in the tip region of the wing, and increases the wing's efficiency without increasing the span. For modern transport aircraft, winglets are known to reduce the block fuel consumption by 4-5%, and also moderate the noise levels at take-off [1]. On span regulated gliders, the increase in performance due to winglets often surpasses the percentage score difference between the top 6 positions in a cross-country competition [2]. Since the wind industry traditionally has been less concerned with span limitations, wind turbines do not normally use winglets. However, if future turbines are to be located in urban areas, or to reduce

the size of floating structures, rotor span might become an important factor. This is recognised by the research community where winglets for wind turbines are given more attention. Since the flow in the tip region of the rotor blades is linked to the wake, winglets are often designed numerically using vortex lattice methods (VLM) with free wake, or with free-wake lifting line algorithms (FWLL). In [3] a winglet for a model-scale turbine is designed using a free-wake VLM code by varying the winglet shape using parameter studies. VLM calculations predict an increase in turbine power of more than 10%, and when the winglet is tested experimentally the test results showed a peak gain of 9.1%, however, this only occurs in a narrow range of conditions. In a wider applicable range, the best increase in power is about 4%. A winglet for a MW-class wind turbine is designed in [4] by optimising the circulation on the rotor using a FWLL method and a gradient algorithm. According to the FWLL calculations, the winglet increases the turbine power by 2.5%. When the winglet is analysed using the more realistic Computational Fluid Dynamics (CFD) code EllipSys3D, the increase in turbine power is reduced to 1.7%. The studies show that functional winglets for wind turbines can be designed using computational inexpensive numerical tools and simple design methods. However, in order to study the possible benefits of using winglets on wind turbines in more detail, numerical tools that predict the flow physics better and optimisation techniques that search for the global best solution should be used to design the winglet.

In this work, a winglet optimisation method for wind turbine application is developed. The tool is tested for a model-scale wind turbine. The best performing winglet shape is found by constructing a Kriging surrogate model, which is refined using an infill criterion based on expected improvement. The turbine performance is simulated by solving the incompressible Reynolds-Averaged-Navier-Stokes (RANS) equations. For the winglet optimisation, the turbulent flow is predicted using the Spalart Allmaras turbulence model, while an Elliptic Blending Reynolds-Stress model is used to analyse the design. To validate the simulated rotor performance, experiments are performed in the NTNU wind tunnel. The main purpose for the work is to develop a tool that automatically designs the best possible winglet shape when solving the computational expensive RANS equations. The work is also performed to design a test turbine for future winglet studies, and to investigate the performance and limitations of the Kriging surrogate model. To develop the wind tunnel test turbine, a new model-scale rotor geometry and new airfoils for the rotor blade and winglet are created.

2. Method

In the following, the approach used to develop the winglet optimisation tool is explained. First, the methods used to design the model-scale rotor blade and airfoils are given. Then, the surrogate model is introduced and the reasons for applying a Kriging model in combination with the expected improvement infill criterion are discussed. Finally, the CFD simulations and wind tunnel experiments are presented. In Figure 1, the optimisation method is illustrated. As can be seen, the best performing winglet shape is found by constructing and refining a Kriging surrogate model in a two stage approach. To create the initial samples, a Design of Experiment (DoE) is created using a Latin Hypercube (LHC) sampling plan. The infill points that maximise the expected improvement are obtained by optimising the Kriging model using a hybrid genetic-gradient algorithm.

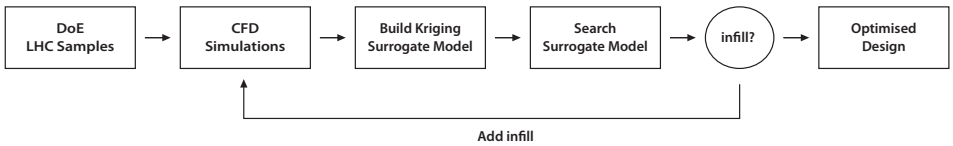

Figure 1: Winglet optimisation loop.

2.1. Rotor blade design

The rotor blade is designed by computing the chord and twist distributions according to Blade Element Momentum (BEM) theory. In this classical model the rotor blade with the best aerodynamic efficiency is obtained by optimising the rotor's axial induction factor at different stream tubes according to

$$16\ a^3 - 24\ a^2 + a(9 - 3x^2) - 1 + x^2 = 0\ . \tag{1}$$

Here, a is the axial induction and $x = \omega r / U_\infty$ is the local rotational speed at a radius r, non-dimensionalised with respect to the wind speed, U_∞. The corresponding tangential induction factor is given by

$$a' = \frac{1 - 3a}{4a - 1}\ , \tag{2}$$

and the optimal local flow angle is found from

$$\tan(\phi) = \frac{(1 - a)}{(1 + a')x}\ . \tag{3}$$

The twist distribution on the rotor blade is computed using

$$\theta = \phi - \alpha_{opt} \ , \tag{4}$$

where, α_{opt} is the airfoil angle of attack for best lift-to-drag ratio. The span-wise chord distribution is calculated according to

$$c = \frac{8\pi \ a \ x \ \sin^2(\theta) R}{(1-a) B C_n \lambda} \ , \tag{5}$$

where, R is the radius of the rotor, B is the number of blades, and λ is the tip speed ratio (TSR),

$$\lambda = \frac{\omega R}{U_\infty} \ . \tag{6}$$

The normal force coefficient is given by

$$C_n = C_{l,opt} \cos(\theta) + C_{d,opt} \sin(\theta) \ , \tag{7}$$

and is calculated using the lift and drag coefficients for the airfoil operating at its best lift-to-drag ratio [5].

Due to the model-scale flow condition on the winglet and the size of the wind tunnel, both the Reynolds number at the rotor tip and the blockage in the wind tunnel are important. The Reynolds number is given by

$$Re = \frac{\lambda U_\infty c}{\nu} \ , \tag{8}$$

where ν is the kinematic viscosity of air. At low Reynolds numbers it is well known that the dominating viscous forces limit the aerodynamic performance. By increasing the rotor radius, the Reynolds number is increased, however, so is the blockage in the wind tunnel. In an effort to balance these two conflicting physical properties, a 2-bladed rotor with a radius $R = 0.45$ m and a design TSR of 5 is chosen. This rotor favours the flow conditions on the rotor tip and has a wind tunnel blockage ratio of about 13%. To check the performance of the 2-bladed rotor, the measured power and thrust is compared to an existing 3-bladed NTNU model turbine with equal rotor radius [6].

2.2. Airfoil design

To match the flow condition on the model-scale turbine and winglet, new airfoils are created using an optimisation method developed in earlier work [7]. Here, the Class-Shape-Transformation (CST) technique [8] is applied

to parametrise the airfoil shape, and the aerodynamic performance is computed using an adjusted version of the panel code XFOIL [9]. Further, the derivative-free Covariance Matrix Adaptation Evolution Strategy (CMA-ES) algorithm [10] is employed to find the best performing airfoil shape. The optimisation is performed by executing the XFOIL code for a range of angles of attack in each objective function evaluation. To maximise the airfoil performance, the lift-to-drag ratio for the simulated range of angles of attack is optimised. The optimisation problem is defined as

$$\begin{aligned} &\text{maximise} \quad f(\boldsymbol{x}) = \sum_{i=1}^{n} \left(\frac{C_l}{C_d} \right)_i \\ &\text{subject to} \quad b_{l,j} \leq \boldsymbol{x} \leq b_{u,j}, \; j = 1, \ldots, m \end{aligned}$$

where, $\boldsymbol{x}$ is a vector with range $j = 1, .., m$ containing the CST airfoil design variables, n is the number of angles of attack where the performance is to be maximised, and C_l and C_d are the corresponding lift and drag coefficients. To symmetrically balance the shape of the lift-to-drag curve in the region of the optimum point, the computed performance in the angle of attack range $i = 1, ..., n$ is normalised with respect to the maximum value. To ensure sufficient structural stiffness for the wind tunnel models, the design space is limited using an upper and lower bound on each design variable, $b_{u,j}$ and $b_{l,j}$, where only airfoils with reasonable thickness in the trailing edge region are considered. To enable manufacturing, the wind tunnel models need to have a trailing edge thickness of 0.25%. To reduce pressure drag, the rotor and winglet airfoil thickness is set to 14% and 12%, respectively. To increase the numerical stability in XFOIL, the airfoils are optimised for a Reynolds number corresponding to a TSR of 5.5, which is slightly higher than the design TSR. The N_{crit} value in XFOIL is used to mimic the turbulence level on the airfoils [11]. For the rotor airfoil, an N_{crit} value of 6 is used, representing the turbulence level in the wind tunnel. To further stabilise the numerical calculations at the lower Reynolds number for the winglet airfoil, an N_{crit} value of 4 is applied. In Table 1, the design criteria for the airfoils are summarised.

The population size in CMA-ES is adjusted according to the number of CST design variables, and an optimal solution is chosen to be found when the largest change in $\boldsymbol{x}$ is smaller than $1 \cdot 10^{-3}$. The thickness of the rotor airfoil is equal to the S826 airfoil used on the 3-bladed NTNU model turbine, hence, the performance of the two airfoils can be compared.

Table 1: Airfoil design criteria.

Design criteria	Rotor airfoil	Winglet airfoil
Airfoil thickness	14%	12%
TE thickness	0.25%	0.25%
Reynolds number	$1.5 \cdot 10^5$	$0.8 \cdot 10^5$
N_{crit} value	6	4

2.3. Winglet shape optimisation

The winglet shape is optimised by constructing and refining a Kriging surrogate model using an infill criterion based on expected improvement. When using a surrogate, the number of computational expensive CFD simulations is reduced by creating an approximate model of the response when changing design variables. In Kriging, this approximate model is constructed using a Gaussian stochastic process modelling approach. This enables the calculation of an estimated error for the model's uncertainty, which is a key advantage since it allows the model to be refined by positioning infill points at locations with high uncertainty [12]. To construct the Kriging model, the MATLAB toolbox ooDACE, developed at Ghent University is applied [13]. The winglet shape is parametrised using 6 degrees of freedom and a normalised design space is created according to maximum and minimum values. To construct the initial Kriging model, a Latin Hypercube (LHC) sampling plan is created, and to avoid clustering and poorly sampled regions, the space-filling ability of the LHC is maximised using a genetic optimisation algorithm [14]. In Figure 2, the different design variables for the winglet are shown. In order to keep the total rotor radius constant at R=0.45 m, the location where the winglet is mounted to the rotor blade is adjusted

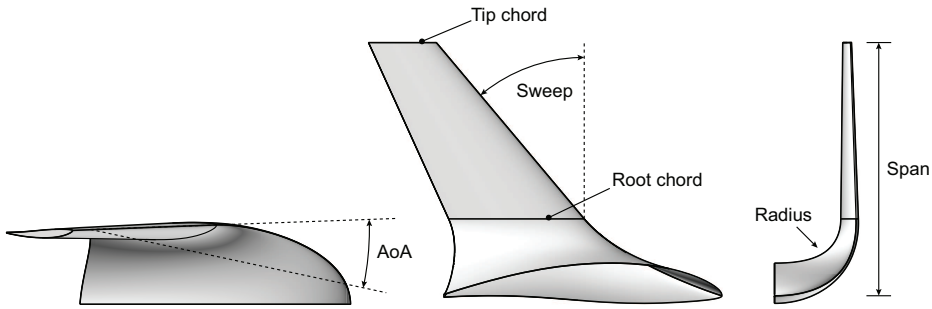

Figure 2: Winglet design variables.

according to the winglet radius. Hence, the rotor tip chord varies slightly around the value 0.04 m. Twist between the root and tip airfoil on the winglet is not considered. In Table 2, the maximum and minimum values used to normalise the design variables are given.

Table 2: Winglet design variables.

Design variables	Min	Max	w.r.t
x_1 - Span	5%	12.5%	Rotor span
x_2 - Sweep	0°	40°	-
x_3 - AoA	−2°	12°	-
x_4 - Radius	2.75%	3.5%	Rotor span
x_5 - Root chord	35%	100%	Rotor tip chord
x_6 - Tip chord	50%	100%	Winglet root chord

Since the Kriging model is only an approximation, the accuracy of the surrogate is enhanced by performing more simulations in addition to the initial LHC samples. The location of these infill points are computed using the expected improvement criterion given by

$$E[I(\boldsymbol{x})] = \begin{cases} (f_{min} - \hat{f}(\boldsymbol{x}))\Phi(\frac{f_{min}-\hat{f}(\boldsymbol{x})}{\hat{s}(\boldsymbol{x})}) + \hat{s}(\boldsymbol{x})\phi(\frac{f_{min}-\hat{f}(\boldsymbol{x})}{\hat{s}(\boldsymbol{x})}), & \text{if } \hat{s} > 0 \\ 0 & \text{if } \hat{s} = 0 \end{cases}. \tag{9}$$

where, Φ and ϕ are the cumulative distribution and probability density function, respectively [15]. Depending on the quality of the Kriging model, the largest improvement might exist either at under-sampled regions or in areas with improved solutions. The infill criterion thus explores and exploits the design space, and the global optimum solution is obtained when the Kriging model no longer has any expected improvement. In the expression, f_{min} and $\hat{f}$ are the current best and the predicted objective function values, respectively. The predicted mean square error is denoted $\hat{s}$. To find the infill point with the largest expected improvement, the $E[I(\boldsymbol{x})]$ criterion is maximised using a hybrid genetic-gradient algorithm. The genetic algorithm is given a population size of 200 and is allowed to evolve for 600 generations. At the end of the evolutionary search, a gradient algorithm is executed to ensure that the best local solution is found in the current global, best basin of attraction. The hybrid algorithm is stopped, and an optimal solution is chosen to be found when the largest change in $\boldsymbol{x}$ is smaller than $1 \cdot 10^{-6}$.

The performance of the rotor blade is maximised by considering the winglet as a single-point, unconstrained optimisation problem, and the

power coefficient of the wind turbine operating at its best TSR is used as objective function. The power coefficient is computed from

$$C_p = \frac{P}{\frac{1}{2}\rho U_\infty^3 A} \ , \tag{10}$$

where, P is the power produced by the turbine, ρ is the density of air and A is the swept area. Since the winglet increases the amount of lift on the rotor blades, the thrust force is important. On coefficient form the thrust is given by

$$C_t = \frac{T}{\frac{1}{2}\rho U_\infty^2 A} \ , \tag{11}$$

and in this work the increase in C_t due to the winglet is monitored. If the thrust is included as a constraint, the optimisation method would allow the rotor performance to be maximised within the specified limit. The ability to include constraints is an important advantage, since the performance of more traditional design methods e.g. parameter studies, or optimising the rotor circulation, will suffer when constraints are added.

To investigate the performance of the Kriging surrogate model and the infill criterion, a 2-dimensional Branin test function is first minimised. In order to obtain a response with two local minima and one global minimum the Branin function is modified according to [15].

The rotor performance with winglets is also compared to a turbine where the rotor radius is increased in order to produce the equivalent amount of power. The larger rotor span is created by extrapolating the chord and twist, using the rotor C_p with winglet as reference. The power production for the two designs are compared experimentally and the measured wind tunnel data is corrected using $\rho = 1.2$ kg/m^3.

2.4. CFD simulations and mesh

The performance of the wind turbine is simulated using the Navier-Stokes solver STAR-CCM+ from Siemens [16]. The turbine rotation is modelled using a moving reference frame model and the air is considered incompressible. To reduce the number of cells in the mesh, periodic boundary conditions are applied and only one rotor blade is present in the model. In Figure 3, the CFD domain and boundary conditions are shown. To ensure that the flow is free to expand, the inlet and far-field boundaries are positioned 8xR from the turbine, while the outlet boundary is located 6xR behind the turbine. To reduce the amount of unsteady flow, the hub is extruded the length of the flow domain.

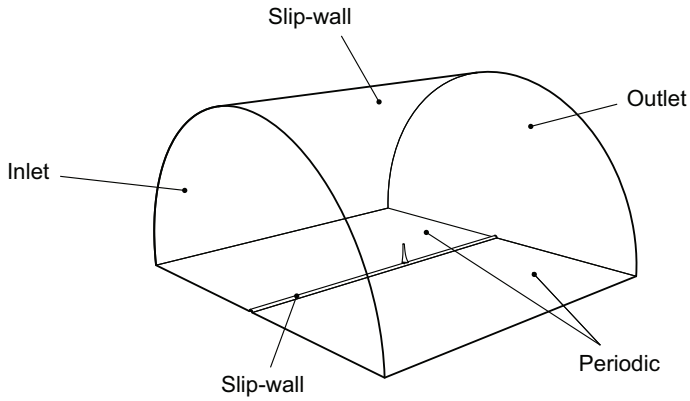

Figure 3: CFD domain and boundary conditions.

For the winglet shape optimisation, the turbulent flow is predicted using the Spalart Allmaras (SA) turbulence model. This is a one-equation, eddy viscosity turbulence model developed for the aerospace industry to predict attached boundary layers and flows with mild separation. The model solves a transport equation for the modified diffusivity $\tilde{\nu}$ to determine the turbulent viscosity, and a correction term is used to account for effects of strong streamline curvature and rapid frame-rotation.

To check the SA simulations and to analyse the transitional boundary layer flows, the rotor blade with the optimised winglet is simulated using an Elliptic Blending Reynolds-Stress Model (EB-RSM). This is a low-Reynolds number model, which solves the transport equations for each component of the Reynolds stress-tensor and, thus, accounts for the anisotropy of turbulence. The model predicts the turbulent flow more realistic than the SA turbulence model, but requires a more refined mesh and larger computational resources. When applying the EB-RSM, convergence is assumed to be reached when a drop in accuracy to the third decimal is obtained for the measured power and thrust coefficients. For the SA simulations, convergence is determined when a drop to the fourth decimal is reached.

To study the effects that the 13% blockage ratio in the NTNU wind tunnel has on the wind turbine performance, additional SA simulations are performed. Here, the distance to the far-field above the turbine is reduced to 2.78xR, a radius that corresponds to the cross-sectional area in the test section.

The turbine and flow domain is discretised using a trimmed hexahedral mesh in a Cartesian coordinate system. The mesh quality required to capture the flow on the rotor blade and wake is determined by reducing the

influencing mesh sizes until the change in turbine power and thrust is less than $1 \cdot 10^{-2}$. To reduce the computation time, only the mesh in the near-wake, 1.5 m behind the rotor is refined. In Figure 4, the mesh used for the SA simulations is depicted. In the mesh, both the extruded hub and the near-wake refinement region have a cell size of 12.5 mm.

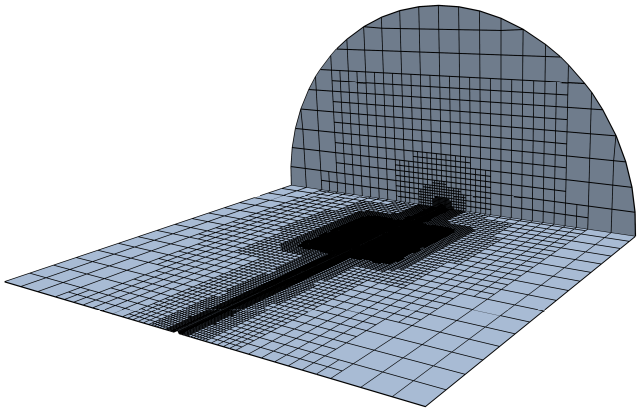

Figure 4: Flow domain mesh.

In Figure 5, a close view of the volume and surface mesh on the rotor is shown. The mesh used to capture the boundary layer flow is depicted in Figure 5a. Here, a 20 layer thick hyperbolic extruded prism layer is applied. The surface mesh depicted in Figure 5b, uses a cell size of 0.6 mm for the rotor blade. In the optimisation study, the winglet is meshed using a cell size of 0.5 mm. The final mesh without winglet has 5.5 million cells. With the winglet, the mesh size varies between 5.6 to 6.4 million cells depending

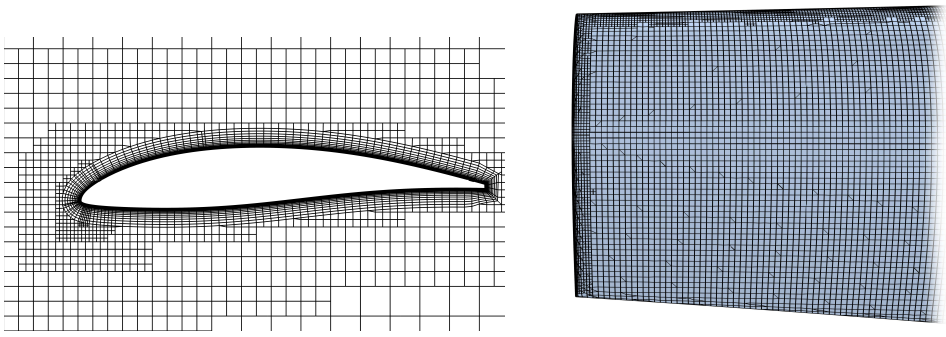

(a) (b)

Figure 5: Tetrahedral volume and surface mesh.

on the winglet shape.

A refined mesh is required for the EB-RSM simulations and 25 prism layers are used to capture the boundary layer. The surface cell size on the rotor blade and winglet is reduced to 0.5 mm and 0.25 mm, respectively. The wake and the extruded hub is discretised using a mesh size of 10 mm and the total mesh has about 20.4 million cells. To resolve the flow in the boundary layer, the first cell-centroid from the wall of the rotor blade and winglet are adjusted to obtain y^+ values smaller than 1, both for the SA and the EB-RSM simulations.

2.5. Wind tunnel experiments

Experiments are performed in the closed-return wind tunnel at the Department of Energy and Process Engineering at NTNU. The wind tunnel has a test section 2.71 m wide, 1.81 m high and 11 m long, where the turbine is positioned 4.3 m from the inlet. A wind speed of $U_\infty = 10$ m/s is chosen, and the turbulence intensity in the wind tunnel is about 0.23% [17]. The turbine torque and thrust are measured for TSR ranging from 2 to 10 using a torque transducer and a force balance. In Figure 6a, the wind turbine test model is shown in the wind tunnel. The rotor blades are 3D printed in an acrylic formulation named Verogray RGD850 [18]. Figure 6b shows the attachment used to mount the winglet and wing extension. In previous work, the performance of the 3-bladed NTNU turbine created in acryl and aluminium is compared [19]. The study discovered that the turbine power and thrust for the 3D printed and aluminium rotor blades compare well up to TSR 7.5. At higher TSR values, the thrust on the less stiff acrylic rotor is under predicted due to twist in the tip region. The 2-bladed wind turbine

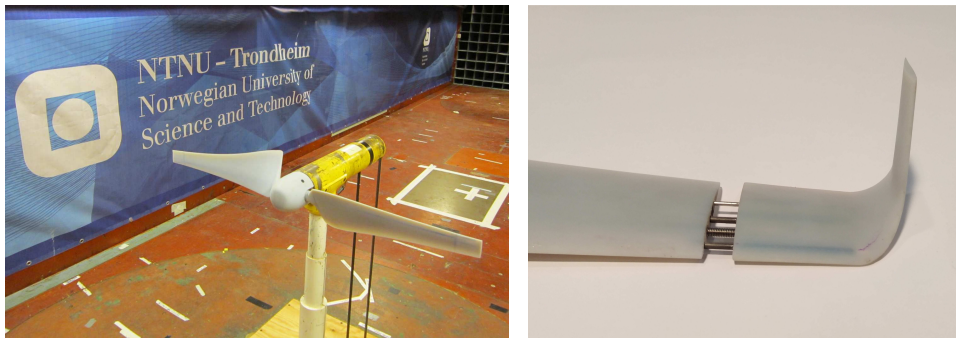

(a) (b)

Figure 6: Wind turbine in the wind tunnel and winglet attachment.

manufactured in this work is expected to have less twist, since the airfoil is designed with increased thickness in the trailing edge region and the rotor has larger chords.

3. Results

In the following, the results of the winglet optimisation are presented. First, the shape and performance of the optimised airfoils and the model-scale wind turbine are given. Then, the performance of the winglet optimisation method is investigated by minimising the Branin function in 2-dimensions. Finally, the winglet shape is optimised and the rotor blade performance is studied.

3.1. Airfoil performance

The design space for the airfoil optimisation is created using 6 CST design variables on both suction and pressure side of the airfoil geometry. The optimisation is performed for angles of attack ranging from 4° to 8° and a population size of 24 is used in the evolutionary CMA-ES algorithm. In Figure 7, the optimised rotor airfoil (R-opt) and the optimised winglet airfoil (W-opt) are shown. The R-opt airfoil is compared to the S826 airfoil, which is used on the 3-bladed NTNU wind turbine, see Figure 7a. As can be seen, the R-opt airfoil has increased thickness in the trailing edge region. The

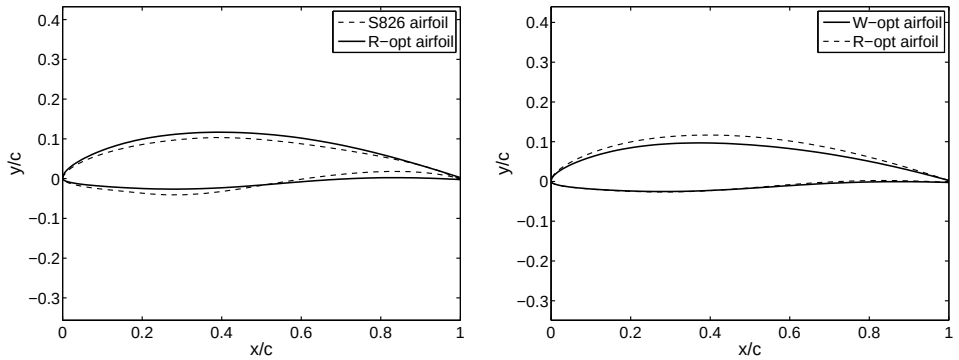

(a) (b)

Figure 7: Optimised airfoils for the rotor (R-opt) and winglet (W-opt).

S826 airfoil is, however, originally designed as a tip airfoil for wind turbines with rotor diameters between 20 and 40 meter, where the smaller thickness in the trailing edge region is compensated by larger chords [20]. In Figure 7b,

the shape of the W-opt and R-opt airfoil is compared. Interestingly, the smaller thickness and the lower Reynolds number on W-opt is compensated mainly by reducing the thickness on the suction side.

In Figure 8, the performance of R-opt, W-opt and the S826 airfoil is compared. In Figure 8a, the lift coefficient at different angles of attack, α, is shown. As is seen, the lift for the R-opt airfoil compares well to the S826, except in the region of the stall, where a less abrupt reduction in C_l is predicted for R-opt. At the lower Reynolds number, the reduced thickness on the suction side of W-opt is seen to reduce the lift compared to R-opt. In Figure 8b, the lift-to-drag coefficients for the airfoils are compared. Here, the performance of the optimised R-opt airfoil outperforms the S826 at all angles of attack. The better performance of R-opt at this Reynolds number is however expected, since the S826 airfoil is designed to operate at a Reynolds number about 10 times higher [20]. The best lift-to-drag ratio for the R-opt and S826 airfoil is 78 and 76, respectively. At the lower Reynolds number, W-opt has better performance than R-opt and the best lift-to-drag ratio is approximately 57 and 52, respectively.

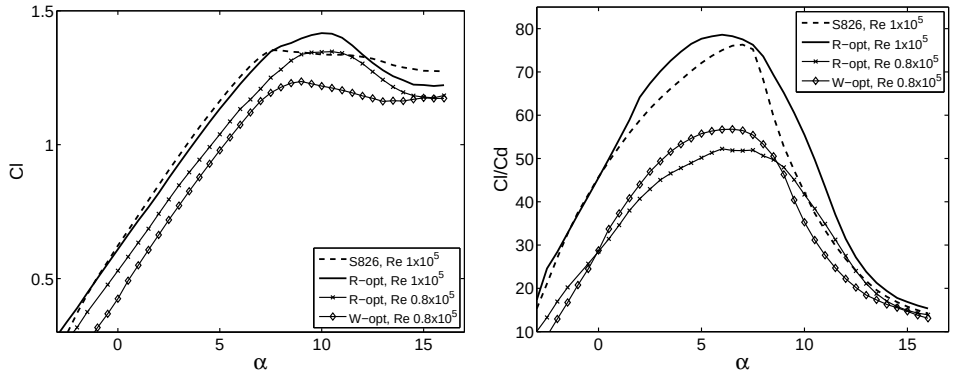

(a) (b)

Figure 8: Airfoil performance predicted using XFOIL.

3.2. Rotor blade performance

In Figure 9, the chord and twist distribution for the new 2-bladed rotor is compared to the 3-bladed NTNU model turbine. The two rotor blades are created using the same design method and the main differences are the airfoil shape and the number of blades. In Figure 9a, the chord distributions are compared. As is seen, the 2-bladed rotor has larger chords to match the solidity. In the root region, both rotors are modified according to the

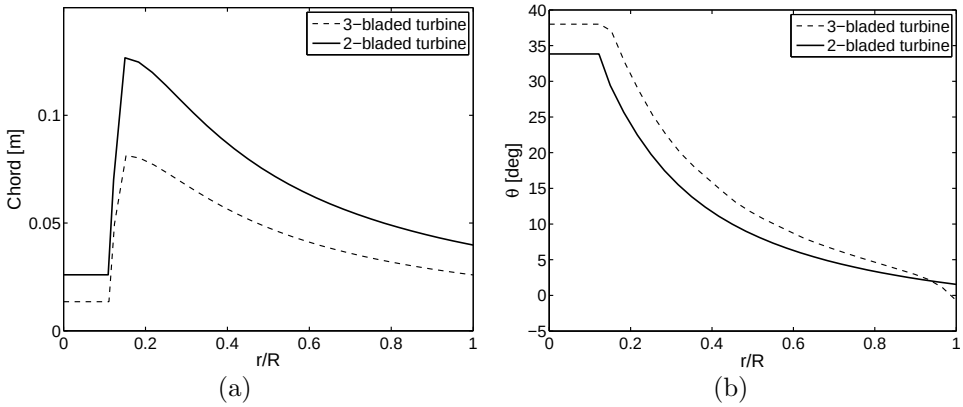

Figure 9: Chord and twist distribution.

experimental setup. In Figure 9b, the twist is shown. Here, the difference in twist is due to the different angle of best performance for the R-opt and the S826 airfoils.

In Figure 10, the measured performance for the two wind turbines is compared. The experiments are performed for a wind velocity $U_\infty = 10$ m/s and the power and thrust are presented on coefficient form. In Figure 10a, the power coefficient for the 2-bladed rotor can be seen to outperform the 3-bladed rotor for TSR values above 4.5. According to theory, a 2-bladed wind

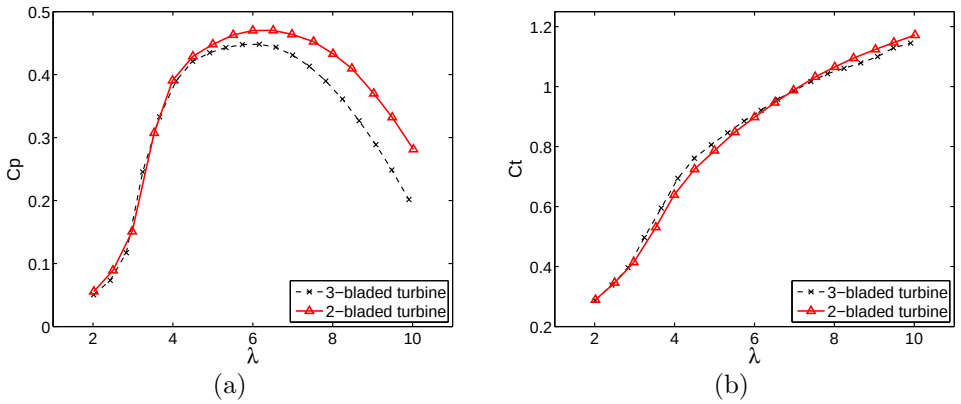

Figure 10: Measured power and thrust for 2- and 3-bladed turbine.

turbine only has slightly reduced performance compared to a 3-bladed wind turbine when airfoil drag is not included [21]. Hence, the better performance of the 2-bladed turbine is expected, since the optimised R-opt airfoil has

better performance than S826. In Figure 10b, the thrust coefficient for the two turbines is shown. Here, the better performance for the 2-bladed turbine does not increase the thrust. For TSR values smaller than $\lambda = 7$, the C_t values on the 2-bladed turbine are about equal or slightly reduced compared to the 3-bladed turbine. At larger TSR, a small increase in thrust coefficient is observed.

3.3. CFD validation

In Figure 11, the SA simulated wind turbine performance without winglet is validated to wind tunnel experiments. In Figure 11a the simulated power coefficients at free-flow conditions can be seen to strongly underpredict the performance compared to the measured wind tunnel data. It is evident that the 13% blockage has a large effect on the power generated by the wind turbine. In the simulations where the distance to the far-field above the turbine is reduced according to the size of the wind tunnel, the predicted and the measured C_p values compare well. The increase in power for the wind turbine occurs since the energy in the wind is not free to expand, but is constricted by walls. At TSR below $\lambda = 3.5$, the simulated free-flow C_p can be seen to match the measured data very well. This is because the rotor blades are operating mostly in stall, and the free-stream wind is able to pass unaffected through the unloaded rotor system. In [22] it is found that to be free from blockge effects, the ratio between the rotor and the size of the wind tunnel should be smaller than 5%. It is also observed that while the rotor blade is designed using BEM for $\lambda = 5$, the free-flow SA simulations predict the best performance at $\lambda = 5.5$. With wind tunnel

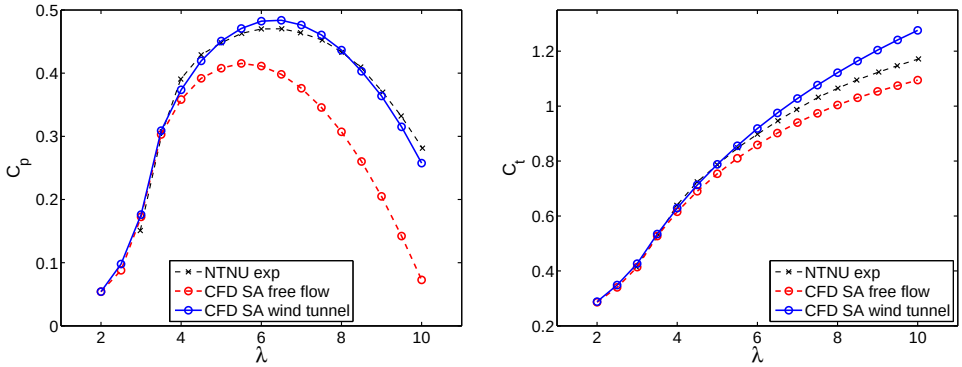

Figure 11: CFD simulations and measured wind tunnel data.

walls, the TSR for best performance is shifted to approximately 6 in both the experimental and simulated results. It is found in [22] that even though a large blockage ratio increases the wind turbine power, the change in flow on the rotor blades is insignificant.

In Figure 11b, the simulated and the measured thrust coefficients for the wind turbine are compared. Here, the free-flow simulations can be seen to predict lower thrust compared to the experimental data at TSR values larger than 3.5. However, when the size of the wind tunnel, and thus the blockage, is accounted for, the simulated thrust is overpredicted. This indicates that even lower C_t values should have been produced by the Spalart Allmaras turbulence model in the free-flow simulations. For TSR values below 3.5, the blockage effects are not present, and the simulated C_t values compare very well to the measured wind tunnel data.

3.4. Winglet optimisation study

To investigate the performance of the Kriging surrogate model and the expected improvement infill criterion, the 2-dimensional Branin function is minimised. In Figure 12, the Branin function and the Kriging surrogate are compared. Here, an LHC sampling plan consisting of 20 data points (triangles) is used to construct the initial Kriging model. To maximise the space-filling ability, the LHC is optimised using a genetic algorithm with a population size of 20, evolved for 200 generations. To find the best solution in the design space, the expected improvement criterion (circles) is

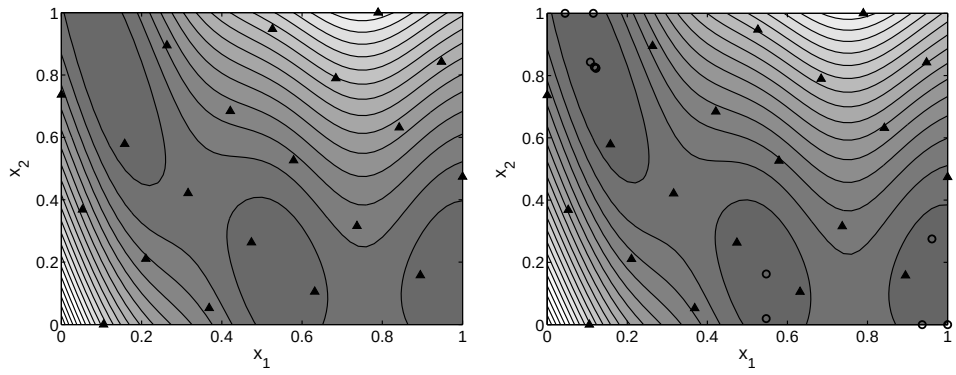

Figure 12: Branin function (left), Kriging model (right).

maximised using a hybrid genetic-gradient algorithm. In the depicted example, no expected improvements exist and the global optimum is obtained (x_1=0.1216, x_2= 0.8239) after 11 infill points. As is seen, the final Kriging

model represents the true Branin function very well. In the optimisation, both regions with high uncertainty (design space boundaries) and regions with improved solutions (the local and global minima) are investigated by the infill criterion. It is observed that by reducing the size of the LHC, the total number of samples required to find the global optimum is also reduced. If the LHC is increased on the other hand, the Kriging model gets saturated, and the global best solution is often found on the first iteration. Since a large LHC increases the required total number of data points, it is tempting to start the optimisation using a small LHC. However, to avoid a perceptive initial Kriging model it is recommended in [12] that approximately one-third of the total number of points should be in the sampling plan, and two-thirds determined by the infill points.

The design space for the winglet optimisation is parametrised using 6 design variables. In Figure 13, three possible winglet shapes in the design space are shown. Here, winglet **a** is given the minimum allowable values for span and sweep, while the chords are maximised. Winglet **b** uses medium values for all design parameters, and winglet **c** is created using maximum span and sweep, and minimum chords. The total number of winglet shapes

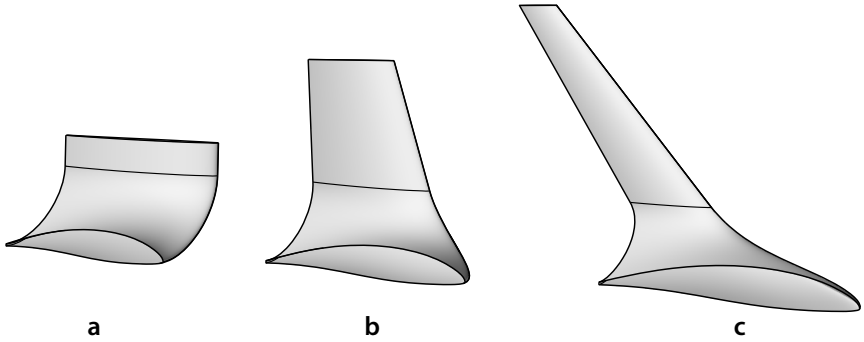

Figure 13: Examples of winglets in the design space.

investigated in the optimisation is determined according to the computational time required to reach a converged solution. The simulations are performed for $\lambda = 5.5$ on a Dell power blade cluster running 36 CPUs in parallel, and a converged solution is reached in about 3-4 hours. The simulation time limits the number of winglets, hence, 100 shapes are investigated. Here, 30 winglets are simulated in the LHC, while 70 shapes are determined by maximising $E[I(\boldsymbol{x})]$.

In Figure 14, the percentage increase in power and thrust coefficient due to the winglet shapes obtained in the optimisation study are presented. As

can be seen, the initial LHC simulation samples the design space well and winglets that both reduce and improve the rotor performance are tested.

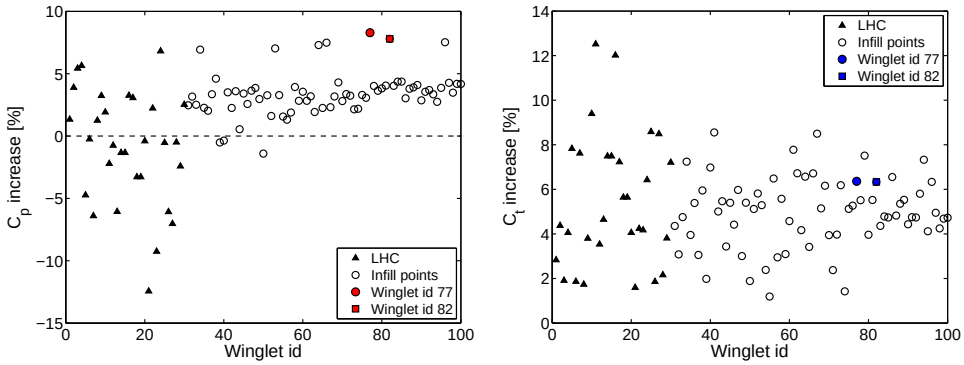

(a) (b)

Figure 14: Winglet optimisation study.

The infill points continue to explore the design space and as the Kriging model is refined, most winglet shapes improve the turbine performance. At the end of the optimisation, expected improvement still exists in the 6-dimensional, multi-modal solution space, i.e. the global optimum might not have been obtained. Hence, more winglet shapes should be tested. Nevertheless, 8 shapes are found in the Kriging model, which increase the turbine performance by more than 6%. The best solutions are winglet id 77 and 82, which increase the turbine C_p by 8.28% and 7.80%, respectively. In Figure 14b, the corresponding increase in C_t is shown. Here, the largest differences in thrust are seen in the LHC, while the increase is less for the winglets investigated using the infill criterion. For winglet id 77 and 82 the increase in thrust is 6.36% and 6.33%, respectively. In Table 3, the five best performing winglet (WL) shapes are listed. It can be seen that winglet id 77 has the largest increase in power. However, this winglet also has the

Table 3: Best performing winglet shapes with increase in C_p and C_t.

WL id	x_1	x_2	x_3	x_4	x_5	x_6	C_p	C_t
64	0.6456	0.4299	0.1142	0.5025	0.4144	0.7446	7.30%	6.57%
66	0.6689	0.1289	0.0671	0.4991	0.4499	0.7552	7.49%	6.71%
77	0.8960	0.4508	0.0258	0.3973	0.3445	0.7772	8.28%	6.36%
82	0.7683	0.4465	0.0592	0.4381	0.3585	0.7629	7.80%	6.33%
96	0.6739	0.2510	0.0300	0.7918	0.4239	0.8426	7.52%	6.33%

largest physical span, $x_1 = 0.896$. In order to validate the acrylic 3D printed winglet in the wind tunnel, winglet id 82 is chosen to be the best solution. This winglet has slightly reduced C_p and a smaller span, $x_1 = 0.7683$. In Figure 15 the winglet is depicted and its un-normalised design values are listed in Table 4.

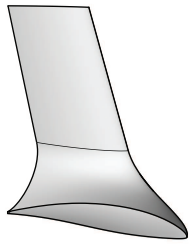

Figure 15: Winglet id 82.

Parameters	Value	w.r.t
Span	10.76%	Rotor span
Sweep	17.86°	-
AoA	-1.17°	-
Radius	3.09%	Rotor span
Root chord	58%	Rotor tip chord
Tip chord	88%	Winglet root chord

Table 4: Winglet design parameters.

3.5. Winglet analysis

The performance of the rotor blade with the optimised winglet is investigated numerically and experimentally for TSR values ranging from 2 to 10. In Figure 16, the simulated vorticity at $\lambda = 6$, with the SA and the EB-RSM turbulence models is depicted. As can be seen, the EB-RSM simulations provide a more detailed description of the wake.

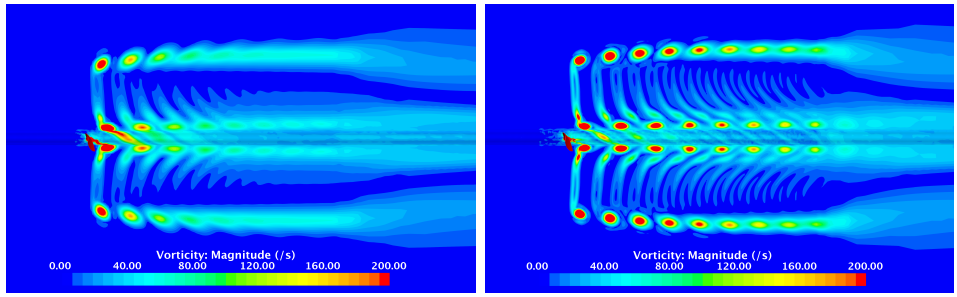

Figure 16: SA wake (left), EB-RSM wake (right).

In Figure 17, the simulated wind turbine performance with and without winglets is compared. The increase in power coefficient due to the winglet is shown in Figure 17a. Here, the SA simulations predict a symmetrical increase in turbine C_p around the design point at $\lambda = 5.5$ with the winglet. At TSR lower than 3.5 and for TSR larger than 8.5, the simulated turbine

performance is unaffected by the winglet. Since the EB-RSM simulations increase the computational time by a factor of 10-15 compared to the SA simulations, only TSR values with steady flow are investigated. As shown in the same figure, EB-RSM predicts a slightly better performance, both with and without winglet, compared to the SA simulations. With the EB-RSM, the best winglet performance is predicted at $\lambda = 6$, where the winglet increases the turbine C_p by 5.8%. In Figure 17b, the SA simulated thrust coefficients with winglet do not increase at TSR values below $\lambda = 3.5$ compared to the turbine without winglets. At values above, the difference in thrust coefficients steadily increases. In the EB-RSM simulations the C_t values are slightly reduced, compared to the SA turbulence model for $\lambda = 5$. At $\lambda = 6$, the EB-RSM predicts an increase in turbine C_t of 5.9% due to the winglet.

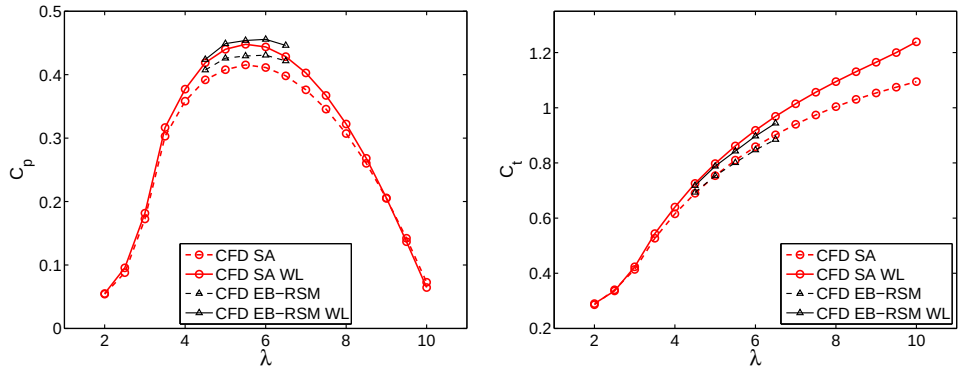

(a) (b)

Figure 17: Simulated winglet performance.

In Figure 18, the experimental results for the wind turbine with and without winglet are shown. Here, it is found that the wind tunnel blockage effect changes the flow on the winglet slightly. Based on additional CFD simulations and experimental parameter studies, a modified winglet is created to compensate for the different flow. This winglet has an increased angle of attack, $\alpha = 1.2°$. In Figure 18a, the turbine power with and without winglet is shown. As can be seen, compared to the simulated predictions the performance with winglet is worse. The best increase in power is 8.9%, however, it occurs at $\lambda = 7$. The improvement is not symmetrical and at lower TSR values, only a small increase in performance exists. In Figure 18b, the thrust force can be seen to resemble the CFD simulations better, and at $\lambda = 7$ the winglet increases the thrust by 7.4%.

The low increase in performance found in the experimental results can

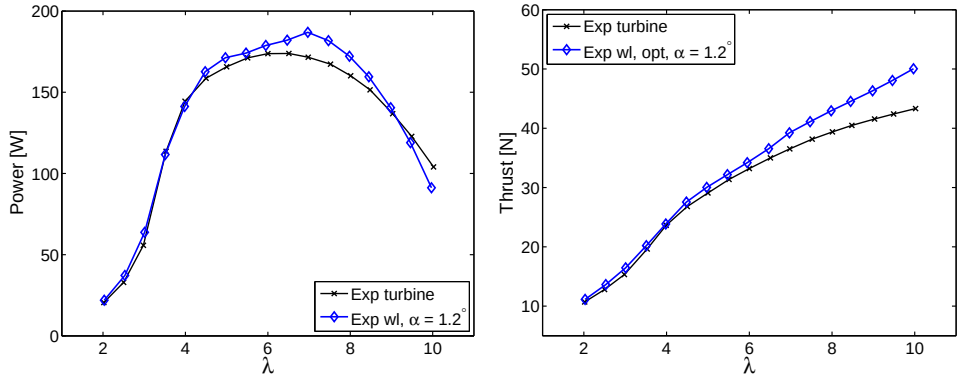

(a) (b)

Figure 18: Measured winglet performance.

be explained by laminar separation of the boundary layer on the model-scale winglet. In order to reduce laminar separation, the turbulence intensity in the wind tunnel flow is increased using a grid. With the grid, the turbulence intensity in the test section is about 5% [17].

In Figure 19, the measured turbine power and thrust with the grid is compared to the winglet and to the extended tip, where the rotor radius is increased by 3.64%. In Figure 19a, the increased turbulence level can be seen to improve the winglet performance. The best increase in power with

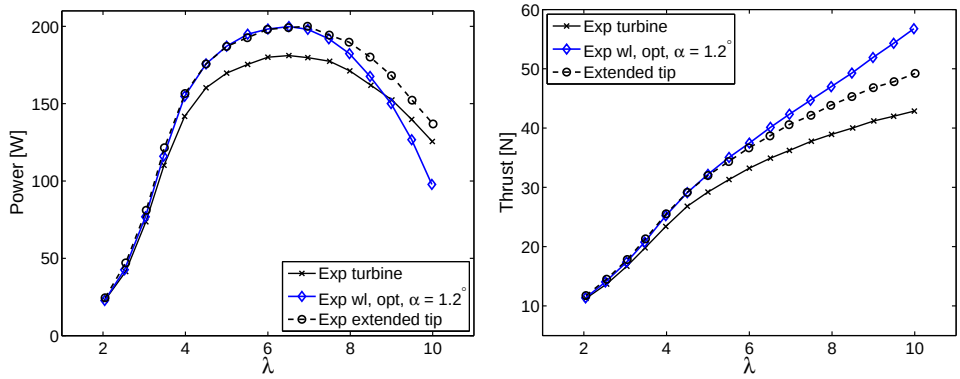

(a) (b)

Figure 19: Measured winglet and extended tip performance, with grid.

the winglet is 10.3% at $\lambda = 6.5$. At TSR values larger than about 9 however, the rotor with winglet produces less power than the turbine without winglet. With the extended tip, the rotor power compares very well to the winglet for TSR values below 6.5. At higher TSR values, the extended tip has better

performance. However, the larger rotor radius also increases the blockage ratio in the wind tunnel and this could explain the better performance.

In Figure 19b, the thrust is compared. Here, the thrust for the turbine with winglets and extended tip is seen to compare well for TSR values below 5. At higher values, the thrust forces on the rotor with winglet grow faster than the rotor blade with extended tip. This is unexpected, since the increased thrust is not measured in the experiments without the grid. The increase in rotor thrust is investigated further using a high-speed camera. It is found that for TSR values above 6 the acrylic winglet increasingly twists and bends, hence the performance is reduced.

To understand how the winglet increases the power production for the wind turbine, the EB-RSM simulations are investigated in detail at $\lambda = 6$. In Figure 20, the flow on the suction side of the rotor blades with and without winglet are compared. Here, the flow is visualised using constrained streamlines of the relative velocity and turbulent kinetic energy (TKE). The figures are created using a perspective projection mode in order to show the flow on the winglet. As seen, the flow on the rotor blades is similar, except locally at the tip, where the streamlines for the blade with winglet are more parallel to the chord-wise direction. On the rotor blade without winglet, the flow at the tip is skewed due to the pressure difference between the suction and pressure side on the blade, and when the two flows meet at the tip a

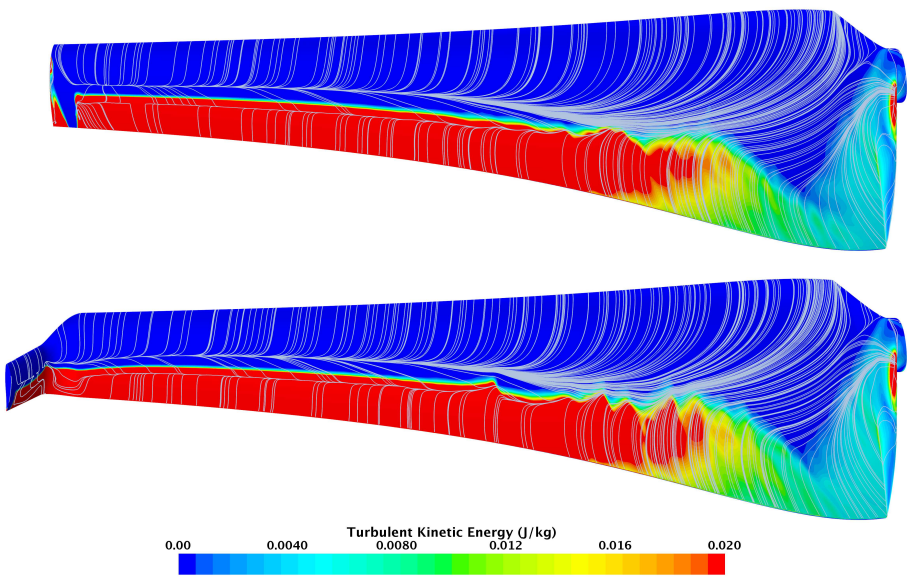

Figure 20: Rotor blade flow comparison, suction side.

vortex is created. This phenomenon is known as induced drag, or drag due to lift, and increases the drag and reduces the lift on the rotor blade. For the wind turbine studied in this work, the main contribution to the reduced performance is found to be the loss in lift.

In the root region of the blades, in the same Figure 20, the flow is strongly affected by the rotation and the streamlines follow the rotors in the span-wise direction. Further out on the blades, the rotational velocity is higher and the flow is more parallel to the chord-wise direction. Here, a laminar separation bubble is created at about half chord. The start of the bubble is seen where the streamlines form a stagnation line in the laminar region of the TKE. Transition to turbulence then occurs where turbulent kinetic energy is created, and the flow re-attaches as turbulent flow at a stagnation line, which can be seen behind the transition point.

In Figure 21, the constrained streamlines and the turbulent kinetic energy on the pressure side of a rotor blade with and without winglets is compared. Here, only laminar flow is predicted by the EB-RSM. In the root region, the flow on the blades is less affected by the rotation than on the suction side, and the main difference in flow occurs at the tip. As is seen, the flow on the rotor without winglet is more skewed due to the induced drag.

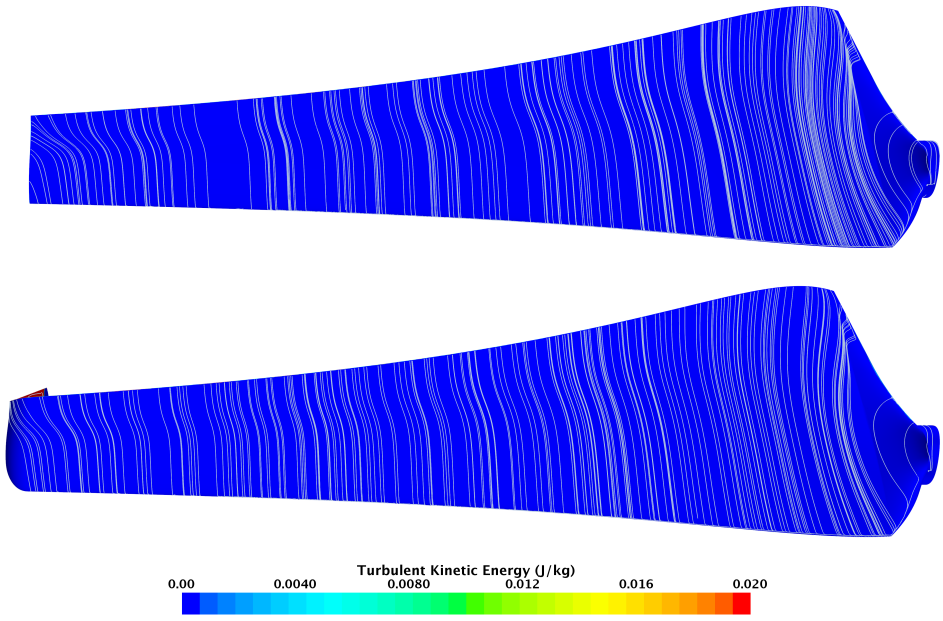

Figure 21: Rotor blade flow comparison, pressure side.

In Figure 22, the pressure on the suction side of the rotor blade with winglet, without winglet, and with the extended tip is shown. In the figure, the pressure is scaled to better visualise the lift in the tip region. As can be seen, the rotor blade with winglet has a larger and stronger region of negative pressure, compared to the rotor without winglet. The improved lift is generated since the flow-field on the winglet interacts with the flow-field on the rotor blade and reduces the amount of span-wise flow in the tip region of the blade. The winglet thus shifts the pressure difference from the rotor blade to the winglet, and the induced drag on the rotor is

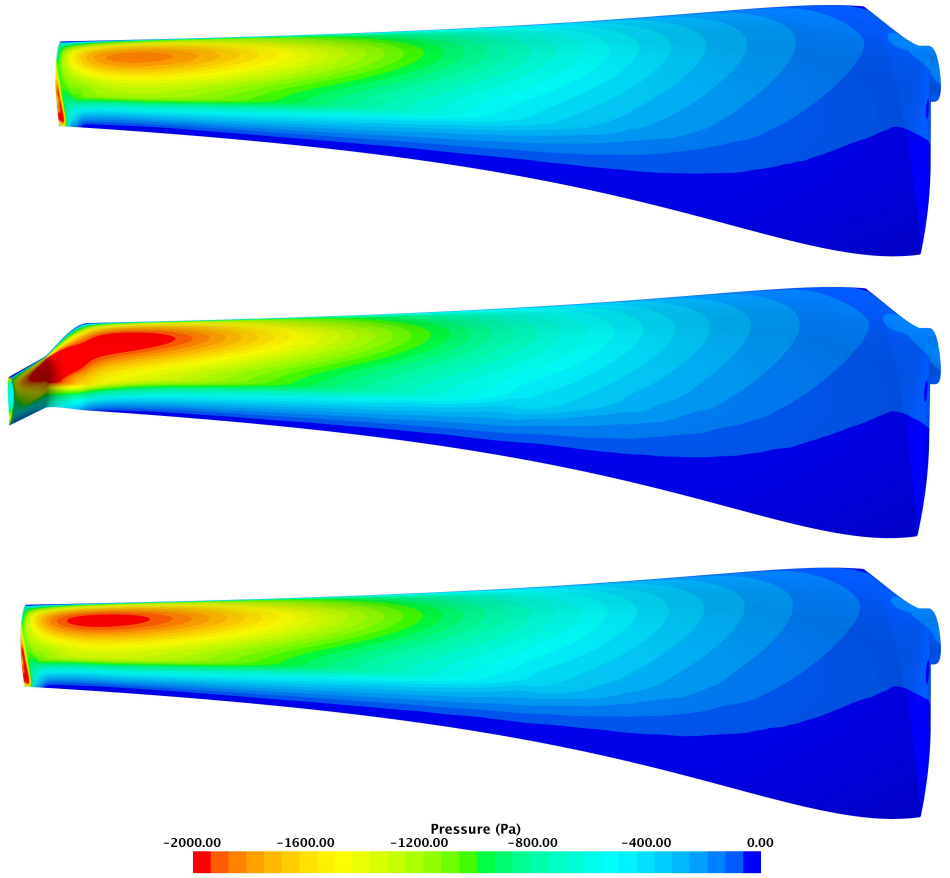

Figure 22: Rotor blade pressure comparison.

reduced. The presence of the winglet introduces additional drag, however, the larger lift on the rotor blade compensates the extra drag, and the power coefficient for the wind turbine is increased. As is seen, induced drag now

exists on the winglet, and the lift generated in the tip region of the winglet is therefore reduced. Hence, if the design space is expanded to include refinement of the winglet tip shape, it is believed that a more efficient winglet could be optimised. Also for the rotor with extended tip, a larger and stronger region of negative pressure is obtained. Here, the better lift is created by shifting the local induced drag phenomena further out on the rotor blade, and thereby expanding the region where lift is created. Since the new tip is an extension, also the aspect ratio is increased slightly. The better performance is, thus, the combined result of capturing more wind energy using a larger rotor radius and reducing the induced drag by using smaller tip chords. As can be seen, a pressure difference at the tip of the blade still exists. Hence, by applying a winglet also on the blade with extended tip, the induced drag would be reduced and the rotor performance could be increased further.

4. Conclusions

In this study, a winglet optimisation method is developed and tested for a model-scale wind turbine. The best performing winglet shape is obtained by constructing and refining a Kriging surrogate model using an infill criterion based on expected improvement. The turbine performance is simulated by solving the incompressible RANS equations and the turbulent flow is predicted using the Spalart Allmaras turbulence model. The winglet is parametrised using 6 design variables, and 100 shapes are tested in the optimisation. To validate the simulated results, experiments are performed in the NTNU wind tunnel, using 3D printed test models.

It is found that the method performs well, and the optimised winglet increases the power coefficient for the turbine by 7.8%, while increasing the trust by 6.3%. In the optimisation, however, the infill criterion is not fully converged, and a better winglet shape might exist in the design space. The wind tunnel experiments show that the winglet increases the power and thrust by 8.9% and 7.4%. However, due to the small scale, the winglet performance is influenced by laminar separation and the increase in performance only occurs in a small range of operational conditions. To eliminate laminar separation, additional wind tunnel tests are performed using a grid to increase the turbulence intensity. With the grid, the winglet increases the turbine power in a wider range of conditions, and the largest increase in power and thrust is 10.3% and 14.9% at a tip speed ratio of 6.5. It is found that the winglet improves the turbine power mainly by increasing the lift locally in the tip region of the rotor blades. Here, the induced drag is

reduced since the pressure difference on the rotor blades is shifted to the winglet. However, since induced drag exists on the winglet, a slightly better solution could be obtained by including an extra design variable for the winglet tip shape. Future studies should include constraints in the Kriging optimisation and simulate the wind turbine using a turbulence model that captures the flow physics even better.

5. Acknowledgments

This project is financially supported by the Research Council of Norway and CMR Prototech. The authors wish to thank Professor Per-Åge Krogstad and Professor Lars Sætran at the Department of Energy and Process Engineering at the Norwegian University of Science and Technology (NTNU) as well as Professor Muyiwa S. Adaramola from the faculty of Environmental Sciences and Natural Resource Management at the Norwegian University of Life Sciences (NMBU) for supervising this work. Also, thanks to Dr. Sonia Faaland at CMR Prototech for her support throughout this study.

References

[1] W. Freitag and E. T. Schulze. Blended winglets improve performance. *AERO-MAGAZINE*, 35(03), 2009.

[2] M. D. Maughmer. The design of winglets for high-performance sailplanes. *Technical Soaring*, XXVII:44–51, 2003.

[3] D. C. Maniaci and M. D. Maughmer. Winglet design for wind turbines using a free-wake vortex analysis method. In *50th AIAA Aerospace Sciences Meeting including the New Horizons Forum and Aerospace Exposition*, Nashville, Tennessee, 2012. AIAA 2012-1158.

[4] M. Gaunaa and J. Johansen. Determination of the maximum aerodynamic efficiency of wind turbine rotors with winglets. *Journal of Physics*, (Conference series 75 (2007)), 2007. doi:10.1088/1742-6596/75/1/012006.

[5] M. O. L. Hansen. *Aerodynamics of Wind Turbines*. Earthscan, London, UK, 2nd edition, 2008.

[6] P.-Å. Krogstad and P. E. Eriksen. "Blind test" calculations of the performance and wake development for a model wind turbine. *Renewable Energy*, 50:325–333, 2013.

[7] T. H. Hansen. Airfoil optimisation for wind turbine application. Submitted to *Wind Energy* January 2017.

[8] B. M. Kulfan and J. E. Bussoletti. Fundamental parametric geometry representation for aircraft component shapes. In *11th AIAA/ISSMO Multidisciplinary Analysis and Optimization Conference*, Portsmouth, VA USA, September 6–8 2006. AIAA 2006-6948.

[9] M. Drela. *XFOIL: An Analysis and Design System for Low Reynolds Number Airfoils. Low Reynolds Number Aerodynamics*. Springer-Verlag, 1989. Lecture notes in Eng. 54.

[10] N. Hansen. *The CMA Evolution Strategy: A Tutorial*. Research Centre Saclay-Île-de-France, Université Paris-Saclay, April 2016.

[11] M. Drela and H. Youngren. XFOIL 6.9 User Primer, April 2014. http://web.mit.edu/drela/Public/web/xfoil/.

[12] A. Forrester, A. Sóbester, and A. Keane. *Engineering design via surrogate modelling*. John Wiley & Sons, 1st edition, 2008.

[13] I. Couckuyt, T. Dhaene, and P. Demeester. ooDACE Toolbox: A flexible object-oriented Kriging implementation. *Journal of Machine Learning Research*, 15:3183–3186, 2014.

[14] MathWorks Inc. *Global Optimization Toolbox User's Guide, R2015b*, 2015.

[15] J. M. Parr, C. M. E. Holden, A. I. J. Forrester, and A. J. Keane. Review of efficient surrogate infill sampling criteria with constraint handling. In *2nd International Conference on Engineering Optimization*, Lisbon, Portugal, September 2010.

[16] CD-Adapco. *Introducing STAR-CCM+*, 2017. User guide, STAR-CCM+ version 12.02.010.

[17] P.-Å. Krogstad, L. Sætran, and M. S. Adaramola. "Blind test 3" calculations of the performance and wake development behind two in-line and offset model wind turbines. *Journal of Fluids and Structures*, 52:65–80, 2015.

[18] Stratasys. *Verogray RGD850*. Safety data sheet, revision A, 2nd March 2016.

[19] F. Mühle, M. S. Adaramola, and L. Sætran. Alternative production methods for model wind turbine rotors – is the 3D printing technology suited? In *12th EAWE PhD Seminar on Wind Energy in Europe*, DTU Lyngby, Denmark, May 25–27 2016.

[20] Dan M. Somers. The S825 and S826 airfoils period of performance: 1994 - 1995. Report SR-500-36344, National Renewable Energy Lab, Golden, Colorado USA, January.

[21] J. F. Manwell, J. G. McGowan, and A. L. Rogers. *Wind Energy Explained*. John Wiley & Sons, 2002.

[22] H. Sarlak, T. Nishino, L. A. Martinez-Tossas, C. Meneveau, and J. N. Sørensen. Assessment of blockage effects on the wake characteristics and power of wind turbines. *Renewable Energy*, 93:340–352, 2016.